SANDIA REPORT
SAND2013-8251
Unlimited Release
September, 2013

Fundamental Study of CO_2-H_2O-Mineral Interactions for Carbon Sequestration, with Emphasis on the Nature of the Supercritical Fluid-Mineral Interface

Charles R. Bryan, Thomas A. Dewers, Jason E. Heath, Yifeng Wang, Edward N. Matteo, Stephen P. Meserole, and David R. Tallant

Prepared by
Sandia National Laboratories
Albuquerque, New Mexico 87185 and Livermore, California 94550

Sandia National Laboratories is a multi-program laboratory managed and operated by Sandia Corporation, a wholly owned subsidiary of Lockheed Martin Corporation, for the U.S. Department of Energy's National Nuclear Security Administration under contract DE-AC04-94AL85000.

Approved for public release; further dissemination unlimited.

Sandia National Laboratories

Issued by Sandia National Laboratories, operated for the United States Department of Energy by Sandia Corporation.

NOTICE: This report was prepared as an account of work sponsored by an agency of the United States Government. Neither the United States Government, nor any agency thereof, nor any of their employees, nor any of their contractors, subcontractors, or their employees, make any warranty, express or implied, or assume any legal liability or responsibility for the accuracy, completeness, or usefulness of any information, apparatus, product, or process disclosed, or represent that its use would not infringe privately owned rights. Reference herein to any specific commercial product, process, or service by trade name, trademark, manufacturer, or otherwise, does not necessarily constitute or imply its endorsement, recommendation, or favoring by the United States Government, any agency thereof, or any of their contractors or subcontractors. The views and opinions expressed herein do not necessarily state or reflect those of the United States Government, any agency thereof, or any of their contractors.

Printed in the United States of America. This report has been reproduced directly from the best available copy.

Available to DOE and DOE contractors from
U.S. Department of Energy
Office of Scientific and Technical Information
P.O. Box 62
Oak Ridge, TN 37831

Telephone: (865) 576-8401
Facsimile: (865) 576-5728
E-Mail: reports@adonis.osti.gov
Online ordering: http://www.osti.gov/bridge

Available to the public from
U.S. Department of Commerce
National Technical Information Service
5285 Port Royal Rd.
Springfield, VA 22161

Telephone: (800) 553-6847
Facsimile: (703) 605-6900
E-Mail: orders@ntis.fedworld.gov
Online order: http://www.ntis.gov/help/ordermethods.asp?loc=7-4-0#online

SAND2013-8251
Unlimited Release
September, 2013

Fundamental Study of CO_2-H_2O-Mineral Interactions for Carbon Sequestration, with Emphasis on the Nature of the Supercritical Fluid-Mineral Interface

Charles R. Bryan
Department of Department of Storage and Transportation Technologies
Sandia National Laboratories
P.O. Box 5800
Albuquerque, New Mexico 87185-MS0779

Thomas A. Dewers
Department of Geomechanics
Sandia National Laboratories
P.O. Box 5800
Albuquerque, New Mexico 87185-MS0751

Jason E. Heath
Department of Geomechanics
Sandia National Laboratories
P.O. Box 5800
Albuquerque, New Mexico 87185-MS0751

Yifeng Wang
Department of Nuclear Waste Disposal Research & Analysis
Sandia National Laboratories
P.O. Box 5800
Albuquerque, New Mexico 87185-MS0779

Edward N. Matteo
Department of Nuclear Waste Disposal Research & Analysis
Sandia National Laboratories
P.O. Box 5800
Albuquerque, New Mexico 87185-MS0779

Stephen P. Meserole
Department of Materials Characterization and Performance
Sandia National Laboratories
P.O. Box 5800
Albuquerque, New Mexico 87185-MS1411

David R. Tallant
Department of Materials Characterization and Performance
Sandia National Laboratories
P.O. Box 5800
Albuquerque, New Mexico 87185-MS1411

Abstract

In the supercritical CO_2-water-mineral systems relevant to subsurface CO_2 sequestration, interfacial processes at the supercritical fluid-mineral interface will strongly affect core- and reservoir-scale hydrologic properties. Experimental and theoretical studies have shown that water films will form on mineral surfaces in supercritical CO_2, but will be thinner than those that form in vadose zone environments at any given matric potential. The theoretical model presented here allows assessment of water saturation as a function of matric potential, a critical step for evaluating relative permeabilities the CO_2 sequestration environment. The experimental water adsorption studies, using Quartz Crystal Microbalance and Fourier Transform Infrared Spectroscopy methods, confirm the major conclusions of the adsorption/condensation model. Additional data provided by the FTIR study is that CO_2 intercalation into clays, if it occurs, does not involve carbonate or bicarbonate formation, or significant restriction of CO_2 mobility.

We have shown that the water film that forms in supercritical CO_2 is reactive with common rock-forming minerals, including albite, orthoclase, labradorite, and muscovite. The experimental data indicate that reactivity is a function of water film thickness; at an activity of water of 0.9, the greatest extent of reaction in $scCO_2$ occurred in areas (step edges, surface pits) where capillary condensation thickened the water films. This suggests that dissolution/precipitation reactions may occur preferentially in small pores and pore throats, where it may have a disproportionately large effect on rock hydrologic properties.

Finally, a theoretical model is presented here that describes the formation and movement of CO_2 ganglia in porous media, allowing assessment of the effect of pore size and structural heterogeneity on capillary trapping efficiency. The model results also suggest possible engineering approaches for optimizing trapping capacity and for monitoring ganglion formation in the subsurface.

ACKNOWLEDGMENTS

This work was funded under LDRD Project Number151305 and Title "Fundamental Study of CO_2-H_2O-Mineral Interactions for Carbon Sequestration, with Emphasis on the Nature of the Supercritical Fluid-Mineral Interface". Many people contributed to the work presented here. John A. Merson of Sandia national Laboratories was the Project Manager. Cedric Sallaberry of Sandia National Laboratories provided assistance and mathematical expertise in the calculation of liquid water configuration in wedged-shaped pores for the CO_2-water-mineral system. Patrick D. Burton of Sandia National Laboratories and Rachel K. Wells of Texas A&M University provided experimental support for the QCM water adsorption experiments. Richard P. Grant of Sandia National Laboratories provided assistance in SEM/EDS imaging and data collection, and Ying-Bing Jiang of the University of New Mexico provided assistance in TEM and FIB analysis. Rex Hjelm, Victor R. Fanelli, and other personnel at the Los Alamos Neutron Beam Facility assisted with the neutron beam experiments, and were instrumental in interpretation of the neutron beam data. Finally, several personnel of the Sandia Geomechanics Department contributed in instrument design and testing, as well as supporting the experimental work performed at the LANSCE facility.

CONTENTS

1. Introduction 15

2. Theoretical Model for Water Adsorption and Capillary Condensation in Supercritical CO_2 19
   2.1 Introduction 19
   2.2 Theory of Aqueous Films in Supercritical CO_2 21
      2.2.1 Overview of Chemical Potential, Water Activity, Adsorption, and Capillarity. 21
      2.2.2 Adsorption of Water Films and Disjoining Pressure 24
   2.3 Results of the CO_2-Water Meniscus Model 30
   2.4 Conclusions 33

3. Measurement of Adsorbed Water Film Development in Supercritical CO_2 35
   3.1 Measuring water uptake with a quartz crystal microbalance 35
      3.1.1 Methods 35
      3.1.2 Results and Discussion 38
      3.1.3 Conclusions 44
   3.2 Measuring water uptake by Fourier Transform Infrared Spectroscopy 45
      3.2.1 Introduction 45
      3.2.2 Materials and Methods 46
      3.2.3 Results 47
      3.2.4 Implications for Geologic Carbon Storage 58

4. Determining Rock Hydraulic Properties in Supercritical CO_2: iN-Situ measurement of shrink-swell behavior of clay in dry-to-wet supercritical co_2 using neutron scattering 59
   4.1 Introduction 59
   4.2 Methods 59
   4.3 Results and Discussion 61

5. Assessing mineral surface reactivity in hydrous Supercritical CO_2 65
   5.1 Introduction 65
   5.2 Methods and Materials 67
      5.2.1 Mineral Samples and Preparation 67
      5.2.2 Experimental Setup and Conditions 67
      5.2.3 Post-test Sample Characterization 68
   5.3 Results and Discussion 69
      5.3.1 Ambient Pressure Experiments 69
      5.3.2 High Pressure Experiments in Humid Supercritical CO_2 72
      5.3.3 The Role of Capillary Condensation in Secondary Mineral Formation under Humid Conditions 73
      5.3.4 Surface Alteration by Dissolution and Secondary Mineral Formation 74
   5.4 Implications for Carbon Storage in Geologic Reservoirs 75

6. Ganglion Dynamics and its Implications For Geologic Carbon Dioxide Storage 77
   6.1 Introduction 77
   6.2 Dynamics of Supercritical CO_2 Ganglia 78
      6.2.1 General Model Formulation 78
      6.2.2 Trapping Criteria 80

6.3 Model Analysis: First Order Approximation 81
6.3.1 Capillary Trapping of $scCO_2$ Ganglia in the Absence of Water Flow 81
6.3.2 Effect of Reservoir Heterogeneity 83
6.3.3 Making $scCO_2$ Ganglia 84
6.3.4 Fate of Moving Ganglia 85
6.3.5 Mobilization of $scCO_2$ Ganglia by Water Flow 86
6.4 Model Analysis: First Order Approximation 88
7. Conclusions 93
8. References 95
Distribution 105

FIGURES

Figure 1. a) Thin section image of a quartz-rich sandstone (the Mount Simon Sandstone). Pore space is filled with pink epoxy. b) Schematic of a single triangular pore in an unsaturated CO_2 storage reservoir rock, showing liquid water (in blue) in corners and on flat pore surfaces as a function of three values of the chemical potential of water. 22

Figure 2. Schematic diagrams fluid-fluid interfaces in slit and corner geometries. a) Slit geometry defined by two parallel plates with Y as half the slit distance. b) Corner geometry with 2α as the angle between two planes. x* is the distance at which the curved fluid-fluid interface becomes equal to adsorptive film thickness. Modified from Tuller et al. [22]. 28

Figure 3. Liquid water menisci at the matric potential of -100 J/kg for air-water and CO_2-water cases in wedge-shaped pores with wedge angle of: a) 30°; b) 60°; and c) 90°. The annotated distances are in units of meters. "VZ" stands for vadose zone. 31

Figure 4. Air-water and CO_2-water menisci in 1×10^{-8} and 1×10^{-5} m equilateral triangular pores. The air-water meniscus forms an inscribed circle, which represents imbibition "snap off". For each pore, respectively, the CO_2-water menisci are calculated at the same chemical potential as the air-water interface. 32

Figure 5. Saturation of triangular pores as a function of the matric potential. Groups of three curves at different pore sizes (labeled with units of meters) are shown. Thus, one set of curves is the saturation path taken by a pore of a fixed size as the chemical potential of water increases for the air-water or CO_2-water system. The general range of pore throat sizes (in units of meters) from Nelson [53] is given at the top of the plot. 32

Figure 6. Imbibition snap-off as a function of a) chemical potential b) and activity of water for air-water and CO2-water systems, and for triangular or square pores 33

Figure 7. A) QCM wafer with a silica coating on the upper electrode. B) QCM wafer with a smectite clay film deposited on the crystal. 36

Figure 8. Experimental setup for measuring water adsorption in N_2 at ambient pressures. 37

Figure 9. Experimental setup for measuring water adsorption in $scCO_2$. 37

Figure 10. Water adsorption by the silica-coated Inficon QCM wafer. 38

Figure 11. Water adsorption curves for the Inficon silica-coated QCM wafer, compared to experimentally measured water adsorption data. 39

Figure 12. AFM image of the surface roughness of the silica layer on the Inficon wafers. 40

Figure 13. Water adsorption onto silica in $scCO_2$. Upper: Comparison with data from N_2. Lower: Comparison to published BET water vapor sorption isotherms. 41

Figure 14. Water adsorption by clay films occurs by several different mechanisms including interlayer cation hydration, surface adsorption, and capillary condensation. 42

Figure 15. Smectite clay adsorption isotherms for water in N_2, at ambient pressure. 43

Figure 16. Water adsorption isotherms for homionic (Na, K, Mg, and Ca) montmorillonite films. A) Adsorption isotherms in $scCO_2$; B) Comparison of isotherms in $scCO_2$ with those collected at ambient pressures. 44

Figure 17. PIKE Technologies "JetStream" ATR High Pressure FTIR Cell designed and built for this study. 47

Figure 18. Absorption spectra of CO_2 contacting the ZnSe crystal as pressure increases past the critical point (~1100 psi at 35ºC). 48

Figure 19. Spectra obtained with CO_2 at 1400 psi. 49

Figure 20. Spectra obtained at 1400 psi with 700 to 1100 µL added H_2O. 50

Figure 21. Spectra obtained at 1400 psi with added H_2O. 51

Figure 22. Spectra with ZnSe coated with silica. 52

Figure 23. Spectra from silica coated ZnSe element with progressively increasing amounts of H_2O added to the $scCO_2$ environment. 53

Figure 24. Spectra from silica coated ZnSe element with increasing RH in N_2. 54

Figure 25. Spectra from silica coated ZnSe element with increasing RH in N_2 (expanded frequency scale in the water stretch mode region). 54

Figure 26. FTIR spectra with clay coatings, using silica coated example as background. 55

Figure 27. FTIR spectra with clay coatings in $scCO_2$ with increasing H_2O. 57

Figure 28. FTIR spectra with clay coatings in $scCO_2$ with increasing H_2O (expanded-frequency-scale of water stretch mode region). 57

Figure 29. FTIR spectra with clay coatings in $scCO_2$ with increasing H_2O (expanded-frequency-scale of water bend-mode region). 58

Figure 30. Schematic and photo of Ti oedometer with dimensions. 60

Figure 31. Schematic diagram of second oedometer with annotation indicated by arrows. Note penny for scale. (Figure courtesy of Mark Taylor, Los Alamos National Laboratories) 61

Figure 32. Example of preliminary LQD results using the titanium oedometer. Black diamonds represent neat (i.e., not placed in vessel) pellets under no axial stress. Red and blue are, respectively, for dry and wet (D_2O-saturated) high pore pressure CO_2 conditions under axial load. 62

Figure 33. Preliminary results for the stainless steel-aluminum oedometer (note these data are preliminary). 63

Figure 34. High pressure experimental setup. Mineral samples were loaded into pressure cells and exposed to a $scCO_2/H_20$ mixture. P_w/P_{sat} was controlled by holding T2 at a higher temperature than T1, which corresponds to a vessel containing water saturated $scCO_2$. 69

Figure 35. Summary of albite alteration for various conditions. A= Expt #5, B= Expt #6, C= Expt#7, D = Expt #8, E and F = Expt in $scCO_2$, P_w/P_{sat} = 0.9. 71

Figure 36. SEM images of test minerals exposed to $scCO_2$. 1) Albite, 2) Orthoclase, 3) Labradorite, and 4) Muscovite 73

Figure 37. TEM/EDS element profile for orthoclase—atomic composition and ratio of elements 74

Figure 38. Conceptual model of pore structure and ganglion movement. (a) A thin section of Mount Simon Sandstone showing a typical sandstone pore structure, with red color indicating pore space (the horizontal field of view is 1.76 mm on the original specimen); (b) pore-scale ganglion movement at advancing and receding fronts. Symbols are defined in the text. 79

Figure 39. Critical vertical dimension for the entrapment of a $scCO_2$ ganglion as a function of pore diameter and contact angle (10º, 40º, and 70º) for a buoyance-only case. The size ratio of pore to throat is set to 5:1. 83

Figure 40. Effect of the pore size of an interbed on $scCO_2$ trapping. The ratio of pore diameter to throat diameter is 5:1 for both sandstone and interbed. 84

Figure 41. Finger spacing induced as $scCO_2$ displaces pore water during CO_2 injection, for two different reservoir permeabilities. The shaded area indicates the possible range of front velocities, assuming a typical CO_2 injection rate of 10^4 to 10^6 metric tons per year in a borehole of 0.3 m diameter and with 10 m injection interval. Finger spacing here is equivalent to the vertical dimension of a ganglion in Figure 39. 85

Figure 42. Ganglion breaking and trapping due to interface instability. The radii of pore throat and pore body are assumed to be 0.1 and 0.5 mm, respectively. To the left of the vertical broken line, ganglia are small and trapped. To the right, ganglia are large enough to attain sufficient rising velocities to cause further breaking up and trapping. The size of regenerated ganglia is calculated from Equations 6-15 and 6-16 by setting $\alpha = 0$, and thus $scCO_2$ fingering due to gravity instability is automatically accounted. Since the size of regenerated ganglia is smaller than the critical size (~ 0.1 m) for mobilization, all regenerated ganglia become trapped. 86

Figure 43. Mobilization and entrainment of ganglia by flow field. Larger ganglia would be more easily mobilized and move faster than the smaller ones in a given flow field. The radii of pore throat and pore body are assumed to be 0.1 and 0.5 mm, respectively. 87

Figure 44. Schematic illustration of the existence of an optimal condition for $scCO_2$ capillary trapping. 89

TABLES

Table 1. Values of Properties used in CO_2-Water-Mineral Model of Adsorptive Films and Capillary Water at Three Depths 26

Table 2. Summary of minerals used for the study, including source and chemcial composition as determined by electron probe microscopy. 67

Table 3. Summary of conditions and results for ambient pressure experiments 70

Table 4. Summary of conditions and results for high pressure experiments 72

Table 5. List of parameter values used in the model analyses 82

NOMENCLATURE

AFM	atomic force microscopy
ATR	attenuated total reflection
AYL	augmented Young-Laplace
CCUS	carbon capture, utilization, and storage
CT	computer tomography
DOE	Department of Energy
DLVO	Derjaguin-Landau-Verwey-Overbeek
EDS	energy dispersive (X-ray) spectroscopy
FIB	focused ion beam
FTIR	Fourier Transform Infrared Spectroscopy
LANSCE	Los Alamos Neutron Science Center
LQD	low-Q diffractometer
MHz	Megahertz
NAPL	nonaqueous phase liquid
PEEK	poly ether ether keytone
QCM	quartz crystal microbalance
RH	relative humidity
SANS	small angle neutron scattering
$scCO_2$	supercritical CO_2
SEM	scanning electron microscopy
SNL	Sandia National Laboratories
TEM	transmission electron microscopy
XRD	X-ray diffraction

1. INTRODUCTION

Carbon sequestration via underground storage in geologic formations is currently the only realistic approach for sequestering high-volume industrial CO_2 emissions. [1]. There is a direct need by operators/regulators for informed models that incorporate coupled multiphysics processes that influence subsurface CO_2 injection and that control the transport, and ultimately the fate, of the sequestered CO_2. Attempts to simulate injection, storage capacity, and reservoir retention (i.e., leakage) at Frio and Sleipner failed [2, 3], showing that current models are inadequate. The existing multiphysics models for CO_2 sequestration do not account for processes occurring at the $scCO_2$-mineral interface due to changing activity of water in the supercritical fluid, which may strongly affect core and reservoir-scale hydrologic properties. Interfacial processes control the wetting properties of minerals, and by affecting wettability (surface tension), affect the permeability of reservoir units and caprock seals with respect to water and $scCO_2$. The interface properties are strongly dependent upon the activity of water in the supercritical fluid, which will change as initially anhydrous $scCO_2$ absorbs water from formation brine. By analogy with vadose zone (air-water systems) as the water activity in the supercritical fluid increases, the water layer on hydrophilic mineral surfaces will thicken [4, 5], with concomitant changes in surface properties [6] that will affect how $scCO_2$ wets mineral surfaces, reservoir/caprock hydrological properties, and the mobility of $scCO_2$. Capillary condensation of water from $scCO_2$ and coalescence of water films will also occur; however, little is known about water film behavior, or even thickness, in $scCO_2$. Moreover, recent studies [7-11] have shown that the development of a water layer controls the chemical reactivity at the $scCO_2$-mineral interface, may be critical to mineral dissolution reactions in $scCO_2$.

Inherent technical challenges exist in performing nano-scale studies of the $scCO_2$-mineral interface, and in upscaling nano/core-scale results to reservoir-scale processes. Current multiphysics process models implement simplified equations of state (EOS) for CO_2, which do not consider the effects of changing water activity in the supercritical phase, and ignore osmotic and capillary condensation. Such processes potentially have large effects on the relative permeability of rock formations with respect to $scCO_2$, and on potential trapping mechanisms. Improved models, incorporating the effects of interfacial processes, are necessary to adequately assess the performance of underground CO_2 storage, and would represent a significant improvement in predictive capability. This work evaluates processes occurring at the $scCO_2$-mineral interface, and how those processes affect the macro-scale hydrologic properties of the reservoir host-rock and cap-rock. Theoretical, experimental, and modeling capabilities for understanding the interactions of supercritical CO_2-H_2O fluids with geologic formations have been developed.

Improved process-level understanding may also allow engineering of reservoir properties or injection methods to enhance sequestration. CO_2 storage designs are already considering injection of pulses of $scCO_2$ chased by brine/water to improve residual trapping processes. Here, we evaluate the dynamics of CO_2 ganglion movement and suggest injection techniques that may improve rates of secondary sequestration by capillary isolation.

The four major goals of this work, and the work done to address them, are provided below:

Determine the properties of water films on mineral surfaces with varying $scCO_2$ water content, at pressure and temperature conditions relevant to subsurface CO_2 sequestration. To address this, a model was developed for theoretically assessing the formation and evolution of water films on mineral surfaces in $scCO_2$ as a function of $scCO_2$ water content. The model assesses both water adsorption and capillary condensation in $scCO_2$, and provides estimates both of film thickness and of water saturation as a function of pore size. The evolution of pendular rings at contact points between particles/mineral grains at water into a fully connected water phase is important to the multiphase transport and trapping of the non-wetting (i.e., $scCO_2$) phase. Once water saturations increase to the point of isolating $scCO_2$ as individual ganglia in pores, the $scCO_2$ phase will be trapped. Capillary condensation of water from humid $scCO_2$ has not been previously evaluated, and no existing studies have measured hydraulic properties as a function of $scCO_2$ water activity. The properties of water films in $scCO_2$ were also evaluated experimentally. Formation and evolution of water films on silica surfaces with increasing $scCO_2$ water content was measured using both quartz crystal microbalance (QCM) techniques and Fourier Transform Infrared Spectroscopy (FTIR). Adsorption of water by smectite clay films silica was also measured by both techniques, to address uncertainty in the behavior of swelling clays in $scCO_2$. For both silica and clays, water uptake was also measured in nitrogen at ambient pressures, to improve the understanding of the importance of these processes relative to their better-known role in near-surface vadose zone environments.

Use core-scale tests to determine hydraulic rock properties as a function of $scCO_2$ water content. Efforts to address this goal focused on the swelling/desiccation behavior of smectite clays in the presence of $scCO_2$ and the resulting changes in clay/shale porosity and permeability. To evaluate clay swelling behavior at conditions relevant to CO_2 sequestration, a high pressure system was developed with a titanium pressure vessel capable of applying both hydrostatic and uniaxial loads on a clay sample. The Ti vessel was designed for use at the neutron beam facility at Los Alamos National Laboratories, to allow *in situ* measurement of pore size distributions and clay interlayer spacing via neutron scattering. A second vessel of aluminum was also developed.

Assess mineral surface reactivity in hydrous $scCO_2$. Mineral reactivity in hydrous $scCO_2$ was evaluated for four common silicate minerals (albite, orthoclase, labradorite, and muscovite), by exposure to $scCO_2$ with a water content equivalent to $P_w/P_{sat} = 0.9$. Mineral reactivity was also assessed at ambient pressures under both humid and immersed conditions, in both air and CO_2, as a baseline (while the $scCO_2$ work was unique, these may also be the first humid air dissolution experiments ever carried out for silicates). Extensive post-test characterization was used to assess mineral/hydrous $scCO_2$ reactivity and secondary phase formation. It is anticipated that mineral dissolution reactions will be accelerated as a free water layer forms on mineral surfaces, and capillary condensation processes may cause these reactions to preferentially occur in small pores and pore throats. Such preferential mineral precipitation would have a disproportionately large effect on hydrologic properties (i.e., permeability, capillary entry pressures).

Upscale $scCO_2$-mineral interfacial processes for use in reservoir-scale models. The model for water adsorption and capillary condensation in $scCO_2$ as a function of $scCO_2$ water content addresses this goal. The model provides a better understanding of adsorption and capillary rewetting phenomena in $scCO_2$ storage reservoirs, and of their impact on rock saturation and the corresponding relative permeabilities for water and $scCO_2$ in the reservoir rock. A second model

as also developed, which describes for the formation and movement of CO_2 ganglia in porous media, allowing assessment of the effect of pore size and structural heterogeneity on capillary trapping efficiency. It also suggested possible engineering approaches for optimizing trapping capacity.

In the following sections, the efforts to address each of these goals will be described in detail, including descriptions of experimental efforts, results of the experiments and models, and the major conclusions of each study. This research provides improved constitutive models and needed experimental data for evaluating and validating the long-term performance of subsurface CO_2 storage.

2. THEORETICAL MODEL FOR WATER ADSORPTION AND CAPILLARY CONDENSATION IN SUPERCRITICAL CO_2

2.1 Introduction

Large-scale geologic storage of CO_2 envisions injection of ~ 1 million metric tons per year of CO_2 at single subsurface target formations at depths > ~ 800–1000 m [12-14]. The process involves compression of CO_2 into a supercritical fluid phase with densities more similar to liquids than gases. The supercritical CO_2 ($scCO_2$) will be essentially anhydrous as surface transportation and pipeline operations require low-water-content CO_2 and no free water to limit corrosion of typical carbon-manganese steels [15]. Conceptual models in the literature assume a region of anhydrous separate-phase $scCO_2$ developing immediately around the wellbore as the formation brine is displaced and remaining water is evaporated [16, 17]. The anhydrous region is encompassed by a multiphase region of separate-phase $scCO_2$ and formation brine (i.e., the aqueous fluid) with mutually-dissolved CO_2 and water in each fluid phase, which is finally surrounded by native formation brine [8, 17, 18]. Of note is that the injected anhydrous $scCO_2$ will instigate change in the value of the chemical potential and activity (i.e., the "effective concentration") of water that is dissolved in the separate-phase $scCO_2$. The chemical potential of water, in general for multiphase-multicomponent porous media, determines the thickness of adsorptive water films and amount of pendular or capillary water [19-22]. The geometry of pore water impacts unsaturated flow and transport, and thus research in the vadose zone literature has focused on estimation of adsorptive film thickness, capillary water geometries, and approaches to upscaling for unsaturated hydraulic conductivity [22-25]. Recent work related to CO_2 storage also investigates the thickness of brine water films [26, 27]. The evolving activity of water in $scCO_2$ may thus impact several factors that affect performance of CO_2 storage sites, including so-called irreducible water saturation, relative permeability, and CO_2 injectivity and storage capacity.

Previous work in the CO_2 storage literature related to the changing magnitude of the chemical potential of water and/or adsorptive and capillary water focuses mainly on: 1) near-wellbore saline water evaporation and concomitant salt precipitation that may reduce $scCO_2$ injection rates due to permeability losses [16, 17, 28-30]; 2) chemical reactivity under humid $scCO_2$ including precipation-dissolution and water intercalation in clays as a function of water content in $scCO_2$ [7, 10, 31-36]; and 3) laboratory observation or theoretical estimation of thickness of water films in $scCO_2$ [26, 27, 37]. Common approaches for assessing near-wellbore dry-out, in calculating water activity in the CO_2-rich phase, typically neglect any effects of capillary potential or surface adsorption potential on the total chemical potential of water [e.g., see 36, 38]. By surface adsorption potential, we refer to attractive forces at solid surfaces that affect the formation of liquid films [see 19]. The common analytical or numerical-based model descriptions of near-wellbore drainage and imbibition processes may fail to capture processes that are dependent on the development or loss of adsorptive water films and capillary condensation, such as transport via water films and capillary imbibition "snap-off" or the spontaneous filling of pores with liquid water at a given chemical potential [e.g., see 22, 23; see Section 2 for details on the definition of "snap off" as used in this paper, 39]. Water vapor transport through the $scCO_2$ phase and capillary condensation in the original dry-out zone may not be fully accounted for by the commonly-used reservoir models.

Mineral precipitation and dissolution reactions under low-water CO_2 conditions have received much less attention than those of aqueous-phase-dominated systems [18], although the water-bearing CO_2 phase (i.e., water dissolved in CO_2) can mediate chemical reactions [40]. Recent work shows a dependency between of carbonation of a magnesium silicate mineral (i.e., forsterite) and brucite on water content in CO_2 [7, 10, 31-35]. A key finding indicates threshold behavior where higher water content in the CO_2 phase facilitates greater extent of carbonation, which we speculate relates to the thickness of water films and capillary water. In CO_2 at 95% saturation by water, nanometer-sized adsorptive water films produced 2% carbonation conversion, while in the presence of excess water (i.e., saturated CO_2) adsorptive films produced 10% conversion [33]. Molecular dynamics modeling indicates water film development on forsterite for water contents below saturation of water in $scCO_2$ [32]. Desiccation of clays represents a potential mechanism for creation and/or exacerbation of permeable pathways in caprock, thus posing risk to storage integrity [18, 41]. Schaef et al. [42] and Ilton et al. [43] point out potential drying and/or expansion of clay (i.e., low iron montmorillonite saturated with Na^+ or Ca^{2+}) under hydrostatic stress using *in-situ* X-ray diffraction. They show that the initial amount of interlayer water (i.e., the degree of hydration and number of interlayer waters) and thus the activity of water govern expansion or collapse of interlayer spacing. Schaef et al. [42] demonstrate vapor transport of water through $scCO_2$ into the interlayer spacing of clay.

Kim et al. [27] experimentally observed water films under multiphase conditions in air (at 45°C and at ~ 0.1 MPa) and $scCO_2$ (at 45°C and ~8.5 MPa) using silica micromodels. Degassed brine was the initial phase in the micromodels and air or CO_2 was then injected. The CO_2 was presaturated with gas prior to injection. Following completion of drainage, the micromodel were closed and left to equilibrate. Stable water films were observed for the air-water case during and after drainage. Quantitative measurements of film thickness were not provided. The CO_2-brine experiments exhibited initially "thick" water films, water film thinning, and water droplet formation. Kim et al. invoke intermolecular interactions to explain their results: protonation of the silica surfaces occurs as CO_2 dissolves into brine and lowers the pH; the resulting lower surface charge compresses the electric double layer and destabilizes the brine film, especially under high ionic strength; and CO_2 is physisorbed by silanol groups on the silica surface. Water activity in these experiments probably varied greatly due to a range in ionic strengths (0.01–5.0 M), but was not specially investigated in its relation to water film thickness or dewetting behavior. Tokunaga [39] presents a Derjaguin-Landau-Verwey-Overbeek (DLVO) model to estimate water film thicknesses on flat mineral surfaces for subcritical- to $scCO_2$ conditions, incorporating effects of van der Waals and electrostatic forces on film thickness. Film thicknesses were typically less than 10 nm. The water film model displays the controls on thickness including electrostatic and van der Waals interactions, where higher salinity and lower surface charge result in thinner films, and the model can assess the thicknesses relative to mineralogy (e.g, smectite estimated to have thicker films than silica). Kim et al. [26] experimentally measured brine film thickness in $scCO_2$ (at 7.8 MPa and 40°C) at matric potentials (combination of adsorptive surface and capillary potential) ranging from 0.18–3.7 kPa, observing thicknesses of ~ 2 nm on smooth surfaces (1.6 nm root mean square roughness (Rrms)), and 265 and 249 nm at matric potentials of 0.18 and 3.7 kPa, respectively, on rough surfaces (330 Rrms). Their approach involved sapphire and silica disks for the location of the brine films, and an apparatus to control the applied matric potential. Film thickness was measured using tracers and X-ray fluorescence. Estimation of film thickness for these

experiments with the flat-film DLVO approach of Tokunaga [39] overestimated the measured film thickness on the flat surfaces, probably because the model is only approximate for high ionic strength (2 M in this case). The DLVO approach underestimated the rough-surface films, probably because the model neglected capillarity, which will increase liquid saturations on the rougher surfaces.

In this paper, we present the theory and results of a pore-scale model on the configuration of liquid water films as an explicit function of chemical potential of water in partially-saturated porous media, with a focus on the CO_2-water system. Extending Tokunaga's [39] water film model for flat mineral surfaces, we incorporate water adsorption in the CO_2-water-mineral system as a term in the augmented Young-Laplace equation [20, 22], which expresses the chemical potential of water as a function of both adsorptive and capillary components. The capillary component allows for more realistic pore geometries including wedge-shaped pores, which facilitates our examination of the importance of capillary condensation and degree of saturation (i.e., liquid water volume fraction of pore space) of a pore unit cell. Our approach follows that of studies for the air-water-mineral system of the vadose zone [22, 44], using the air-water-mineral interfaces as a reference for interpretation of the CO_2-water-mineral system. We investigate water saturation and imbibition "snap off" in triangular and square pores under varying chemical potential and water activities in $scCO_2$. As used in this paper, imbibition snap off refers to the spontaneous filling of a pore with liquid water as discussed in the vadose zone literature [e.g., see 22; see Section 2 for more detail for comparison to other uses of the term snap off by the petroleum and CO_2 storage literature]. Our investigation includes the reservoir conditions at depths of 0, 1000, and 2000 m for the CO_2-water system. We also include the air-water system of the vadose zone and at deeper depths (for the nitrogen-water system) as a point of reference. Our findings show that chemical potential has a strong control on water saturations in pores of different sizes, with the CO_2-water saturations being much less than those of the air-water system of the vadose zone. Imbibition snap off in large pores of conventional reservoir rocks requires relatively high values of chemical potential or water activity than pores in tight gas sandstones or shales.

2.2 Theory of Aqueous Films in Supercritical CO_2

2.2.1 Overview of Chemical Potential, Water Activity, Adsorption, and Capillarity

Phillip [20] presents a "unitary approach" for quantitatively assessing how adsorption and capillarity govern the configuration of liquid water in partially-saturated porous media. Tuller et al. [22] recognize that the unitary approach is a modified version of the Young-Laplace equation, deemed the augmented Young-Laplace (AYL) equation, in which an adsorptive term is added to the expression of capillarity. The fluid-fluid (e.g., liquid water–CO_2 phase; or water-air) interface represents a surface of specific partial molar Gibbs energy or chemical potential μ of water. Herein we specifically consider the matric potential portion of the total water potential, which has adsorptive ($\mathcal{A}$) and capillary ($\mathcal{C}$) components [22]. We use $\Delta\mu$ to express the change in energy from the reference standard state $\mu°$:

$$\Delta\mu = \mathcal{A}(D) + \mathcal{C}(c) \tag{2-1}$$

where D is the adsorptive film thickness; and c is the mean curvature of the fluid-fluid interface. We assume that the matric potential of Equation 1 represents the work performed by an infinitesimal amount of water when it moves from a reference reservoir of free (i.e., no surface forces) water to the unsaturated confined pore at the same elevation. We are not incorporating the osmotic potential; thus, the reservoir and confined pores can both contain solutes. The water in the confined pore may contain solutes, which will affect the adsorptive component of Equation 2-1 (see the information on the electrostatic component of the disjoining pressure described below). Figure 1a illustrates the pore space of a typical quartz-rich sandstone with pore shapes that would, under partially-saturated conditions, result in flat adsorptive films and capillary water in the wedge-shaped corners of the pores, as shown conceptually in part b. Part b illustrates that a change in the angle of a pore corner affects the relative amount of capillary water (three angles are shown: 30°, 60°, and 90°; although part b is schematic, the water-CO_2 interfaces were calculated with our interface model described in Section 2.2.2 and are based on the results of Figure 3). Different values of the chemical potential of water in the CO_2 (or the liquid water—the chemical potentials in the two phases are equal) will result in different configurations of the capillary water and thicknesses of adsorptive films (see Figure 1b).

The adsorptive component of Equation 2-1 is typically expressed by the disjoining pressure (in the following it is expressed in units of pressure or energy per volume), which is the derivative of the Gibbs energy interaction per unit area in the direction normal to the interacting repulsive or attractive solid-fluid and fluid-fluid interfaces (i.e., the interfaces that bound the adsorptive film):

$$\Pi(\mathrm{D}) = -\frac{1}{\mathrm{A}}\left(\frac{\partial \mathrm{G}}{\partial \mathrm{D}}\right)_{\mathrm{T,V,A}} \tag{2-2}$$

where G is the work to thin an infinitely-thick film to a finite thickness D; T is temperature; V is volume; and A is area [22]. The types of intermolecular interactions represented in the disjoining pressure are typically the following [22]:

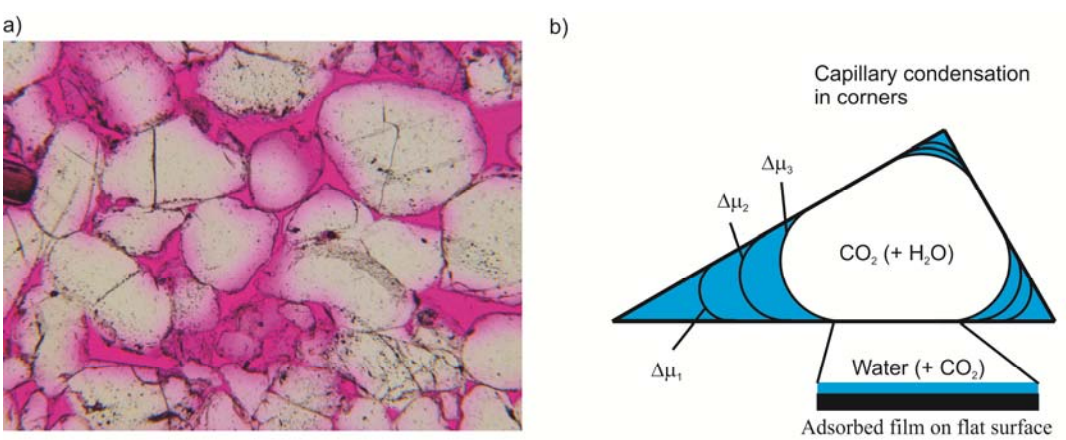

Figure 1. a) Thin section image of a quartz-rich sandstone (the Mount Simon Sandstone). Pore space is filled with pink epoxy. b) Schematic of a single triangular pore in an unsaturated CO_2 storage reservoir rock, showing liquid water (in blue) in corners and on flat pore surfaces as a function of three values of the chemical potential of water.

$$\Pi(D) = \Pi_{vdW}(D) + \Pi_e(D) + \Pi_s(D) \tag{2-3}$$

where the subscript vdW indicates van der Waals forces; *e* represents electrostatic interactions; and *s* is the structural term. The structural term may represent changes in water properties near surfaces that may include water density or the dielectric constant. The structural term is cited as the origin of hydration repulsion [22].

The Kelvin equation for a single component vapor and condensed fluid phase, and considering only adsorption, is related to disjoining pressure by the following:

$$\Pi(D) = -\frac{RT}{V_m}\ln\left(\frac{p}{p_{sat}}\right) \tag{2-4}$$

where R is the gas constant; T is temperature; V_m is molar volume of the liquid; and p/p_{sat} is the relative vapor pressure at the temperature of interest. If the condensed fluid phase is pure water, Pw/P_{sat} equals the activity of water with a value of one if the bulk water (corresponding to an infinitely thick film) is present. For the multiphase-multicomponent system with capillarity and surface potentials, the Kelvin equation is the following, expressed in terms of the ratio of activity coefficients [19]:

$$\frac{\mathbb{A}_\beta^\gamma}{\mathbb{A}_\alpha^\gamma} = \mathcal{K}_{\beta,\alpha}^\gamma(p_0,\overline{T})\exp\left\{\left[-\upsilon_\alpha^\gamma\left(\frac{2\widetilde{\sigma_{\alpha\beta}}}{c_{\alpha\beta}}\right)^{\alpha\beta} + \widetilde{\varphi_{s\alpha}^{\gamma\alpha\beta}}\right]M^\gamma/R\overline{T}\right\} \tag{2-5}$$

where $\mathbb{A}_\beta^\gamma$ and $\mathbb{A}_\alpha^\gamma$ are the macroscopic activity coefficient of the γ component (e.g., water) in the α or β phase (in the liquid water phase or separate CO_2 phase); $\mathcal{K}_{\beta,\alpha}^\gamma$ is the partitioning coefficient of the γ component of between the α or β phases; p_0 is the pressure at the reference reservoir; $\overline{T}$ is absolute temperature that is uniform over the α or β phases (e.g., water and CO_2); υ_α^γ is the partial volume of the γ component in the α phase; $\sigma_{\alpha\beta}$ is the interfacial energy between α and β phases; $c_{\alpha\beta}$ is the mean radius of curvature of the α–β interface; $\varphi_{s\alpha}^{\gamma\alpha\beta}$ is the partial surface potential minus the gravitational potential of component γ, which is due to surface forces acting on phases α or β, where the tilde overbar indicates the surface average over the α-β surface; and M^γ is the molecular mass of γ component. Equation 2-5 shows that both capillarity and the surface potential affect phase equilibrium for multicomponent-multiphase systems. Which effect is dominant depends in large part of the size of the adsorptive films in relation to the size of the pores and the degree of capillarity (or angle of wedge-shaped pores).

A full derivation using fundamental thermodynamic expressions of the relationship between chemical potential and activity of water for the CO_2-brine-mineral system in porous media requires careful simultaneous treatment or incorporation of the following: the multicomponent, multiphase Kelvin equation that accounts for mutual dissolution of CO_2 and water (and other gaseous components) into these fluid phases; adsorption of liquid water containing dissolved CO_2 on mineral surfaces, with charge regulation of the mineral surface due to pH lowering as CO_2 dissolves; upscaling of microscopic to macroscopic potentials (Equation 2-5 is an example of using macroscopic potentials); osmotic and surface potentials in the context of disjoining pressure of thin films where higher salinity collapses double layers and provides for thinner

films, whereas osmotic potentials would tend to thicken films; and capillary forces where the interfacial energy of the CO_2-water fluid-fluid interface varies as a function of the adsorptive film thickness. For examples of in-depth, thermodynamic derivations for unsaturated soils, see Bear and Nitao [45] and Nitao and Bear [19]; however, note that these authors do not address many of the specific concerns listed above. The full derivation for the CO_2-water-mineral unsaturated porous medium system is beyond the scope of this study. We focus on a simplified system as discussed below that combines adsorption and capillarity, but ignores the osmotic potential.

Section 2.2.2 presents typical methods for estimating the vdW and electrostatic components of disjoining pressure, as applied to the CO_2 system. Adapting Tuller et al.'s [22] approach requires incorporation for the electrostatic component of disjoining pressure (we do not incorporate the structural component here). Tuller et al. [22] only used the vdW component of disjoining pressure. Section 2.2.3 addresses the solution of Equation 2-2 for the location of the fluid-fluid interface as presented by Tuller et al. [22] for the air-water system, but with explicit focus on the CO_2-water system. Section 2.2.3 makes explicit the link between chemical potential and the capillary and adsorptive terms for wedge-shaped pores in terms of the location of the fluid-fluid interface.

2.2.2 Adsorption of Water Films and Disjoining Pressure

2.2.2.1 van der Waals Component

The van der Waals component of the disjoining pressure for a flat film is given by [46]:

$$\Pi_{\mathrm{vdW}} = -\frac{A_{132}}{6\pi D^3} \tag{2-6}$$

where A_{132} is the Hamaker constant for media 1 and 2 interacting across medium 3; and D is the flat film thickness. In our case, subscripts of A_{132} are the following: 1) solid phase; 2) H_2O-rich phase; and 3) CO_2-rich phase. A_{132} can be calculated for pure or mixed H_2O and CO_2 phases. A positive value of Π_{vdW} (i.e., A_{132} negative) indicates repulsive pressure or the tendency of solid-water and water-CO_2 interfaces to disjoin or separate from each other.

The following combining relation is used to calculate the nonretarded Hamaker constant [46]:

$$A_{132} \approx \left(\sqrt{A_{11}} - \sqrt{A_{33}}\right)\left(\sqrt{A_{22}} - \sqrt{A_{33}}\right) \tag{2-7}$$

where A_{ii} is the Hamaker constant for pure medium i interacting with itself across vacuum. A_{ii} is obtained by a simplification of Lifshitz theory [46-48]:

$$A_{ii} = \frac{3}{4} k_b T \left(\frac{\varepsilon_i - \varepsilon_{vacuum}}{\varepsilon_i + \varepsilon_{vacuum}}\right)^2 + \frac{3h\nu_e}{16\sqrt{2}} \frac{\left(n_i^2 - n_{vacuum}^2\right)^2}{\left(n_i^2 + n_{vacuum}^2\right)^{3/2}} \tag{2-8}$$

where k_b is the Boltzmann constant (i.e., 1.381×10^{-23} J K^{-1}); T is temperature in Kelvin; ε is dielectric constant; n is refractive index; h is Planck's constant (6.626×10^{-34} J s); ν_e is the

maximum electronic ultraviolet adsorption frequency (e.g., 3×10^{15} s^{-1}). The values of ε_{vacuum} and n_{vacuum} are set to 1.
The values of ε and n for H_2O-rich phases with dissolved CO_2, and CO_2-rich phases with dissolved H_2O, herein referred to as mixed phases, are calculated using the Lorentz-Lorenz mixing rule [48]:

$$\frac{(n_{mix}-1)^2}{(n_{mix}+2)^2} = \sum \frac{\phi_i (n_i-1)^2}{(n_i+2)^2} \tag{2-9}$$

$$\phi_i = \frac{x_i V_{m,i}}{\sum x_i V_{m,i}} \tag{2-10}$$

where ϕ_i is the volume fraction of component i.

Tokunaga [39, Table 1] presents estimates for A_{132} for the CO_2-water system with minerals of quartz and smectite for a range of pressures and temperatures. For simplicity and to facilitate comparison with previous work, in Section 3 we use his A_{132} values quartz for depths of 0, 1000, and 2000 m for calculations involving the AYL equation (Table 1). For comparison with estimate film thickness of the vadose zone, we choose the A_{132} value of of -1.9×10^{-19} J for the air-water-mineral system as given by Tuller et al. [22]. Air-water A_{132} values for depths of 1000 and 2000 m use those of pure nitrogen at the relevant temperatures and pressures (Table 1).

2.2.2.2 Electrostatic Component

The Poisson-Boltzmann (PB) equation is the basis of the electrostatic component of the disjoining pressure. The PB equation incorporates charge and electrostatic potential of the interfaces (in our case the solid-water and water-scCO_2 interfaces) to calculate the net excess charge density at a distance normal to the solid-fluid and fluid-fluid interfaces. The PB equation can be solved to obtain the electrostatic term of the disjoining pressure between the interfaces. For the CO_2-water system, Tokunaga [39] investigates the following two solutions to the PB equation: the double-layer compression approximation by Gregory [49]; and the linear superposition approximation (LSA) [50]. The Gregory solution is suitable for low- to intermediate-magnitude charge potentials on mineral-fluid and fluid-fluid interfaces. For a range of ionic strength of a 1:1 symmetric salt (e.g., NaCl as opposed to $CaCl_2$) up to moderate values [39], the Gregory solution was shown to be similar to the LSA solution (< 5% different) [see 39]; thus, we use this solution in Section 3. The Gregory solution is given by the following:

$$\Pi_e = n_\infty k_b T \left[2\left(1 + \frac{(Y_{e,1}+Y_{e,2})^2}{4}\operatorname{csch}^2(\kappa D/2)\right)^{1/2} - \frac{(Y_{e,1}-Y_{e,2})^2 \exp(-\kappa D)}{1+\frac{1}{4}(Y_{e,1}+Y_{e,2})^2 \operatorname{csch}^2(\kappa D/2)} - 2 \right] \tag{2-11}$$

Table 1. Values of Properties used in CO_2-Water-Mineral Model of Adsorptive Films and Capillary Water at Three Depths

	Depth (m)		
Property	**0**	**1000**	**2000**
Temperature (K)	293	323	353
Pressure (MPa)	0.1	10.6	21.1
Air-water σ (N m^{-1})	0.072[a]	0.063[b]	0.056[c]
CO_2-water σ (N m^{-1})	0.075	0.029	0.026
ρ_{H2O} (kg/m^3)	998	989	975
ε_{H2O}	80.25	69.93	60.89
A_{132} (quartz) (J)	-1×10^{-20}	-6.8×10^{-21}	-5.6×10^{-21}
ψ_1 (quart-water) (mV)	0	0	0
ψ_2 (water-CO_2) (mV)	-25	-25	-25
n_∞ (mol m^{-3})	100	100	100

Notes: Temperature, pressure, depth, CO_2-water interfacial tension, water density, water dielectric constant, and the quartz-water-CO_2 Hamaker constants were taken from Tokunaga [39]. The surface potentials ψ and the bulk concentration n are for a base case. [a]Value taken from Tuller et al. [1999]. [b]Interfacial tension data for of the pure N_2 and water system, at temperature and pressure of 333.15 K and 10.0 MPa, respectively, from Yan et al. [51]. [c]Interfacial tension data for of the pure N_2 and water system, at temperature and pressure of 353.15 K and 20.0 MPa, respectively, from Yan et al. [51].

where n is the ion density of the bulk fluid (saline water in our case); k_b is the Boltzmann constant; T is temperature; $Y_{e,1}$ and $Y_{e,2}$ are the dimensionless electrostatic potential at the two Gibbs dividing surfaces (i.e., the mineral-fluid and fluid-fluid interfaces); and κ is the Debye-Hückel reciprocal length parameter; and D is the distance normal to the two Gibbs dividing surfaces. The parameters $Y_{e,i}$ (where subscript i equals 1 or 2 to represent the two surfaces) and κ are given by:

$$Y_{e,i} = \frac{ze\psi}{k_b T} \tag{2-12}$$

$$\kappa^2 = \frac{2e^2\rho z^2}{\varepsilon k T} \tag{2-13}$$

where z is the ion valence; e is the electron charge; and ψ is the electrostatic potential . Equation 2-11 is combined with Equation 2-6 to give the total disjoining pressure for use in the AYL equation (see Section 2.2.3 for more detail).

2.2.2.3 Extension of the Augmented Young-Laplace Equation for CO_2-Water Systems

Tuller et al. [22] present two approaches for calculating liquid-vapor interfaces of a unit cell. They modify Philip's "unitary approach" [20, 21] with the modern version of the vdW component of disjoining pressure. The first approach simultaneously combines adsorptive and

capillary contributions through the AYL equation (Equation 1). The second, the shifted Young-Laplace (SYL) equation, treats capillarity separately and then shifts the curved interface by the constant adsorptive film thickness as calculated independently at the same chemical potential. In the following, we extend the AYL approach to include the electrostatic component of disjoining pressure to accommodate aqueous and subcritical to supercritical CO_2 fluid phases. We recapitulate the solution of Philip [20] and Tuller et al. [22] with an explanation of the steps required to incorporate the expanded adsorptive term.

Replacing the capillary term *C(c)* of Equation 2-1 to explicitly express the energy associated with curvature of the interface of the fluid pair gives

$$\mu = \mathcal{A}(y) - \frac{\sigma}{\rho}\nabla \cdot n \tag{2-14}$$

where μ is the chemical potential of the interface; $\mathcal{A}(y)$ is the adsorption term with y as the interface location and, particularly for the adsorption term, the thickness of the flat film; σ is the interfacial energy for the fluid pair; ρ is density of the wetting or aqueous phase; and $\boldsymbol{n}$ is the interface unit normal vector. In 2D Cartesian coordinates, the divergence of $\boldsymbol{n}$ (with units of 1/L) is expressed in the AYL equation as

$$\mu = \mathcal{A}(y) - \frac{\sigma}{\rho}\frac{y''}{(1+(y')^2)^{3/2}} \tag{2-15}$$

where primes indicate derivatives with respect to spatial coordinate *x*. Solution of Equation 2-15 for two parallel plates forms the basis for calculating the interface in a wedge-shaped pore. The parallel plate solution is

$$x(y) = \int_y^Y \left(\left(\frac{\sigma}{\rho u(y_1)}\right)^2 - 1\right)^{-1/2} dy_1 \tag{2-16}$$

with

$$u(y_1) = \int_{y_1}^Y (\mu - \mathcal{A}(y))dy \tag{2-17}$$

$$\mathcal{A}(y) = \frac{\Pi(y)}{\rho} \tag{2-18}$$

$$\Pi(y) = \Pi_{vdW}(y) + \Pi_{el}(y) + \Pi_s(y) \tag{2-19}$$

where *Y* is the half of the slit distance (Figure 2a); *Π* is disjoining pressure for the flat fluid interface, with subscripts *vdW*, *e*, and *s* indicating van der Waals, electrostatic, and structural terms (the structural term is neglected here). The capillary and adsorptive components of the AYL equation are met at a particular value of the equilibrium chemical potential, which is given by this iterative equation:

$$\mu_{n+1} = \frac{-\frac{\sigma}{\rho} + \int_{\mathcal{A}^{-1}(\mu_n)}^{Y} \mathcal{A}(y)dy}{Y - \mathcal{A}^{-1}(\mu_n)} \tag{2-20}$$

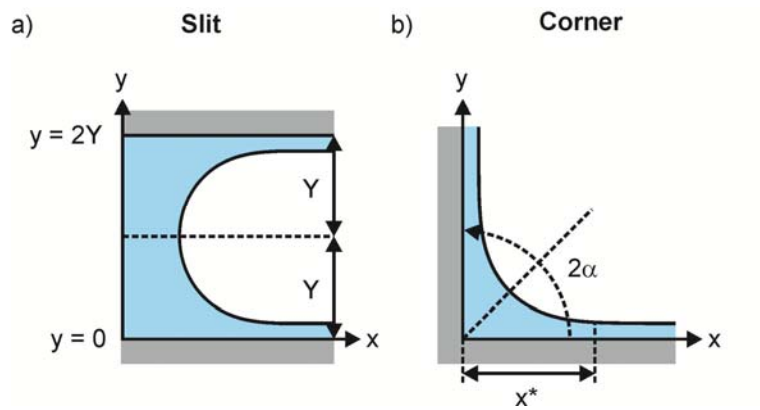

Figure 2. Schematic diagrams fluid-fluid interfaces in slit and corner geometries. a) Slit geometry defined by two parallel plates with Y as half the slit distance. b) Corner geometry with 2α as the angle between two planes. x* is the distance at which the curved fluid-fluid interface becomes equal to adsorptive film thickness. Modified from Tuller et al. [22].

where the inverse of the sorption term $\mathcal{A}^{-1}(\mu_n)$ represents the adsorptive film thickness.

Our goal is to obtain the fluid interface as a function of chemical potential for the wedge. The solution requires reflecting the parallel-plate-solution of the fluid interface across a plane of symmetry, where the wedge angle is 2α ($0 < \alpha < 2\pi$) (see Figure 2b). The point at which interface intersects the symmetry plane normally is y_{α}, given by

$$u(y_\alpha) = -\frac{\sigma \sin(\alpha)}{\rho} \tag{2-21}$$

Rearranging Equation 2-20 provides an iterative approach for determining *Y* at a given chemical potential

$$Y_{n+1} = \frac{-\frac{\sigma}{\rho} + \int_{\mathcal{A}^{-1}(\mu)}^{Y_n} A(y)dy}{\mu} + \mathcal{A}^{-1}(\mu_n) \tag{2-22}$$

This *Y* is used as the upper limit of integration, with y_α as the lower limit, for the $u(y_\alpha)$ integral (Equation 2-17). Once y_α is obtained, it becomes the upper limit of integration of Equation 2-15. The *u(y)* term that is plugged in Equation 2-14 uses the *Y* of Equation 2-22 as the upper limit of integration.

Tuller et al. [22] only used the van der Waals term of Equation 2-19 for calculating the interface, given as

$$\Pi_{vdW}(y_1) = \frac{A_{132}}{6\pi y_1^3} \tag{2-23}$$

where subscripts of the Hamaker constant *A* refer to phases *1* (e.g., quartz) and *2* (e.g., CO_2) interacting across phase *3* (e.g., water). The electrostatic component of the disjoining pressure

can be represented by solutions to the Poisson-Boltzmann equation, one is which is Gregory's [49] for unequal plates at constant charge (see Section 2.2.2.2), which we use herein:

$$\Pi_e(y_1) = n_\infty kT\left[2\left(1+\frac{(Y_{e,1}+Y_{e,2})^2}{4}\operatorname{csch}^2\left(\frac{\kappa y_1}{2}\right)\right)^{1/2} - \frac{(Y_{e,1}+Y_{e,2})^2\exp(-\kappa y_1)}{1+\frac{1}{4}(Y_{e,1}+Y_{e,2})^2\operatorname{csch}^2\left(\frac{\kappa y_1}{2}\right)} - 2\right] \tag{2-24}$$

$$Y_e = \frac{ze\psi_e}{k_b T} \tag{2-25}$$

$$\kappa^{-1} = \sqrt{\frac{\varepsilon_0\varepsilon_r kT}{2e^2z^2n_\infty}} \tag{2-26}$$

where the definitions of the parameters are given in Section 2.2.2; however, not that the film thickness D has been replaced by y_1, which is used in the specific solution of the interface equations (e.g., Equation 2-16).

In Section 2.2.3, values of -25 and 0 mV are used for the electrostatic component of the disjoining pressure for the solid (quartz)-water and water-CO_2 interfaces, and an aqueous concentration of a 1:1 symmetric salt of 100 mol/m^3. Little data in the literature exists for the electrostatic potential of the CO_2-water interface; Tabor et al. [52] for approximately atmospheric conditions measure surface potentials close to 0 mV. For more information on the influence of these parameters on flat adsorptive film thickness, see Tokunaga [39]. In general, Tokunaga [39] demonstrates that higher salinity or a greater difference in the positive and negative electrostatic potential terms ψ of the solid-water and water-CO_2 interfaces tend to result in thinner adsorptive water films.

In this paper, we use the term imbibition "snap off" to refer to the situation where the following occurs: the growth of adsorptive water films and capillary water progressively increases as the chemical potential achieves less negative values (i.e., less negative equals higher water activities). In this case the chemical potential of water in the separate-phase air or CO_2 thus can control the growth of the liquid films and capillary water in contrast to filling of pores by advective flow. Once the water configuration becomes an inscribed circle in a pore of a given geometry, we assume that the pore spontaneously fills or "snap offs." Prior to imbibition snap off, the water configuration model of Section 2 describes the location of the water-CO_2 or water-air interfaces as the pore fills with water. After snap off, however, the water interface readjusts itself as the pore continues to fill and the model no longer applies [see 22, for more detail on imbibition snap off]. This usage is common in the vadose zone literature [e.g., see 22] and thus is used herein. However, note that in the CO_2 storage or petroleum literature, snap off may also refer to the water phase occupying pore throats and trapping residual separate-phase CO_2 or oil within the larger pore body.

2.3 Results of the CO_2-Water Meniscus Model

Figure 3 presents the location of CO_2-water menisci in wedge-shaped pores for the geologic pressure and temperature conditions of 0, 1000, and 2000 m depths as compared to the air-water interface of the vadose zone and pure nitrogen for the depths of 1000 and 2000 m (see Table 1 and Section 2.2 for parameter values). The film thicknesses on flat surfaces for CO_2-water case, for progressively deeper depths, are 1.8, 1.67, 1.57 nm, respectively, which indicate a slight change to thinner films with depth. In contrast, for the three progressively deeper depths, the air-water flat film thicknesses are 1.7, 1.7, and 1.8 nm, which suggests the tendency of the CO_2 system to produce thinner water films than the air-water system with depth and is also the conclusion reached experimentally by Kim et al. [27]. The curved portion of the menisci represents the contribution of capillarity. Less capillary water for the CO_2-water system water (i.e., the menisci is compressed towards the apex of the wedge) with depth as compared to the air-water system is due to the greater change to lower interfacial tension values of the CO_2-water system (Table 1). Note that because the AYL combines the energy contributions from both capillarity and adsorption, the thinner water films in CO_2 may also contribute to less capillary as compared to the air-water case, but the interfacial tension effect is probably dominant. Comparison of part a to parts b and c of Figure 3 illustrate that the amount of capillary water dramatically increases as wedge angles lower from 60° to 30°. Thus, the angle of the wedge-shaped pore affects the degree of saturation, with smaller wedge angles containing substantially more water. This has implications on textural controls; for example, more slit-like or narrow pores will contain much more capillary water.

Using the wedge-shapes, equilateral triangular pores of 1×10^{-8} m (0.1 μm) and 1×10^{-5} m (10 μm) long on a side are assembled in Figure 4. These sizes are chosen as they fall within pore-throat size ranges of typical shales, tight sandstones, and conventional reservoirs rocks [ranges are, respectively, 0.1–0.005, 2–0.03, and > 2 μm; 53]. The air-water interfaces, for the vadose zone, form inscribed circles in the pores, which are considered the point at which spontaneous filling or imbibition "snap-off" of the pores will occur during imbibition [22]. In the air –water system, the matric potentials of water at imbibition snap-off for these 1×10^{-8} m (0.1 μm) and 1×10^{-5} m (10 μm) sized pores are calculated to be -30640 and -25.0 J/kg, respectively. Using these same calculated water potentials for snap-off in the air-water case, the CO_2-water interfaces are calculated for the respective pore sizes. These show a large decrease in the portion of the pore filled with water and thus imbibition snap-off will not occur for the CO_2-water cases unless the chemical potential achieves less negative values (or higher water activities). These results suggest that for CO_2-water systems, pore and upscaled rock saturations will be lower than in vadose zone systems at a given water matric potential, and higher matric potentials are required to achieve snap-off and pore filling.

Figure 5 illustrates the pore-filling water saturation paths for equilateral triangular pores of sizes ranging from 1×10^{-8} m to 1×10^{-4} m. Groups of three curves for the vadose zone air-water, 1000-mCO_2-water, and 2000-m CO_2-water cases are shown for a given pore sizes (labeled above the curves). The circles at the top of the curves represent the point of imbibition snap off, after which our model no longer applies. The highest saturations at snap off are achieved for the smallest pore sizes (see the group of curves for 1×10^{-8} m), which indicates that at the smallest

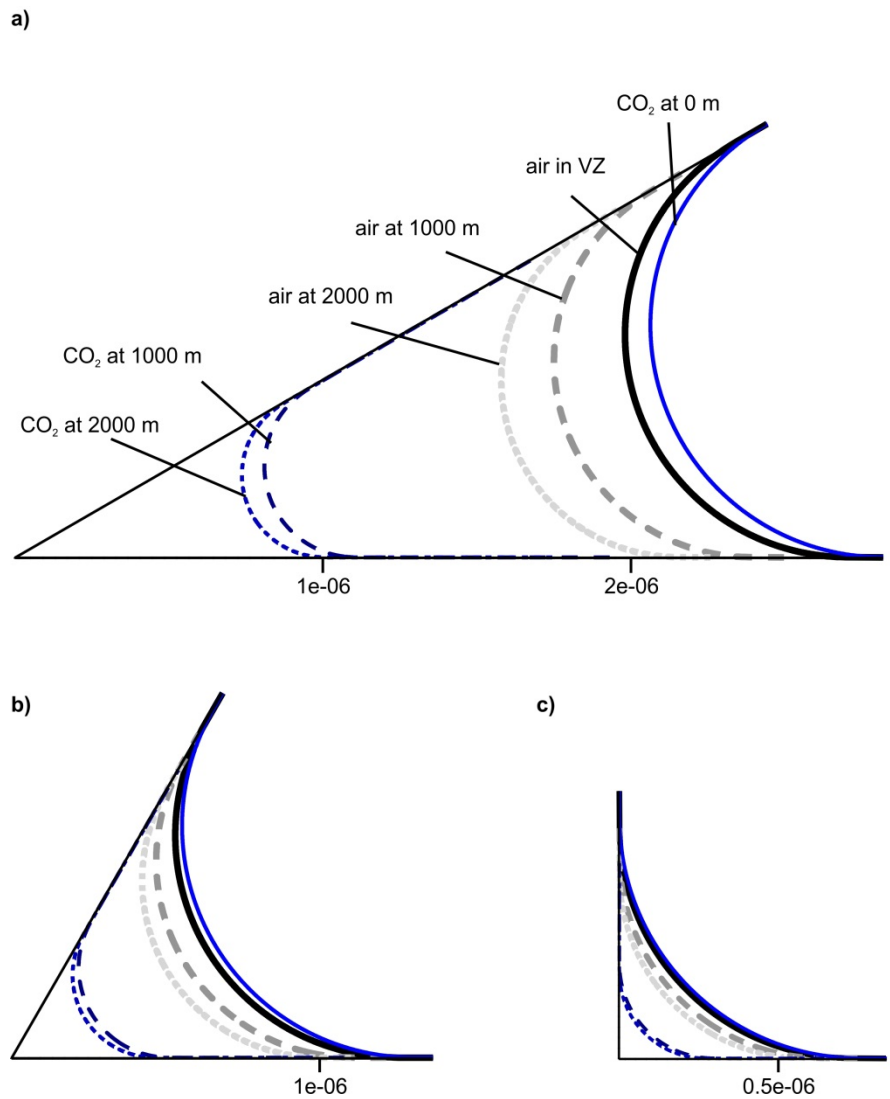

Figure 3. Liquid water menisci at the matric potential of -100 J/kg for air-water and CO_2-water cases in wedge-shaped pores with wedge angle of: a) 30°; b) 60°; and c) 90°. The annotated distances are in units of meters. "VZ" stands for vadose zone.

sizes, the adsorptive film thickness contributes to the saturation (see Figure 4 and the relative sizes of the adsorptive films for the pore sizes of 1×10^{-8} m and 1×10^{-5} m). Pore sizes of approximately 1×10^{-6} m and larger show similar maximum saturations, which indicates that the adsorptive films contribute much less to the saturation than the capillary water as the curves approach imbibition snap off. Pore-throat sizes of tight gas sandstones and shales encompass the range of sizes where saturations are affected by the adsorptive film thickness (see the upper annotation of Figure 5).

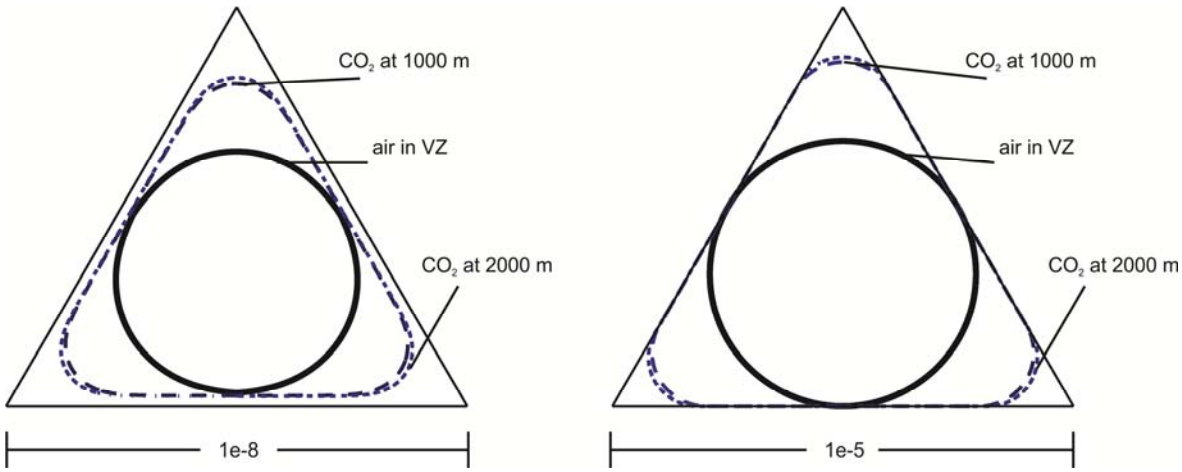

Figure 4. Air-water and CO_2-water menisci in 1 ×10^{-8} and 1 ×10^{-5} m equilateral triangular pores. The air-water meniscus forms an inscribed circle, which represents imbibition "snap off". For each pore, respectively, the CO_2-water menisci are calculated at the same chemical potential as the air-water interface.

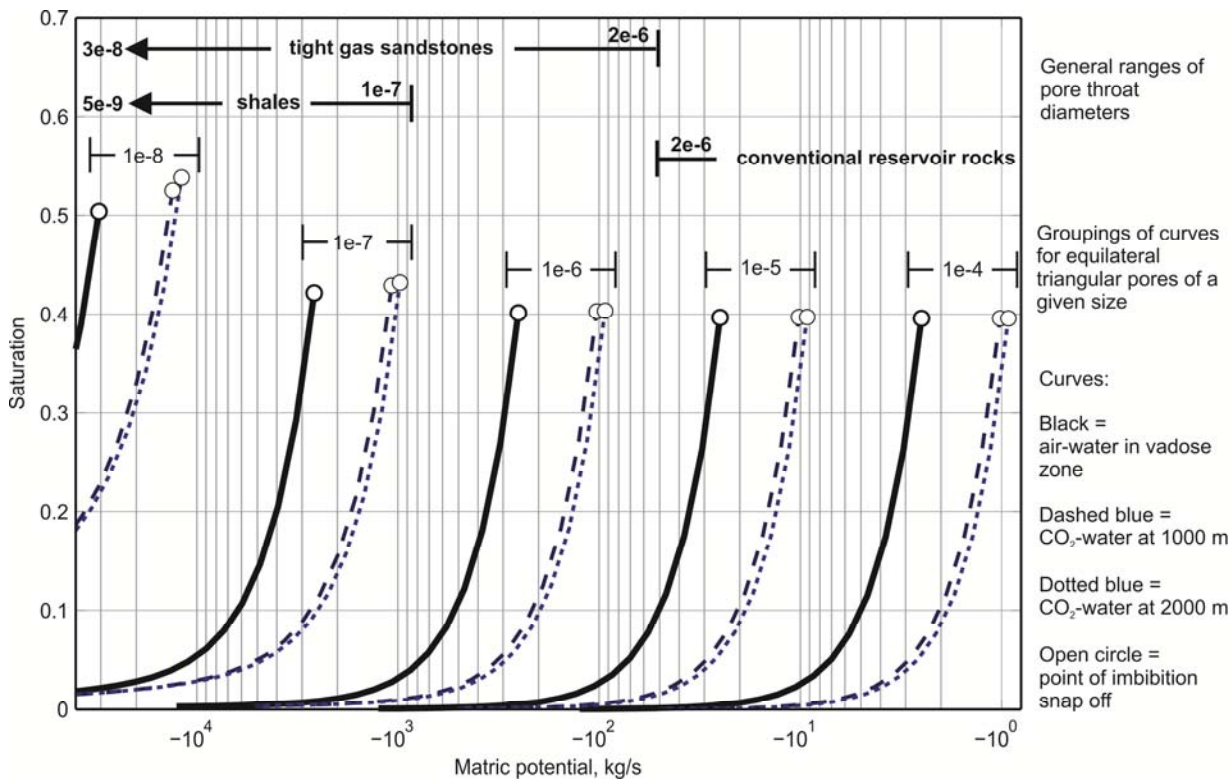

Figure 5. Saturation of triangular pores as a function of the matric potential. Groups of three curves at different pore sizes (labeled with units of meters) are shown. Thus, one set of curves is the saturation path taken by a pore of a fixed size as the chemical potential of water increases for the air-water or CO_2-water system. The general range of pore throat sizes (in units of meters) from Nelson [53] is given at the top of the plot.

Figure 6a presents the matric potential at imbibition snap-off in triangular or square pores of a given size (the *y* axis is the length of the side of the triangular or square pore) for the vadose zone air-water and CO_2-water system at 1000 and 2000 m. The matric potentials were determined by iteratively solving for the shape of the menisci until they reached the shape of an inscribed circle. The relationship is linear in log-log space. At a given pore size and shape (triangle or square), imbibition snap-off for the CO_2-water system requires less-negative chemical potentials and thus greater activities of water. Assuming that the water matric potential of the CO_2 phase in the pore-scale model can be related to that of the activity of water through $\Delta\mu_{H2O} = RTln(a_{H2O\text{-}aq})$ (which is an important assumption and does not use the more complicated Equation 2-5; see Section 2.2), Figure 6a is replotted as a function of activity of water in Figure 6b. The activity of water, based on the matric potential, thus may need to be greater than 0.95 for imbibition snap off to occur for pores equal to or larger than 0.1 μm.

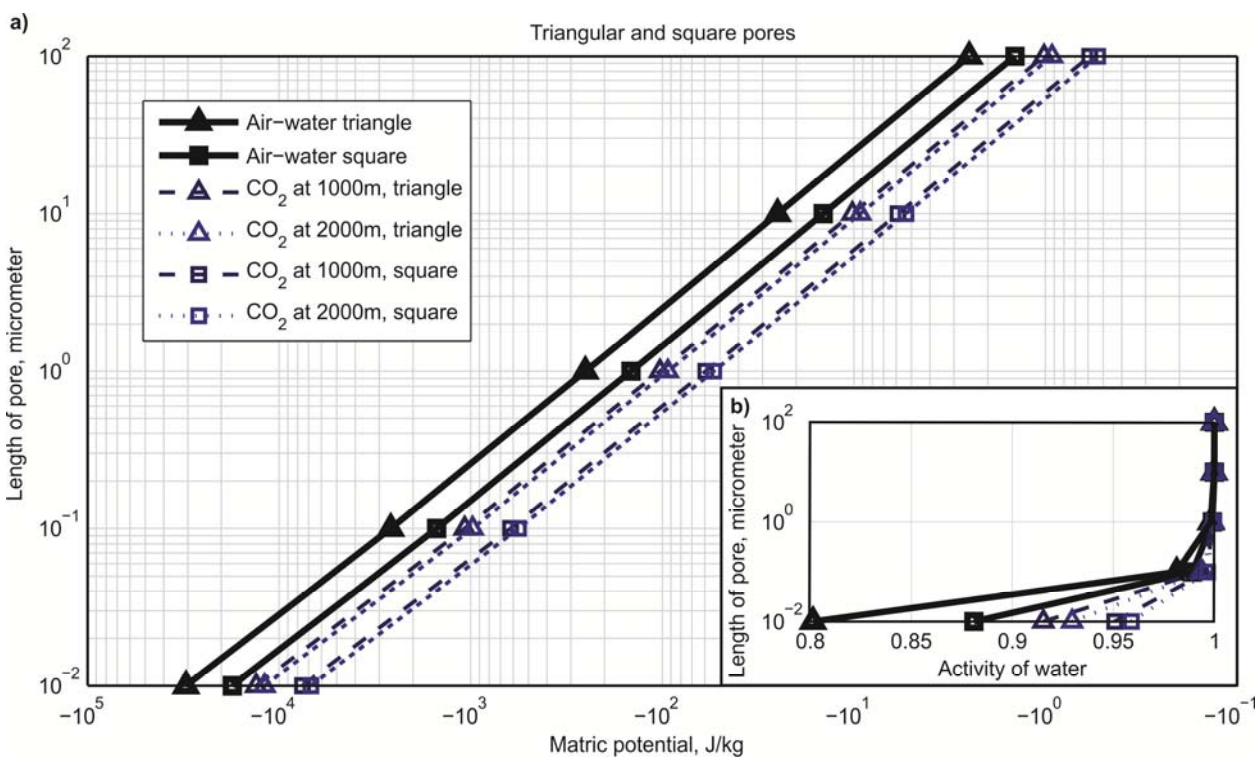

Figure 6. Imbibition snap-off as a function of a) chemical potential b) and activity of water for air-water and CO2-water systems, and for triangular or square pores

2.4 Conclusions

This study investigates capillary condensation and adsorption of water as a function of matric potential for the CO_2-water and air-water systems. At the same given chemical potential, water adsorption and capillary condensation will be less for the CO_2-water system as compared to that of the air-water system for geologic CO_2 storage and vadose zone conditions, respectively. Capillary water contributes much more greatly to pore saturation than adsorptive films,

especially at pores sizes equal to or greater than 1×10^{-6} m. Wedge-shaped pores with low angles of corners (e.g., < 60°) will contain significantly more capillary water than larger angle pores. If the matric potential or activity of water changes in the CO_2 phase (e.g., due to water vapor transport), our model indicates that wetting up to imbibition snap off (i.e., the spontaneous filling of pores) may occur if high enough water activities are achieved. Progressively higher matric potential or water activities are needed for larger pore sizes (see Figure 5). Matric potential thus has a strong control on water saturations, which will affect the capillary condensation in pores of different sizes: larger pores require orders of magnitude larger values of chemical potential than smaller pores for imbibition snap off.

3. MEASUREMENT OF ADSORBED WATER FILM DEVELOPMENT IN SUPERCRITICAL CO_2

3.1 Measuring water uptake with a quartz crystal microbalance

The quartz crystal microbalance (QCM) is method for way of measuring very small masses very accurately. The QCM itself consists of a thin quartz wafer with a gold electrode on each side. The electrodes are used to electrically stimulate the quartz, which is a piezoelectric material, causing it to vibrate in a transverse direction at a fixed frequency. The frequency of the quartz wafer is sensitive to tiny mass changes on the active area of the wafer; changes in frequency are directly proportional to mass changes on the wafer surface. The active region of the wafer is the area of overlap between the front and back gold electrodes. This approach is widely used to monitor deposited masses during vapor deposition procedures, and also to measure surface reactions, including adsorption/desorption, on the active face of the wafer. The active face of the wafer can be treated using a variety of techniques to control its reactivity with respect to different chemicals. In the experiments described here, the active surface consists of amorphous silica, which has been coated onto the gold electrode on one side of the QCM wafer. The QCM was used to monitor water adsorption onto the silica surface, in air and in $scCO_2$, as a function of the activity of water (a_w) in the gas phase—relative humidity (RH) in air, or P_w/P_{sat} in $scCO_2$. Then, films of montmorillonite clay, treated to be homionic with either Na^+, K^+, Ca^{+2}, or Mg^{+2}, were deposited on the wafer and water uptake by the clay was measured.

3.1.1 Methods

The QCM used for this work was a Maxtek© Research Quartz Crystal Microbalance, with a 9 MHz frequency controller. The quartz wafers were 1” diameter Inficon© 9 MHz wafers; the wafers were cut at an angle C-axis of the mineral that minimizes thermal sensitivity at 25ºC.

For the silica adsorption experiments, off-the-shelf Inficon© 9 MHz crystals were purchased with the gold electrode on the active face coated with silica. To make the clay-coated mounts, a smectite (montmorillonite) reference clay, SWy-2, was purchased from the Clay Mineral Society. The clay was disaggregated with an ultrasonic probe, and the <2 µm size fraction was separated by centrifugation. Portions of the clay were washed with solutions of NaCl (1 M), KCl (1 M), $CaCl_2$ (0.1 M), or $MgCl_2$ (0.1 M), to make the clay homionic, and then rinsed with deionized water and centrifuged until salt-free. Then, small volumes of each homionic slurry were vacuum filtered through a 0.20 µm filter and the clay was transferred to the surfaces of the QCM wafers using the Millopore filter transfer technique [54], to produce a thin, even layer. To minimize potential stresses to the wafer as the film dried, a mask was used to confine the clay film to the area of the front electrode. An example of the bare silica wafer and of a clay-coated wafer is shown in Figure 7.

In most QCM applications, the wafer is placed in a holder such that the back face of the crystal is not exposed to the aqueous or gas phase containing the reagent of interest. The holder also contains the electrode contacts for the wafer and a coaxial cable connects it to the QCM

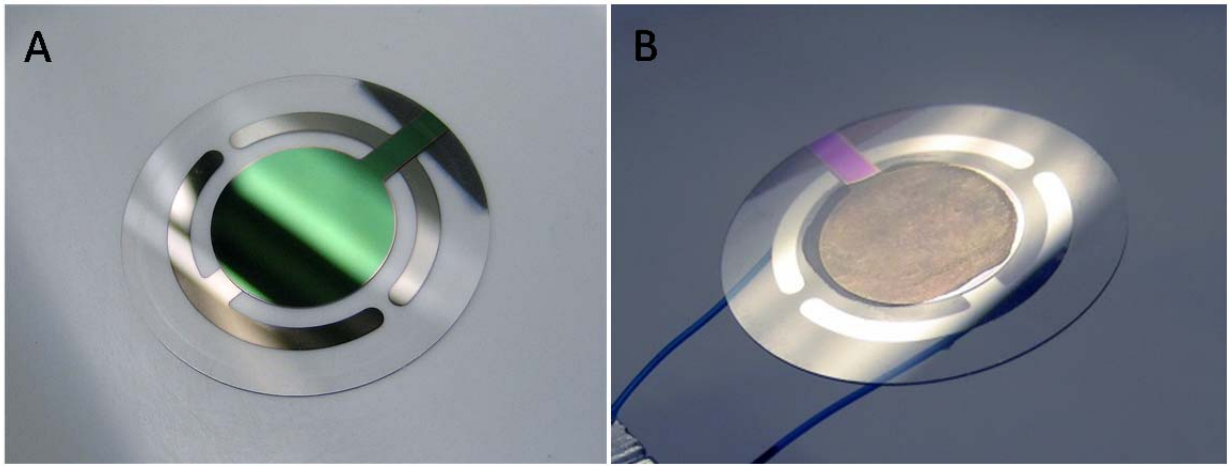

Figure 7. A) QCM wafer with a silica coating on the upper electrode. B) QCM wafer with a smectite clay film deposited on the crystal.

controller. However, the thin wafers can only withstand pressure differentials of a few psi between the front and back of the crystal. Therefore, for use at high pressures, the wafers were used without a holder. Instead, wire leads were soldered to the electrodes on the wafer, and the wafer was hung vertically, with both faces exposed to the surrounding atmosphere. To maintain consistency, the same setup was used for both ambient pressure and high pressure experiments. In order to prevent water adsorption onto the back of the crystal, which would complicate data interpretation, the gold electrode on the rear face of the wafer was treated with dodecanethoil make it hydrophobic. The dodecanethoil molecules self-assemble on the gold surface, with the reactive thiol groups bonding to the gold and the dodecane tails forming a hydrophobic layer over the surface of the electrode.

The experimental setup for experiments at low pressure is shown in Figure 8. The QCM wafer was placed in an exposure chamber within a temperature-controlled oven, and humidity within the chamber was controlled by mixing wet and humidified N_2 gas streams in different proportions using rotometer-type flow meters. A Viasala® temperature/RH probe was placed in the exposure chamber beside the QCM wafer to monitor conditions within the chamber.

The setup for measuring water adsorption in $scCO_2$ is shown in Figure 9. The QCM wafer was suspended in a high pressure chamber within a closed system. Pressure was maintained in the system, and $scCO_2$ was generated, by an ISCO model 500D syringe pump. Water was added to the system by use of a Rheodyne® injection valve with a 20 µL loop; a second chamber, upstream of the QCM chamber served as an equilibration chamber, prevented injected water from splashing onto the QCM prior to evaporation into the supercritical phase. A recirculating pump maintained flow throughout the system and sped equilibration. P_w/P_{sat} was used to estimate water activity. P_w was calculated from the added water content and the system volume, and P_{sat} was estimated using the TOUGH2 code and the CO_2 Equation of State (EOS) developed by Spycher and Pruess [55].

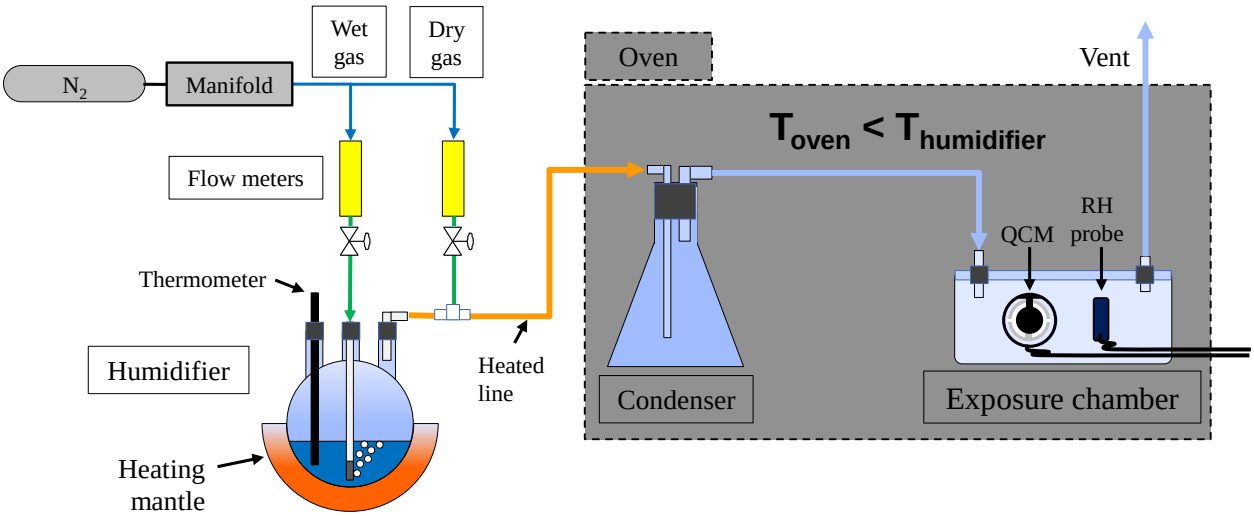

Figure 8. Experimental setup for measuring water adsorption in N_2 at ambient pressures.

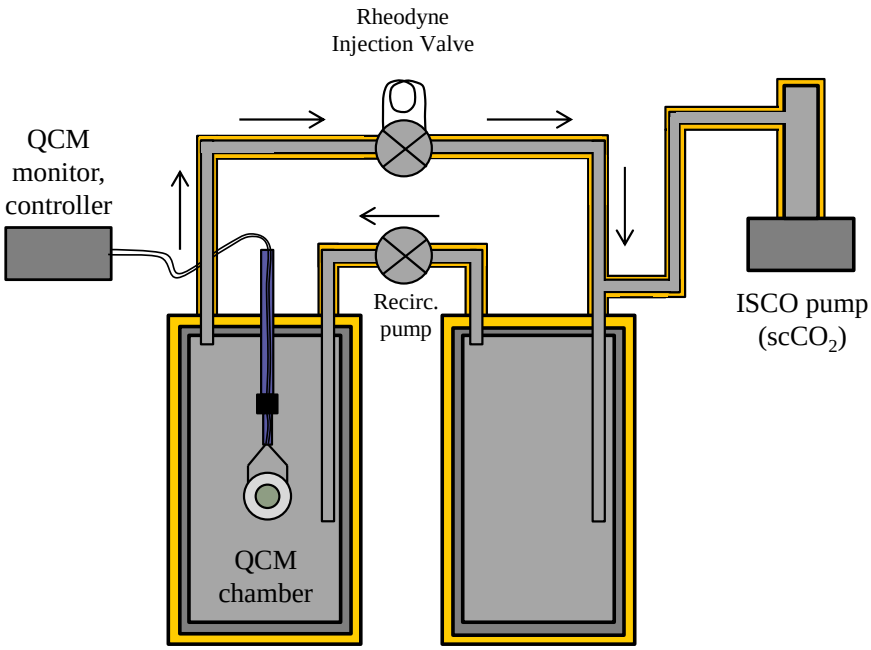

Figure 9. Experimental setup for measuring water adsorption in $scCO_2$.

3.1.2 Results and Discussion

3.1.2.1 Silica

Ambient pressure adsorption results for water adsorption onto the silica surface are shown in Figure 10, for both N_2 and CO_2 gases. Two different N_2 datasets are given for N_2, to illustrate the reproducibility of the data from run to run, and from wafer to wafer. CO_2 was assessed in addition to nitrogen, to see if development of acidity in the surface layer would affect water adsorption; very little change was observed relative to the nitrogen data. The general shape of the adsorption curve is typical for water adsorption to hydrophilic surfaces, with a steep increase in the mass of water adsorbed at low RH, leveling out as the RH rises. However, the total amount of water adsorbed is much greater than expected. A mass change of 1 $\mu g/cm^2$ is approximately equivalent to a water layer thickness of 10 nm, so the observed mass change of 5 $\mu g/cm^2$ corresponds to a water layer thickness of approximately 50 nm. This is much greater than observed water film thicknesses on quartz or other mineral surfaces. Figure 11 compares the masses of adsorbed water as determined by the QCM with that measured by standard vapor adsorption methods [56]. The adsorbed mass, as measured by QCM, is about 100 times that of the adsorbed mass measured by standard vapor adsorption methods [56]. As noted earlier, measurement of liquid films by QCM is difficult, because of viscous losses and slip at the fluid/crystal interface. However, these effects result in a measured mass that is lower than the actual sorbed mass. Because the observed mass change is much higher than expected in this case, these processes cannot explain the measured data.

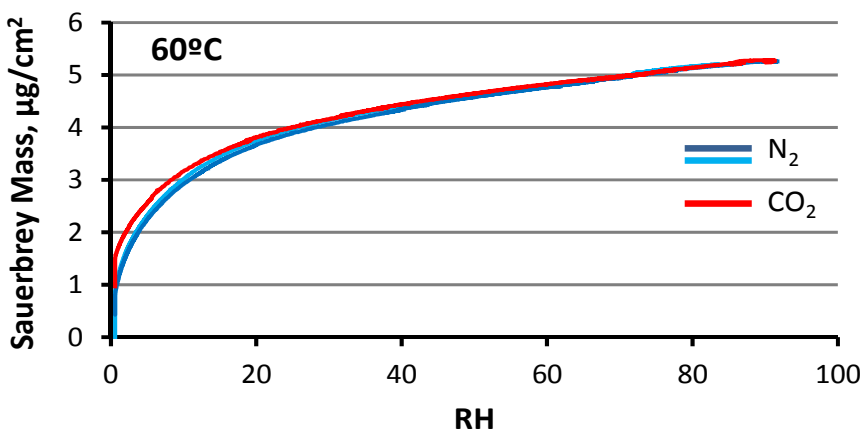

Figure 10. Water adsorption by the silica-coated Inficon QCM wafer.

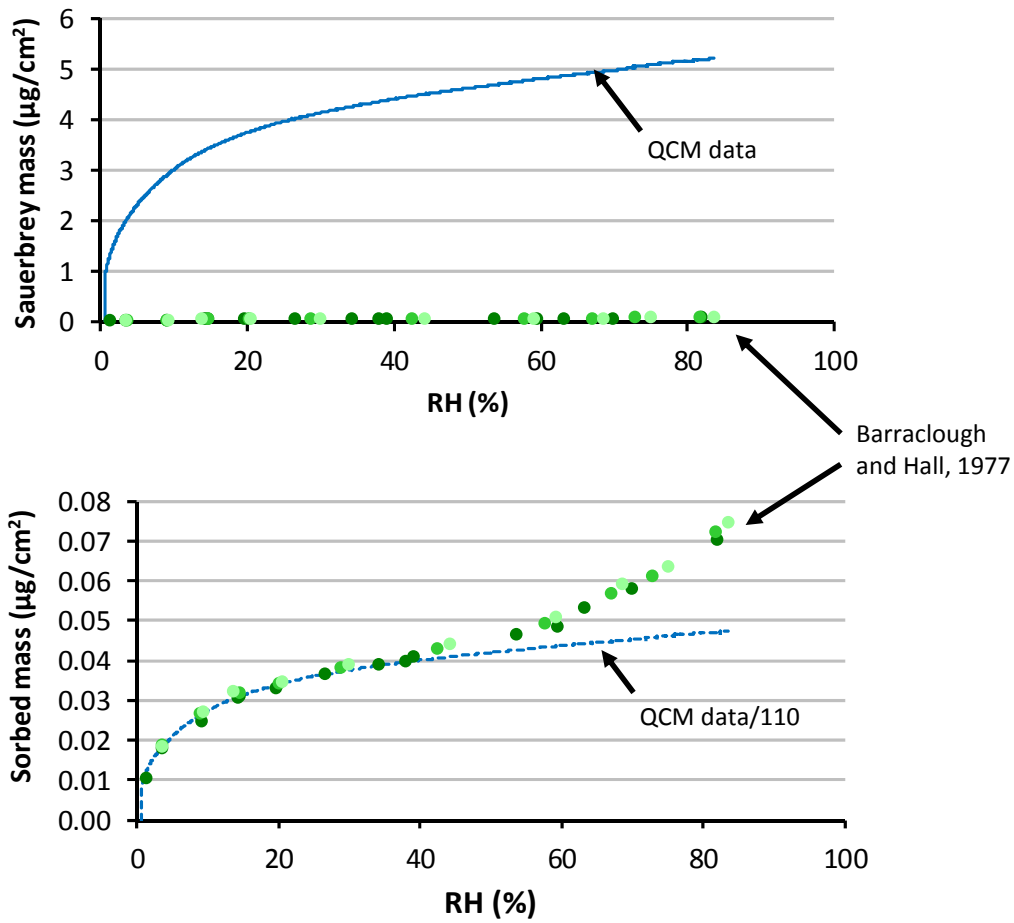

Figure 11. Water adsorption curves for the Inficon silica-coated QCM wafer, compared to experimentally measured water adsorption data.

An alternative possibility was that the surface of the QCM wafer was sufficiently rough to significantly increase the surface area relative to the nominal area of the active region. Moreover, surface roughness would promote coupling with the water layer, resulting in an apparent mass that is larger than the sorbed mass. To test this, the surface of the wafer was examined by Atomic Force Microscopy (AFM). However, the AFM analysis showed that the crystal surface roughness was only on the order of 14 nm (Figure 12). This results in a calculated surface area that is less than 10% higher than the nominal area. In addition, this degree of topography is insufficient to explain the observed water sorption through enhanced coupling with the water layer. Finally, the silica layer, which had been deposited by sputter coating, was examined by transmission electron microscopy (TEM) to evaluate whether it might be porous and be retaining water due to the greater than expected surface area, and due to capillary condensation in the pores. The silica layer was determined to be about 500 nm thick. Porosity was not observed directly within the silica layer, but the pores may have been nonperiodic and too small. However, the layer was significantly dimmer in the image relative to

the underlying quartz crystal. Material brightness a function of average Z, and the brightness of the layer relative to the underlying quartz wafer suggests it was significantly porous. It is likely that the excess sorption observed on the silica-coated QCM was due to adsorption and possibly capillary condensation into small pores within the sputter-deposited silica layer.

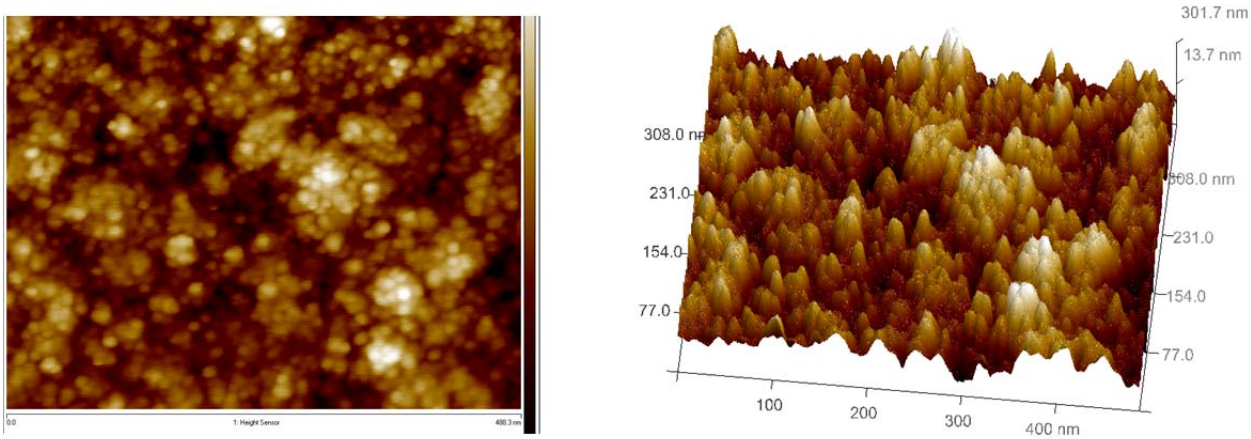

Figure 12. AFM image of the surface roughness of the silica layer on the Inficon wafers.

Because the adsorbed water is present not as a surface coating but as water in topography and in pores in the silica layer, it is strongly coupled to the surface of the QCM wafer, and is not subject to viscous losses or slip. Hence, the "Sauerbrey mass" reported by the QCM, which assumes good coupling between the film and the wafer, is likely to be an accurate measure of the actual sorbed mass on the QCM wafer.

Although the water sorption curves do not represent water film formation on a flat surface, they still represent a data point for comparisons to water sorption, measured with the same wafers, in $scCO_2$. Water adsorption onto the silica-coated wafers was measured in $scCO_2$ at a range temperature and pressure conditions that are relevant to CO_2 storage conditions, including 30ºC, 10 MPa; 40ºC, 14.5 MPa; and 60ºC, 8.3 MPa. The results are shown in Figure 13. Under all conditions, it is apparent that water sorption onto the silica-coated QCM wafers in $scCO_2$ is only a tiny fraction of the sorption that was measured in air or CO_2 at ambient pressures. Although much smaller than the adsorption measured at ambient pressures, the amount of adsorbed water is still significantly higher than that predicted by adsorption isotherms for water using BET methods (e.g, [56]). This is consistent with the model we have developed to assess water film thicknesses on mineral surfaces in $scCO_2$ (Section 2), which predicts that for a given P_w/P_{sat}, water films will be much thinner in $scCO_2$ than in air at ambient pressures, and the saturation of the porous silica layer will be much lower. One possible interpretation is that for the ambient pressure runs, nanopores in the silica layer are filling via snapoff; mass gain is proportional to pore volume. But in the $scCO_2$, the thinner water films mean that the pores are not filling—the mass gain s proportional to the pore surface area rather than the volume.

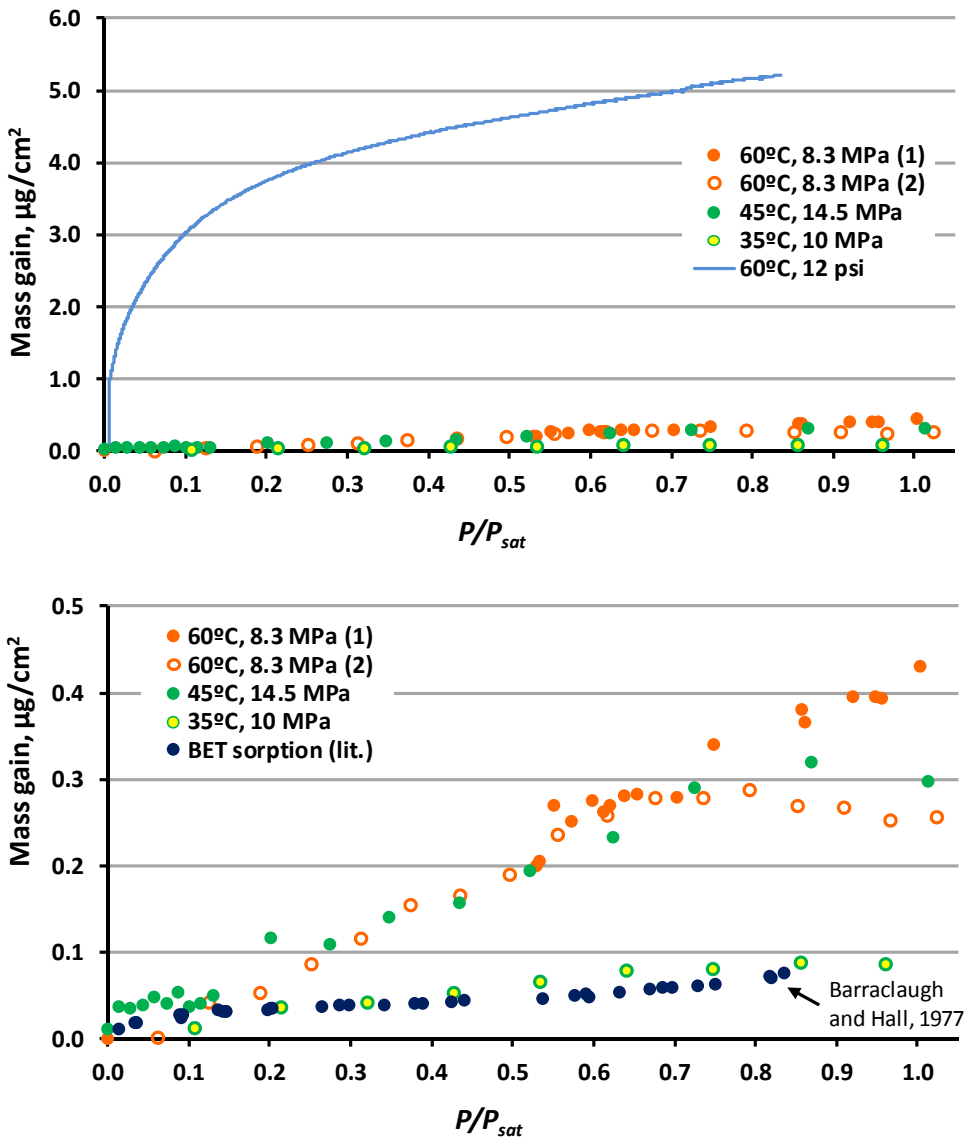

Figure 13. Water adsorption onto silica in $scCO_2$. Upper: Comparison with data from N_2. Lower: Comparison to published BET water vapor sorption isotherms.

3.1.2.2 Smectite clays

In air, water adsorption by swelling clays occurs by several mechanisms [57, 58] (Figure 14):

- Adsorption onto crystallite surfaces. This process is most important at low RH (or P_w/P_{sat}), but generally accounts for less than 20% of the water adsorbed.
- Interlamellar adsorption. Water adsorption in the interlamellar spaces occurs by hydration of the interlayer cations. This is the dominant mechanism of sorption over most of the range of P_w/P_{sat}. This mechanism has a larger impact for divalent montmorillonites than for monovalent montmorillonites.

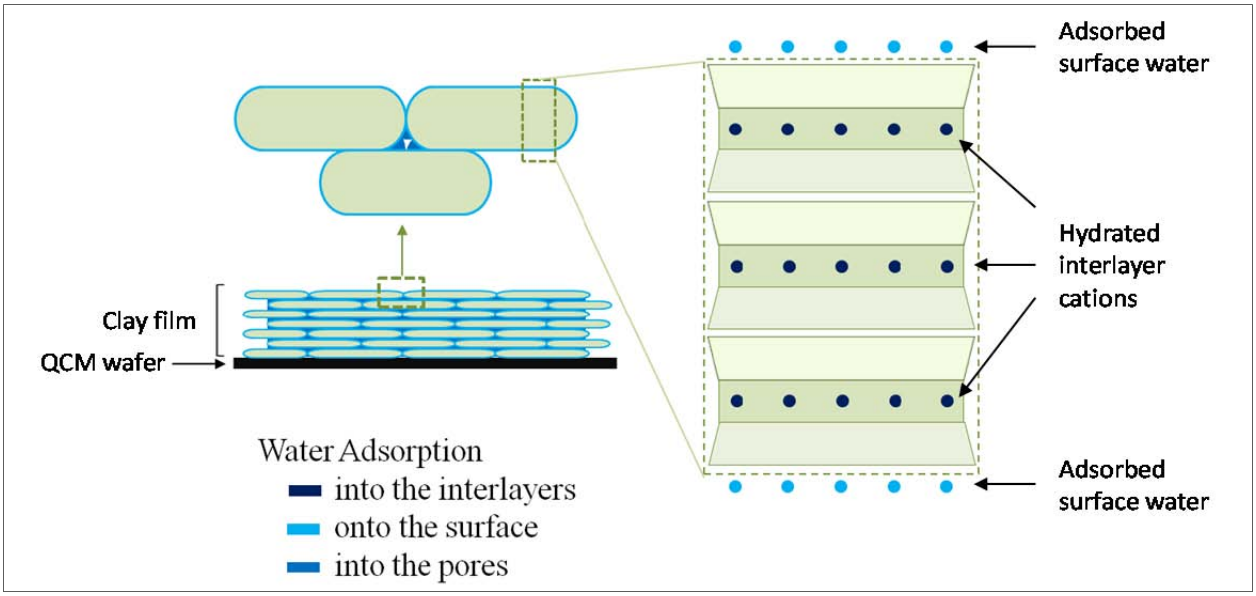

Figure 14. Water adsorption by clay films occurs by several different mechanisms including interlayer cation hydration, surface adsorption, and capillary condensation.

- Capillary condensation between clay crystallites. This process is most important at high water activities, and accounts for the commonly observed steep increase in water sorption once water activities in the gas phase exceed 0.85-0.9.

In $scCO_2$, water adsorption may be affected by additional processes. For instance, it has been suggested that CO_2 can enter the interlamellar sites and compete with water in cation hydration shells. This process, if it occurs, may inhibit water uptake by swelling clays in $scCO_2$ sequestration environments, having important impacts on the fate of stored $scCO_2$. For instance, infiltration of humid $scCO_2$ into a claystone caprock might result in clay shrinkage and the development of pathways for CO_2 leakage. Alternatively, shrinkage due to desiccation of shale during emplacement of anhydrous $scCO_2$ may or may not be recoverable once the $scCO_2$ absorbs water, or once water re-infiltrates into the rock as a bulk phase.

If CO_2 competes with interlamellar water, then mass sorption curves as a function of water activity in $scCO_2$ will differ from those in air, not only because less water may adsorb, but also because CO_2 could adsorb instead. Moreover, the adsorbed water film model in Section 2 suggests that capillary condensation would play a much smaller role in $scCO_2$ than in air, further reducing water adsorption.

Results for sorption of water by the four homionic smectites in N_2 at ambient pressures, are shown in Figure 15. The results are largely consistent with previous studies in the scientific literature. At any give aw, clays with divalent cations adsorb more water than monovalent clays, and water adsorption begins at lower a_w values. At water activities above 0.85 or so, a sharp

increase in water uptake occurs, as capillary condensation between the clay crystallites becomes a dominant process.

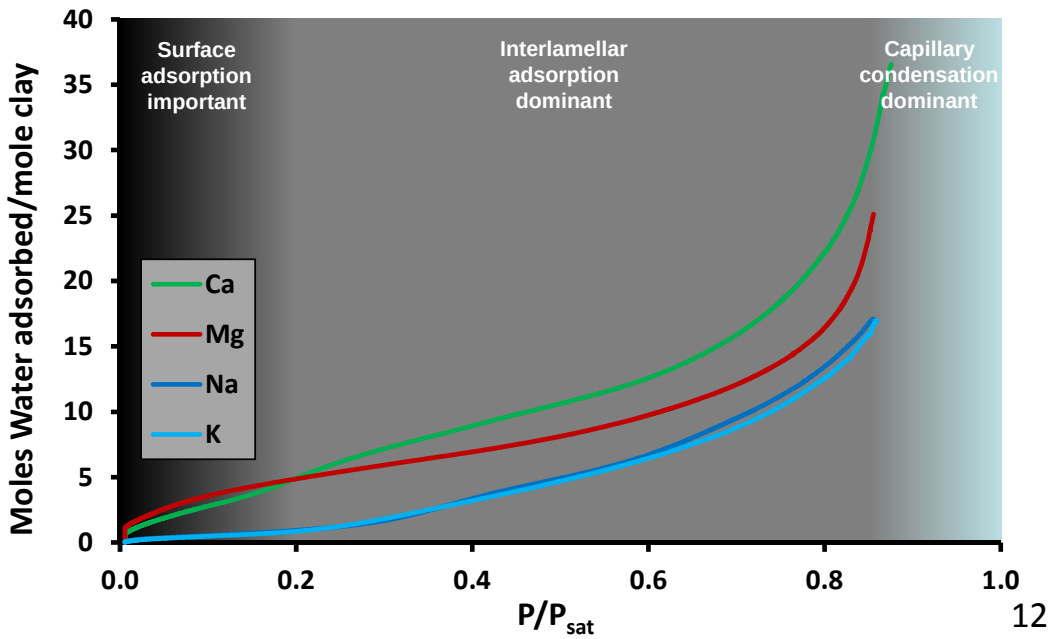

Figure 15. Smectite clay adsorption isotherms for water in N_2, at ambient pressure.

Initially, in this study, this was a concern that de-lamination of clay from the QCM wafer (e.g., air bubble formation under the clay film) would be a major source of experimental uncertainty. However, this was rarely observed in the ambient pressure systems, and the consistency of the results with adsorption isotherms determined by gas adsorption techniques such as BET suggests that QCM methodology is an appropriate and effective method for measuring water uptake by clays.

Isotherms for water adsorption by the Na-, K-, Ca-, and Mg-substituted montmorillonite clays in $scCO_2$ (60ºC, 10.3 MPa) are given in Figure 16. There is much more scatter than the ambient pressure data, and the isotherms are coarsely discretized, as the mass adsorbed was measured at discrete volumes of water injected, rather than continuously. Moreover, while clay delamination at ambient pressures was minimal, it occurred commonly in the $scCO_2$ systems. The data presented in Figure 16 represent the successful attempts out of many tries to measure water sorption isotherms in $scCO_2$ (success was evaluated by visual examination of the clay-coated wafer after use to ensure that delamination did not occur). Despite this, there are two clear trends. First, less water was adsorbed by the divalent cation clays than the monovalent clays, a reversal to the trends seen in the ambient pressure experiments. The reason for this is not clear. Second, at low a_w values, less water was adsorbed by the divalent clays in $scCO_2$, but not the monovalent clays; at middle-to-high a_w values, less water was adsorbed by all clays in $scCO_2$ than was adsorbed in the ambient pressure cases. Especially clear is the lack of an increase in adsorption at high P_w/P_{sat}, suggesting that capillary condensation is minimized in $scCO_2$. The second point strongly suggests that thinner water films and less capillary condensation is

occurring in the clay films in $scCO_2$. This conclusion is consistent with the water adsorption/capillary condensation model presented in Section 2.

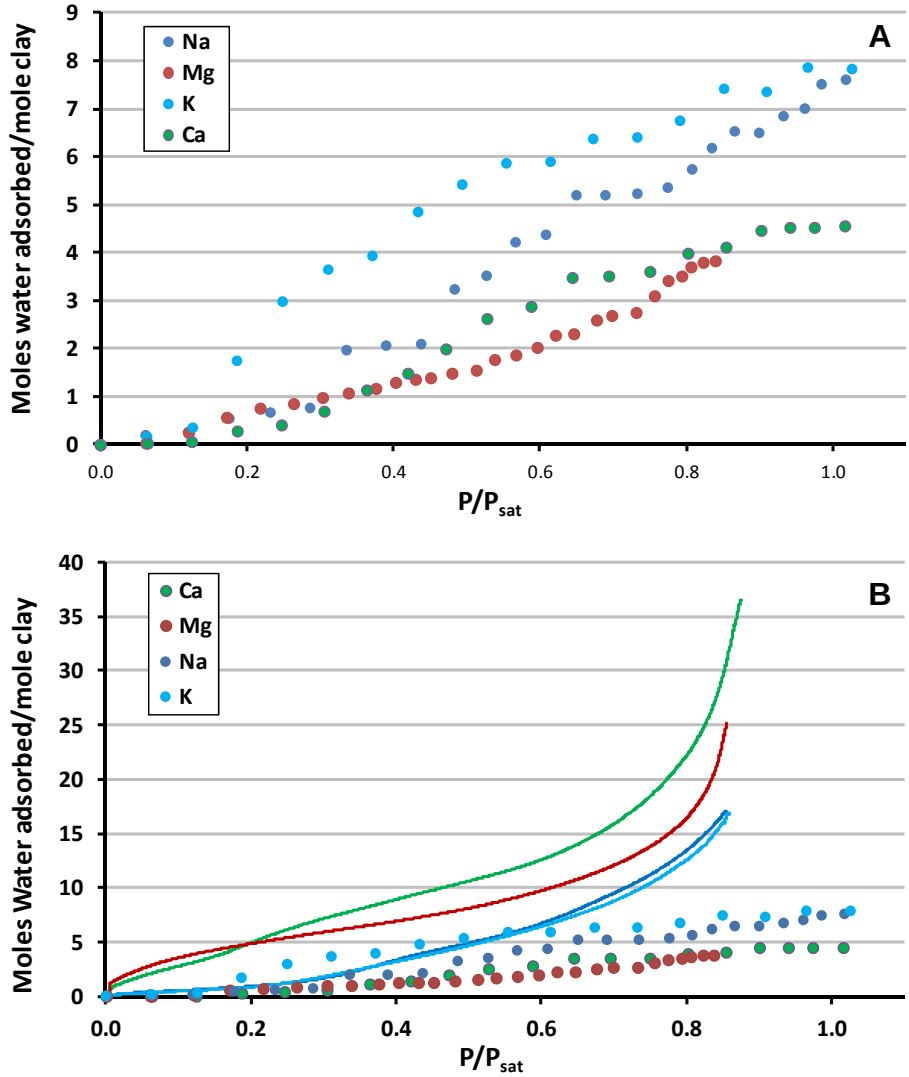

Figure 16. Water adsorption isotherms for homionic (Na, K, Mg, and Ca) montmorillonite films. A) Adsorption isotherms in $scCO_2$; B) Comparison of isotherms in $scCO_2$ with those collected at ambient pressures.

3.1.3 Conclusions

In this study, a QCM was used to successfully measure water adsorption onto a silica surface at both ambient pressures and high pressures. The porous nature of the silica layer used prevented accurate measurement of water film thicknesses, but was advantageous in that it resulted in strong coupling of adsorbed (or trapped) water with the QCM wafer, eliminating the need for accounting for viscous losses or slip in evaluating the sorbed masses. QCMs have been used to measure water sorption previously, [59-63], and QCMs have been used, rarely, in $scCO_2$ [64-66];

however, this is the first attempt to use the technology for measuring water adsorption isotherms in $scCO_2$.

The QCM was also successfully used for measuring water adsorption by clay at ambient pressures and at elevated pressures. This has not previously been done, and the method provides a tool for assessing clay swelling under a range of conditions that had not previously been accessible. Clay water uptake is significantly less in $scCO_2$, than in air, and this appears to be dominantly a function of less capillary condensation between the clay particles. This is consistent with the water adsorption/capillary condensation model described in Section 2.

These findings are significant with respect to CO_2 sequestration, as they indicate that capillary condensation is not likely to be an effective rewetting mechanism following reservoir host rock dryout by injected $scCO_2$. The data also suggest that changes in clay caprock permeability will occur due to clay shrinkage when $scCO_2$ infiltrates, even if it is wet $scCO_2$. Moreover, clay shrinkage in response to dry $scCO_2$ infiltration will not be recovered by eventual humidification of the CO_2; rather it will depend on re-infiltration of the aqueous phase.

3.2 Measuring water uptake by Fourier Transform Infrared Spectroscopy

3.2.1 Introduction

In this section we summarize our new experimental approach at assessing water sorption from humid supercritical carbon dioxide using a technique called Fourier Transform Infrared Spectrophotometry (FTIR). FTIR is a spectroscopic technique that looks at adsorptive spectra across a range of frequencies [67]. Its application is ideal for this application as different forms of H_2O (e.g. adsorbed H_2O on mineral surfaces, capillary H_2O in nanopores, free H_2O solved in $scCO_2$) will adsorb different frequencies of light, thereby permitting diagnostics as to the state of H_2O in a mineral-H_2O-CO_2 system. For subsurface geologic carbon storage applications, FTIR has principally been used to measure amounts of carbonation of minerals [10, 68] and calcium-aluminum cements [69].

Absorption spectra interpreted in this document were obtained using the technique known as Attenuated Total Reflectance (ATR), in which an infrared (IR) beam is propagated inside an infrared transparent element designed to cause multiple reflections as the beam travels down the element. Since the beam is propagated at greater than its critical angle with the interface between the ATR element and its external environment, the IR wave, in the absence of absorbing species in intimate contact with this interface, is completely reflected each time it impinges on the surface of the ATR element. However, although the propagating IR wave remains completely inside the ATR element, its electromagnetic field crosses the interface and can interact (be absorbed) by materials in contact with the ATR element. This penetration of the electromagnetic field into the medium in contact with the ATR element has been called the “evanescent wave.” The depth of penetration of the evanescent wave into the second medium can be calculated from the refractive indices of the ATR element and the medium in contact and the angle of incidence of the IR beam, but a useful approximation is that it is on the order of a fraction of the wavelength of the IR beam.

It is important, in interpreting the IR spectra, to realize that they are the ratio of two "single beam" spectra: one taken under the conditions described for the spectra; and the other "background" spectrum usually taken under conditions considered baseline for the experiment. Ratioing these spectra eliminates features related to the wavelength-dependent response of the IR spectrometer, its detector, the ATR accessory's optics, the ATR element itself and absorption or scattering events in the path of the IR beam but outside of the volume of the experiment of interest. Thus, the features seen in the IR spectra referred to in this document represent *changes* in the environment with which the IR beam interacts compared to that present when the background spectrum was obtained. Positive-pointing features in the ratioed spectra thus correspond to increased absorption by a species. Negative-pointing features correspond to decreased absorption by a species.

For the series of experiments carried out as part of this study, we employed a unique high pressure FTIR cell manufactured by PIKE Technologies, termed the "JetStream ATR Accessory" which was designed and built at our request for this study. It operates at a Maximum Allowable Working Pressure of 2000 pounds per square inch (psi). This device is shown schematically in Figure 17. In this system, an IR beam is directed at one end of the cell into a ZnSe crystal of higher refractive index than the surrounding medium, which in our case is supercritical CO_2 with or without water. The IR beam reflects from the internal surface of the crystal and creates an evanescent wave, which projects orthogonally into the $scCO_2$ in contact with the crystal. Some energy of the wave is absorbed by the sample and the reflected radiation is both partially absorbed by the $scCO_2$ and returned to the detector. The depth of penetration yields a relative measure of intensity of the resulting spectrum measured with the FTIR spectrophotometer.

In some cases, the background spectrum used in the ratioing was obtained with CO_2 at high pressure in the ATR cell in order to minimize CO_2 features, which would tend to dominate, in the ratioed spectrum. Also, features due to the EPDM o-rings sealing the ATR element to the cell are minimized by ratioing, but can be present when cell pressure changes and the o-rings flex, changing the amount of their surface in contact with the ATR element (that is sampled by the evanescent wave of the IR beam).

3.2.2 Materials and Methods

For (FTIR) analysis, we used a PIKE Jetstream high pressure attenuated total reflection (ATR) cell, with a ZnSe cylindrical crystal (Figure 17). The ATR accessory was used with a Nicolet Nexus 870 FTIR Spectrometer. For controlled the environments of water adsorption, the equipment used was largely the same at that used for QCM experiments in Section 3.1. The controlled environment at low pressures was that shown in Figure 8, except that heated lines were used instead of an oven to control temperatures in the gas transfer lines, and the Vaisala® RH/temperature probe was in a separate chamber upstream of the ATR-FTIR cell. Both the transfer lines and the RH/temperature probe chamber were kept a few degrees Celsius hotter than the ATR-FTIR cell to prevent condensation. The system for measurements in $scCO_2$ was identical to that shown in Figure 9, except that the QCM chamber was replaced with the Jetstream© FTIR-ATR cell. All experiments were run at 40ºC, and the $scCO_2$ experiments, at 1400 psi.

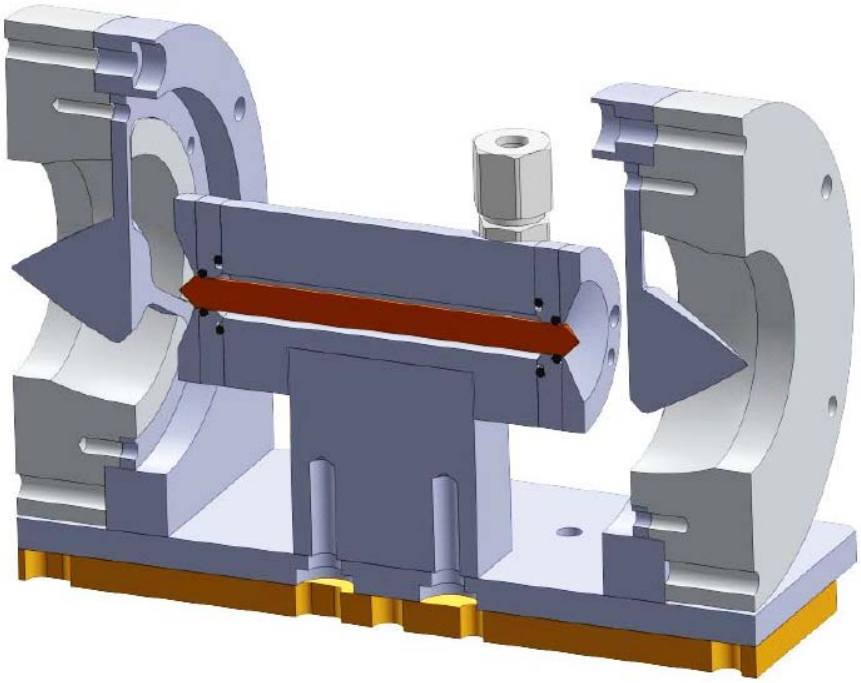

Figure 17. PIKE Technologies "JetStream" ATR High Pressure FTIR Cell designed and built for this study.

In the experiments, the ZnSe ATR crystal was first run as-delivered, to establish a blank. ZnSe is relatively hydrophobic. Then, the crystal was plasma coated with a 71Å coating of amorphous silica; plasma coating was used because it generally deposits a relatively dense, nonporous layer of material. Following experiments with the silica-coated crystal, it was drip-coated with Ca-montmorillonite by using an-eyedropper to apply droplets of a clay slurry to the surface of the crystal and allowing to dry. This method was used instead of drip coating because the slurry tended to run off of the crystal when dip-coating, leaving little or no residue.

3.2.3 Results

First, we summarize results of supercritical CO_2 spectra contacting the ZnSe crystal itself, both dry and containing an amount of H_2O. We then examine absorption spectra in the presence of silica surfaces and nanopores by coating the crystal with silica. We then end our discussion by examining $scCO_2$-H_2O interactions with a coating of clay minerals.

3.2.3.1 Bare ZnSe ATR Element

In Figure 18 are spectra of $scCO_2$ on the bare ZnSe element as its pressure is increased to and past the supercritical point. The background for these spectra was obtained with a nitrogen-flushed ATR cell prior to introducing CO_2. At low pressures the CO_2 spectrum consists of bands due to the fundamental stretching and bending vibrations (near 2350 cm^{-1} and 670 cm^{-1},

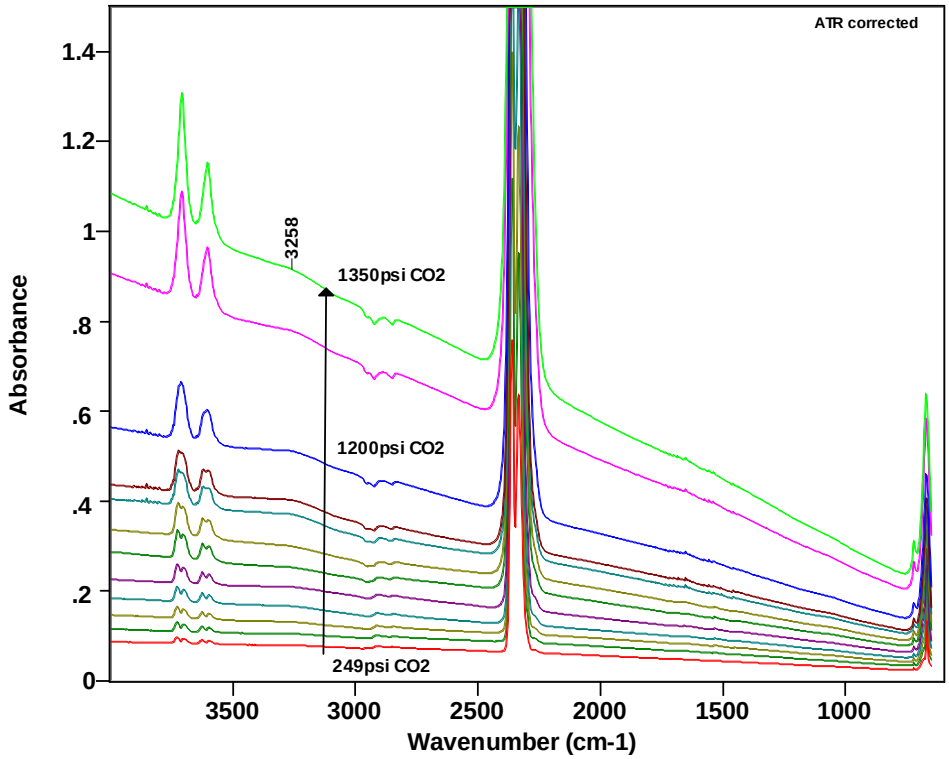

Figure 18. Absorption spectra of CO_2 contacting the ZnSe crystal as pressure increases past the critical point (~1100 psi at 35ºC).

respectively) and the Fermi Resonance bands (near 3610 cm^{-1} and 3710 cm^{-1}). The Fermi Resonance bands are actually combination bands (of the fundamental IR-active stretching mode seen in the spectra and a Raman- but not IR-active mode peaking near 1250 cm^{-1}). Two combination bands are seen because of what is known as Fermi Resonance splitting of two bands that would otherwise occur at the same energy, contrary to quantum mechanical rules. The fundamental stretching mode and the Fermi Resonance bands show additional splitting because, in the gas phase, they are composed of rotational transitions, which are known as "Q" and "R" branches, in addition to the vibrational transitions. As the pressure increases the bands broaden, and the rotational/vibrational splitting becomes less apparent. When the CO_2 assumes a condensed phase (above the supercritical point), the rotational motions are damped out, and the bands collapse into a single profile centered on the vibrational transition. In addition to a general increase in absorption intensity with increasing pressure, small, progressive frequency shifts in the band centers occur.

In Figure 19, we show spectra obtained with CO_2 1400 psi with the bare ZnSe element. The backgrounds for these spectra were taken at that CO_2 pressure. The experimental variation for the set of spectra consisted of progressively adding water to the pressure cell as noted on the spectra. The water bands (stretching, 3000-3600 cm^{-1}, and bending, near 1650 cm^{-1}) resulting from these additions have the shape of liquid water but are shifted a few tens of inverse centimeters lower in frequency, possibly as a result of the high cell pressure. Note that features from CO_2 (stretching mode near 2350 cm^{-1} in Slides 2-4 and combination bands, 3600-3700 cm^{-}

[1], and bending modes, 670 cm^{-1}, in Figure 19), both positive- and negative –pointing, appear in the spectra and increase in intensity as the water content is increased. The presence of these bands suggests that interaction with water is causing some changes in the intensity and position of the CO_2 bands. Negative-pointing bands at 2800-3000 cm^{-1} and 1500-1600 cm^{-1} are related to changes in the overall absorption of the EPDM or-rings.

The background for the spectra in Figure 20 was taken with the bare ZnSe element at ambient pressure in flowing nitrogen. 600 µL of water was added to the cell, causing the appearance of the stretching and bending modes of liquid water. Then, addition of CO_2 to the cell to 1400 psi resulted in the appearance of CO_2 bands across the spectrum and the decrease in intensity of the water bands to low levels, which were not significantly increased by the addition of more water to a total of 1100 µL. It appears that water on the surface of the ATR element was largely replaced by CO_2 under pressure.

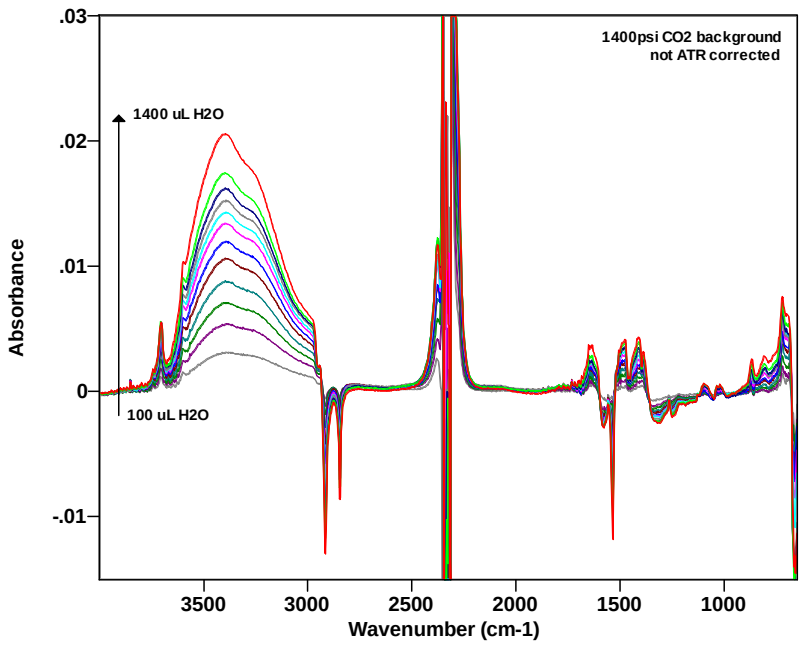

Figure 19. Spectra obtained with CO_2 at 1400 psi.

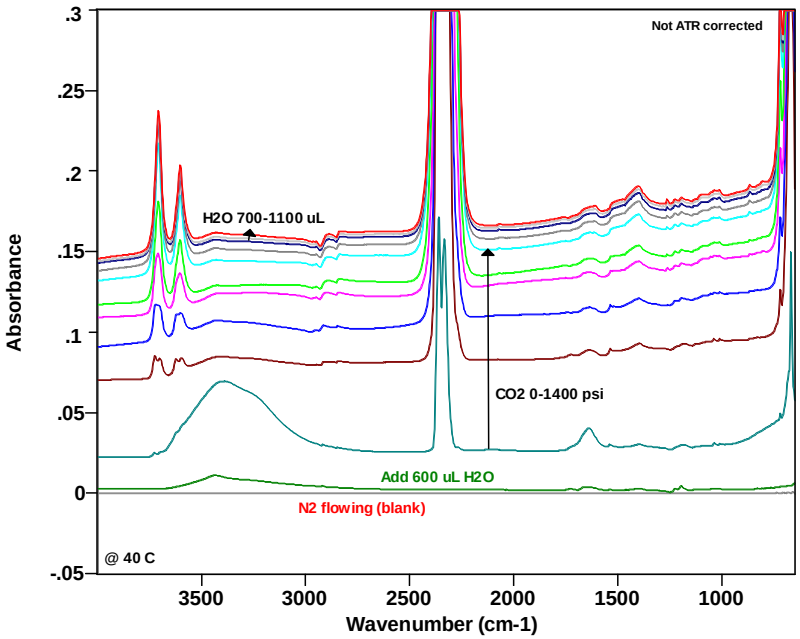

Figure 20. Spectra obtained at 1400 psi with 700 to 1100 µL added H_2O.

The opposite experiment was carried out as shown in the spectra in Figure 21. The background for these spectra was obtained with 1400 psi present in the ATR cell. Subsequently a total of 1100 µL of water was added in increments with the result of only low intensity water bands. However, following a decrease CO_2 pressure to 1000 psi, the water bands significantly increased in intensity. Further decreases in CO_2 pressure resulted, as expected, in negative-pointing CO_2 bands. Note that the EPM o-ring bands first appeared as negative-pointing bands, then ultimately reversed direction as the CO_2 pressure decreased to ambient.

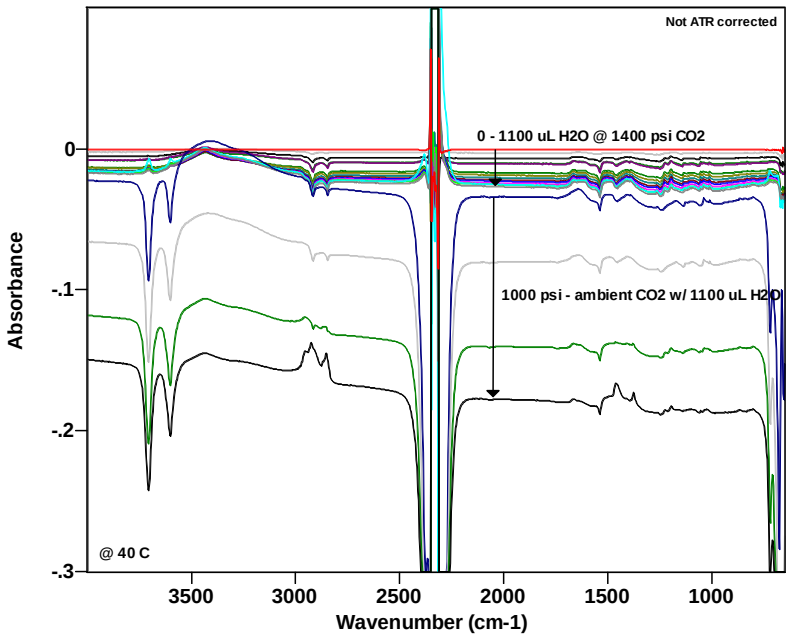

Figure 21. Spectra obtained at 1400 psi with added H_2O.

3.2.3.2 ZnSe Element with Silica Coating

For the next set of experiments, the ATR element was coated with a sub-micron film of silica (nominally SiO_2). Figure 22 shows a spectrum at ambient pressure with nitrogen flowing, using a background of the uncoated ATR element. This spectrum shows, in addition to o-ring bands, bands at 1000-1200 cm^{-1} consistent with amorphous silica, a band near 900 cm^{-1} suggesting the presence of a silanol species, liquid water bands (3000-3600 cm^{-1}) and a negative-pointing isolated O-H band (near 3700 cm^{-1}) from an "isolated" hydroxyl that was apparently on the bare ZnSe but was removed when it was coated with silica. The other spectrum in Figure 22 shows the spectrum of the silica-coated ATR element in 1400 psi CO_2 plus 1200 uL water with a background of the same environment prior to the water addition. This spectrum shows shifted water bands (more on this later) and a negative-pointing silanol band. The decrease in absorption of the silanol band represents the incorporation of the silanol hydroxyl into a more hydrogen-bonded matrix of water molecules.

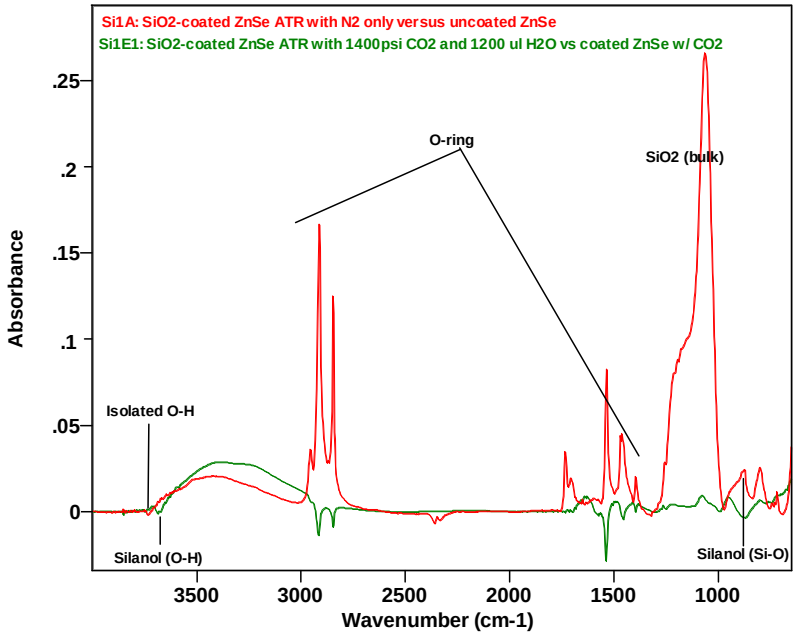

Figure 22. Spectra with ZnSe coated with silica.

The spectra in Figure 23 show the effects of progressively adding water to a total of 1200 uL. The bands due to various species are labeled in the slide. The background for Figure 23 is the silica-coated ATR element at 1400 psi CO_2. The CO_2 stretching band features were removed from the spectra to simplify interpretation. The water stretching bands initially appear with a broad, featureless peak near 3270 cm^{-1}, but eventually shift into features much like those from liquid water as the water content is increased. A broad, featureless peak like that seen near 3270 cm^{-1} has been associated with "ice-like" water by Asay and Kim [6] but the peak position and lack of structure in the band suggests that it is more like the amorphous solid water identified by Bergren et al. [70] at low temperatures. It may be that the internal pore structure of the silica initially constrains the water molecules into the "amorphous solid" conformation. Negative-pointing bands at 3688 cm^{-1} and 870 cm^{-1} are believed to indicate the conversion of vicinal silanol (hydroxyls on adjacent silicon atoms) IR bands to those of liquid water as the silanols are incorporated into a more hydrogen-bonded water matrix as the water content increases. The complex structure of positive- and negative-pointing features in the 1000-1200 cm^{-1} region is believed to reflect the attachment of hydroxyl molecules to silica tetrahedral, converting some bridging (Si-O-Si) bonds to silanols.

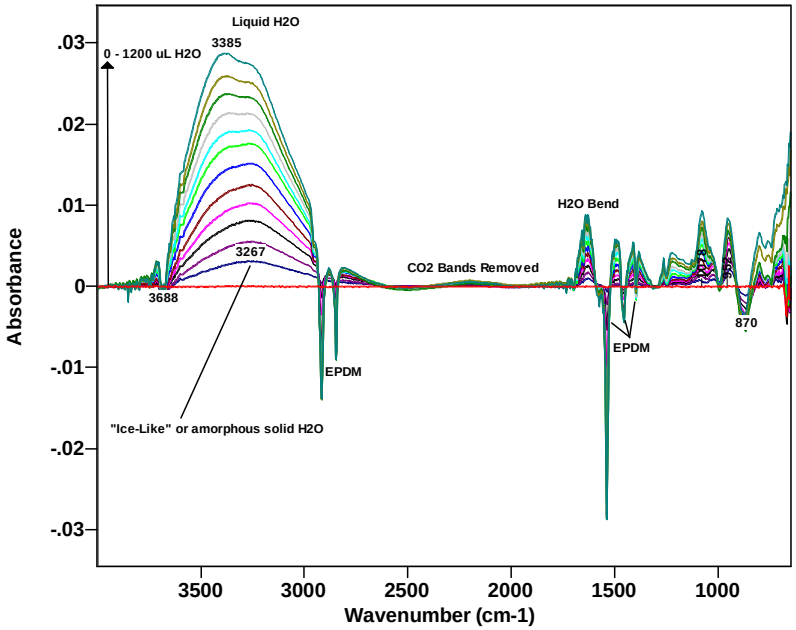

Figure 23. Spectra from silica coated ZnSe element with progressively increasing amounts of H_2O added to the $scCO_2$ environment.

Figure 24, and Figure 25 depict spectra from an experiment in which the silica-coated ATR element was subjected to increasing relative humidity (to about 82%) at ambient pressure in nitrogen. Figure 24 includes a spectrum using the uncoated ATR element in ambient nitrogen as the background, in order to include, for comparison, the features due to the silica coating. The remaining spectra have the silica-coated ATR element in flowing nitrogen as their background. Figure 25 shows the spectra of Figure 24 with baseline-corrected spectra and the region with O-H stretching bands. The development of the water (O-H) stretching mode is about the same as with the water additions in high CO_2 pressure: a band corresponding to amorphous solid water morphing into a profile like that of liquid water as the relative humidity increases.

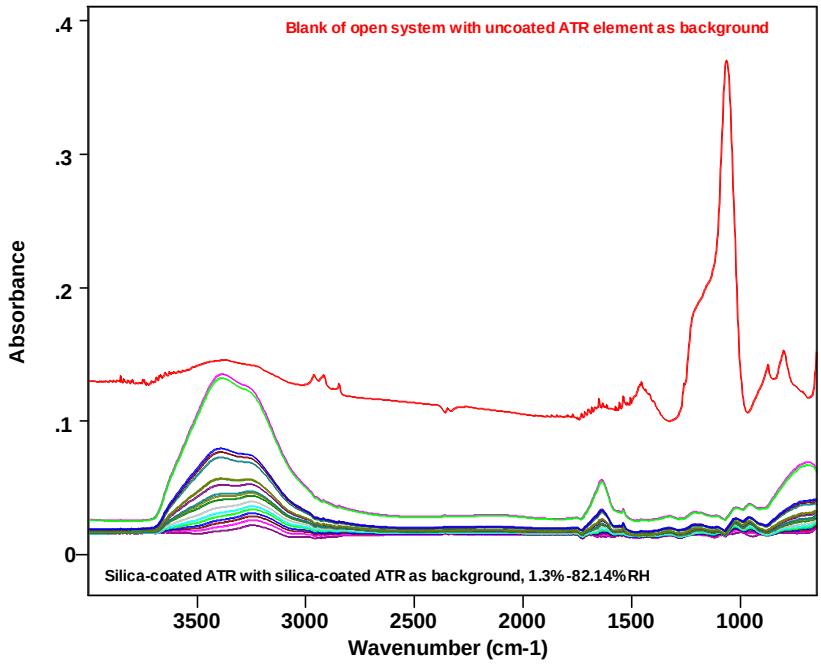

Figure 24. Spectra from silica coated ZnSe element with increasing RH in N_2.

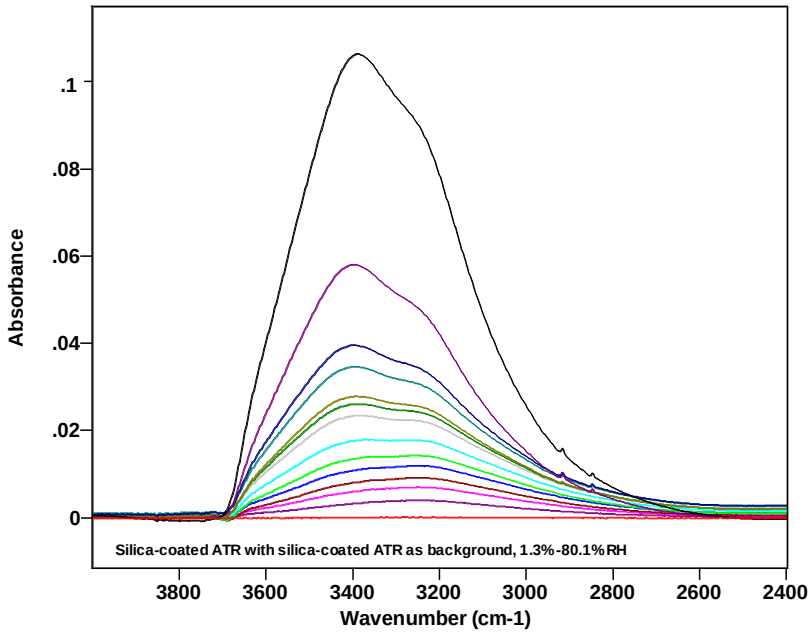

Figure 25. Spectra from silica coated ZnSe element with increasing RH in N_2 (expanded frequency scale in the water stretch mode region).

3.2.3.3 Silica-covered ZnSe element with clay coating

Figure 26 shows spectra from an experiment conducted after coating the silica-coated ZnSe ATR element with a thin layer of clay nominally from the family of clays that includes the aluminosilicate, Montmorillonite. The spectra were obtained at ambient pressure with the relative humidity progressively increased to 72%. One of the spectra (the red trace), as indicated in the slide, used, as a background, the ZnSe element with only its silica coating. This spectrum shows features due to the clay coating prior to water exposure (flowing nitrogen). The prominent features in this spectrum are water stretch (near 3630 cm^{-1}) and bend (near 1620 cm^{-1}) modes. The relatively high frequency and narrow width of the stretch mode indicates that the water molecules associated with this feature are in ordered, crystalline lattice positions. Such water molecules are often called "waters of hydration" in the chemistry community, but they will be referred to as "crystalline" water in this document. The negative-pointing bands in this spectrum are due to the EPDM o-ring. Since the lower frequency limit of the spectrum is near 1100 cm^{-1}, only the high frequency edge of the clay lattice bands is present in the spectrum.

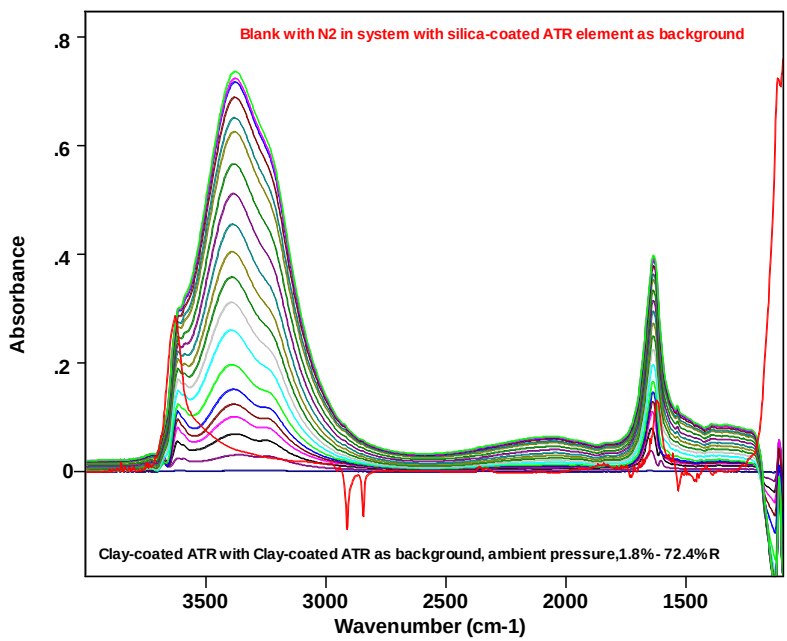

Figure 26. FTIR spectra with clay coatings, using silica coated example as background.

The remaining spectra in Figure 26 use the clay-coated ZnSe element in nitrogen, prior to increasing the relative humidity, as the background. These spectra reflect the changes in the clay and its surface as water is added to the ATR chamber. The features that increase regularly with relative humidity increases and come to dominate the spectra are water stretch (3380 cm^{-1} and 3220 cm^{-1}) and bend modes (1640 cm^{-1}). The shape of the stretch bands resembles that of liquid water, just shifted a few tens of inverse centimeters to lower frequency, possibly due to near surface adsorption effects. At the frequencies of the crystalline water stretch and bend modes, negative-pointing features appear as the relative humidity increases, with a positive-pointing

peak developing at slightly lower frequency (near 3620 cm^{-1}) from the crystalline water stretch mode. These changes in the crystalline water bands are due to changes in the crystal lattice around the crystalline water and/or increased hydrogen bonding interactions of the crystalline water with water molecules adsorbing on or infiltrating the clay lattice.

Figure 27, Figure 28, and Figure 29 show spectra using the clay-coated ZnSe ATR element under 1400 psi CO_2 as up to 1200 uL water is progressively added to the chamber. Figure 28 and Figure 29 show expanded-frequency-scale versions of Figure 27 for the water stretch and bend mode regions. One spectrum (the red trace) on these figures uses the silica-coated (only) ZnSe element in 1400 psi CO_2 as the background in order to show the IR features due to the clay (at 1400 psi CO_2) prior to water addition. The aluminosilicate lattice bands of the clay provide the broad, complex band structure between 700 cm^{-1} and 1100 cm^{-1}. IR bands due to Montmorillonite are less broad and complex, but they fit within the envelope of the clay lattice bands in Figure 27. Crystalline water bands are also present in this spectrum, peaking near 3630 cm^{-1} (stretch mode) and 1620 cm^{-1}, as in the corresponding spectrum in Slide 16. However, the crystalline water stretch mode in Figure 27 (and Figure 28) shows shoulders near 3700 cm^{-1}, 3580 cm^{-1} and 3500 cm^{-1} on the corresponding feature in Figure 26. It appears that the high pressure environment has created additional or more distinct lattice sites for crystalline water to reside. Carbonate formation would be indicated by an intense, broad band peaking in the 1450 cm^{-1} region; no such band is observed.

The remaining spectra in Figure 27, Figure 28, and Figure 29 use the clay-coated ZnSe element at 1400 psi CO_2 prior to water addition as the background. They show the changes occurring as up to 1200 uL of water is added to the chamber. There is a complex set of changes occurring in the clay lattice with water addition, as shown by the complex of positive- and negative-pointing features in the 700 cm^{-1} to 1200 cm^{-1} region. A detailed analysis of these features would require more time than is available now. Bands like those of liquid water (but slightly shifted in frequency) develop and dominate the water stretch mode (3000 cm^{-1} – 3500 cm^{-1}) and bend mode (1640 cm^{-1}) regions. Negative-pointing bands due to crystalline water develop on the shoulders of the liquid water bands. In fact, four negative-pointing bands, corresponding to the dominant crystalline water stretch mode and the three shoulders, are apparent in the spectra. It is believed that the crystalline water modes disappear because these water molecules become hydrogen bonded (and thus look like liquid water) to the infiltrating water from the water additions. As noted in earlier experiments, the carbon dioxide bands shift and broaden with water addition.

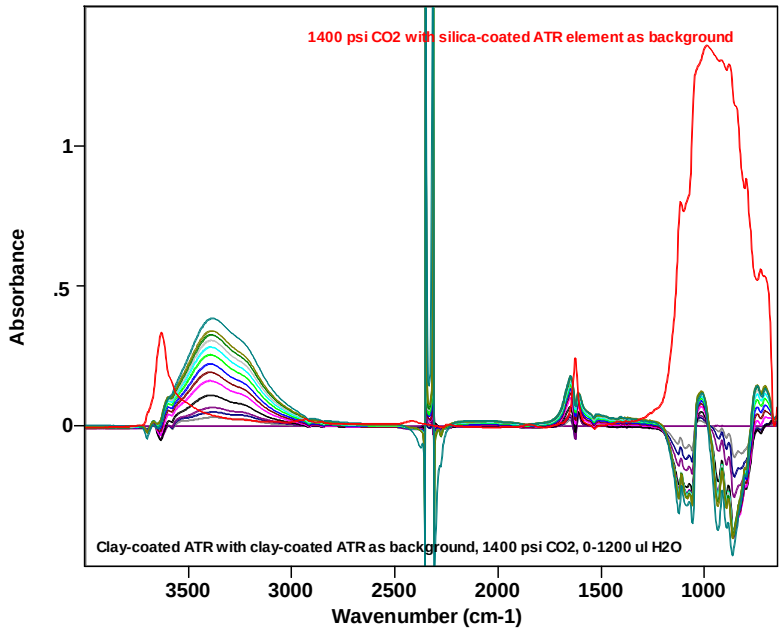

Figure 27. FTIR spectra with clay coatings in $scCO_2$ with increasing H_2O.

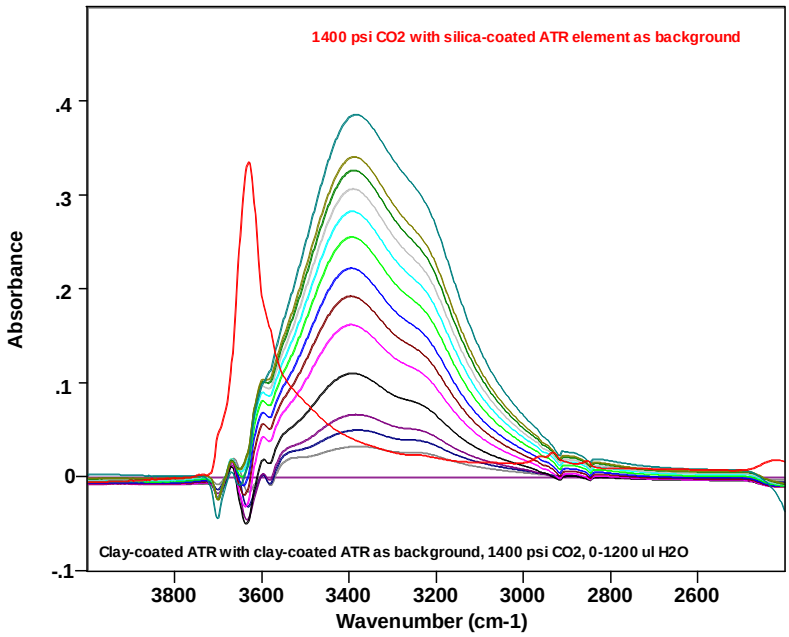

Figure 28. FTIR spectra with clay coatings in $scCO_2$ with increasing H_2O (expanded-frequency-scale of water stretch mode region).

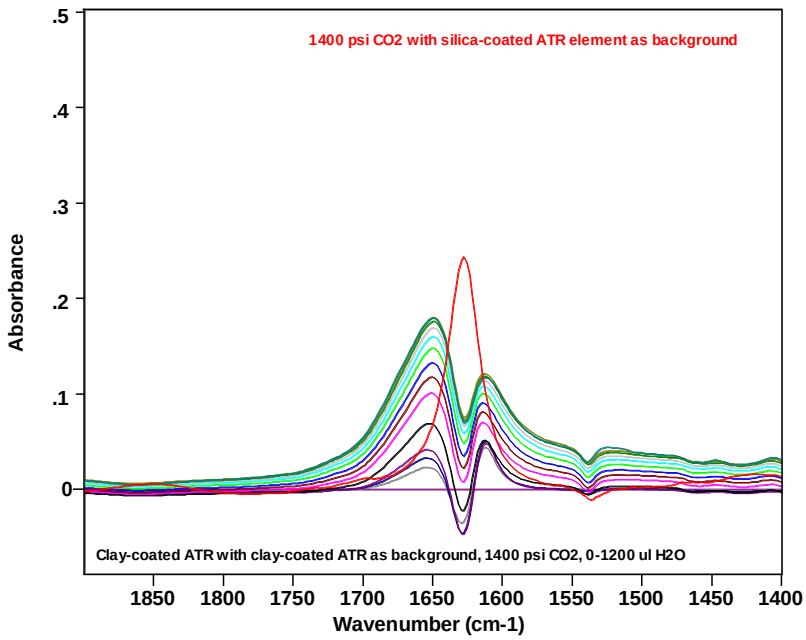

Figure 29. FTIR spectra with clay coatings in $scCO_2$ with increasing H_2O (expanded-frequency-scale of water bend-mode region).

3.2.4 Implications for Geologic Carbon Storage

The data collected here is still under analysis. For instance, relative thicknesses of the water films on silica in N_2 and in $scCO_2$ have not been calculated at this time. Therefore, it is not yet possible to assess whether the water sorption data shown are quantitatively consistent with the water adsorption model developed in Section 2. However, that data do qualitatively agree with the water film model. At a given a_w (P_w/P_{sat}), less water is adsorbed to the silica surface in supercritical CO_2 than in N_2. Moreover, less water is sorbed onto, and into a clay film in $scCO_2$. The thin film model predictions, and these validating results, have important implications with respect to anticipated changes in relative permeability during dryout and rewetting of reservoir and caprock lithologies during CO_2 sequestration

A second important conclusion is that there is no evidence for CO_2 intercalation into the structure of the swelling clay. Although it might be suggested that the lower water sorption observed for the Ca-montmorillonite indicates displacement of waters of hydration by CO_2 in the clay interlamellar regions, this is unlikely. There is no change in the CO_2 infrared bands for the dry versus humid CO_2 conditions, and it is extremely unlikely that CO_2 intercalation could occur without any constraint of the CO_2 molecule. Certainly, formation of carbonate or bicarbonate species, perhaps complexed with the interlayer cation, did not occur. If CO_2 entered the interlayer sites, it did so in a state essentially unchanged from the external $scCO_2$ state. The observed decrease in water sorption by the clay film in $scCO_2$ is probably caused by thinner water films on the crystallite outer surfaces, and correspondingly less capillary condensation in the pores between the crystallites.

4. DETERMINING ROCK HYDRAULIC PROPERTIES IN SUPERCRITICAL CO_2: IN-SITU MEASUREMENT OF SHRINK-SWELL BEHAVIOR OF CLAY IN DRY-TO-WET SUPERCRITICAL CO_2 USING NEUTRON SCATTERING

4.1 Introduction

The Carbon Capture, Utilization, and Storage (CCUS) community has identified shrink-swell properties of clay-rich caprock as a risk for creation and/or exacerbation of leakage pathways at subsurface CO_2 storage sites [18]. Injected, anhydrous CO_2 will dissolve water to solubility limits such that subsequent dry-out of clays by CO_2 near wellbores may occur. Ilton et al. [43] and Schaef et al. [42], using *in situ* high pressure X-ray diffraction (XRD), observed changes in smectite clay interlayer spacing upon exposure to CO_2 at variable water content, which suggests dehydration and potential shrinkage of caprock. In contrast, using Monte Carlo and molecular dynamics simulations, Botan et al. [41] investigated interlayer spacing of smectite under varying amounts of water and CO_2, but neither shrinkage nor swelling were observed. Clay swelling against an applied pressure or under constant volume conditions and water imbibition can produce swelling pressures up to, for example, ~ 10 MPa (1450 psi) [71]. A recent study examines CO_2 intercalation and shrink-swell under conditions of non-hydrostatic stress [72], but without water. Limited work on CO_2-brine systems with swelling clays, with equivocal conclusions and not under realistic subsurface stress states, indicates the need for additional research. With neutron scattering methods, we examine the pore structure, fluid saturation, and swelling pressures of smectite clay as a function of dry-to-wet supercritical CO_2 ($scCO_2$) under uniaxial strain. The neutron methods seem promising because neutrons can pass through adequately designed pressure vessels, thus allowing studies of representative high pressure dry-to-wet CO_2 environments under non-hydrostatic stress.

The neutron experiments aim to address the question: what is the change in pore structure (i.e., compaction or expansion due to swelling pressures) of aggregates of clay (reference smectite SWy-2) as a function of dissolved water content in $scCO_2$ and degree of water saturation (liquid water volume per volume of voids) under uniaxial strain? Preliminary sets of experiments were run in February–March and August–September of 2013 using two types of pressure vessels. Both vessels are uniaxial strain pressure vessels or oedometers. The first oedometer sample chamber was overly large for small angle neutron scattering (SANS), which resulted in data that are difficult to interpret. A redesigned oedometer was better optimized for the optics of SANS and used in recent tests in August and September.

4.2 Methods

We performed test-of-concept neutron-beam experiments during February 28–March 2, 2013, at the Los Alamos Neutron Science Center (LANSCE) using the Low-Q Diffractometer (LQD). We investigated pore structure of smectite pellets (initial dry bulk density of ~ 1.3 g/cm^3). These experiments used a custom-designed, titanium uniaxial-strain, high pressure vessel or oedometer (Figure 30). The titanium (i.e., Ti 6Al-4V) has low neutron attenuation and is resistant to acidic water-CO_2 mixtures. The sample chamber of the Ti oedometer is 25.4 mm (1-inch) diameter,

which proved to be overly large for SANS (see results in Section 4.3); however, the Ti oedometer sample chamber may still be suited for other neutron scattering instruments at LANSCE (e.g., the High-Pressure-Preferred Orientation time-of-flight diffractometer or HIPPO, but so far we were unable to use the HIPPO). The Ti oedometer is designed with a factor of safety of 4× for maximum allowable working pressure (MAWP) within the sample chamber of 27.6 MPa (4000 psi; a pressure safety data package with full details is available upon request, which includes the results of a 1.3× overpressure test). Test conditions included non-confined or "neat" samples; and pellets placed in the oedometer under axial stress with dry and wet (saturated with D_2O) $scCO_2$, with fluid pore pressure and axial stress being ~ 1315 psi and ~ 1760 psi, respectively, at the beginning of the tests (pressure may have dropped during the tests) and a temperature of ~ 40°C.

A second round of experiments in August and September 2013 was conducted using a stainless steel and aluminum oedometer that was optimized for the neutron optics of the LQD. This oedometer has an Al sample chamber thickness normal to the direction of the beam of approximately 3.2 mm (0.13 in). Figure 30 presents a schematic of the oedometer with annotation regarding fluid inlets and/or outlets, sample location, and dimensions. Although originally designed for a MAWP of 20.7 MPa (3000 psi), the results of an overpressure test determined the MAWP should be 6.9 MPa (1000 psi), which is below the critical point of CO_2. The second round of experiments includes collection of neutron data when the pore pressure was zero (1.85 kg/m^3 CO_2 density) and from approximately 5.7 to 5.5 MPa (840 to 800 psi), at a temperature of approximately 18.2°C (liquid CO_2 densities of ~ 800 to 792 kg/m^3). The axial load is applied by a narrow piston (Figure 31) that magnifies the applied hydraulic fluid pressure by a factor of ~ 7.74 due to the ratio of areas of the top part of the hydraulic piston and the lower narrow packing ram.

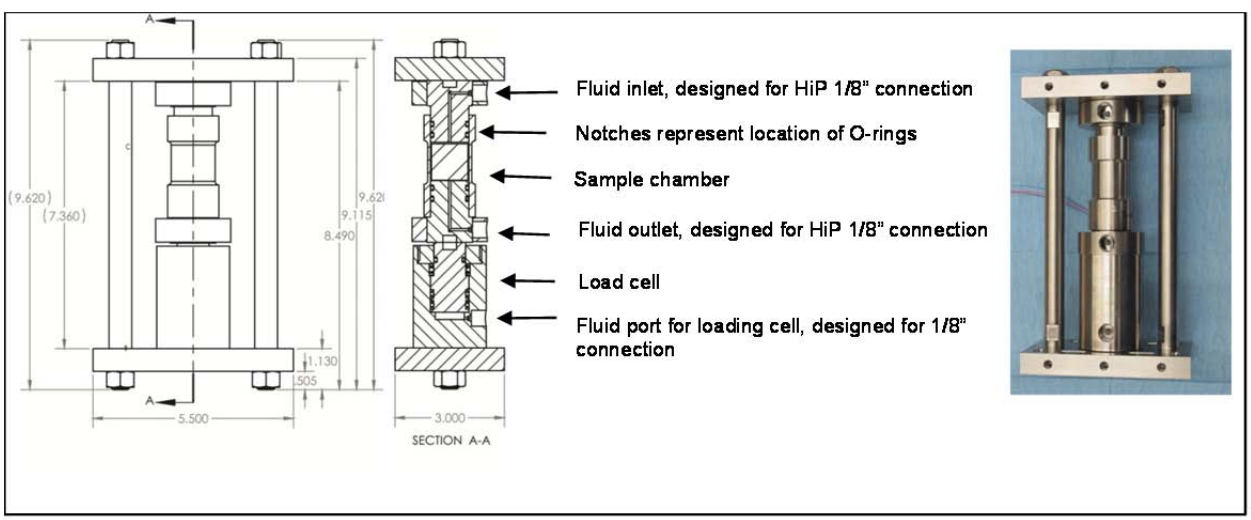

Figure 30. Schematic and photo of Ti oedometer with dimensions.

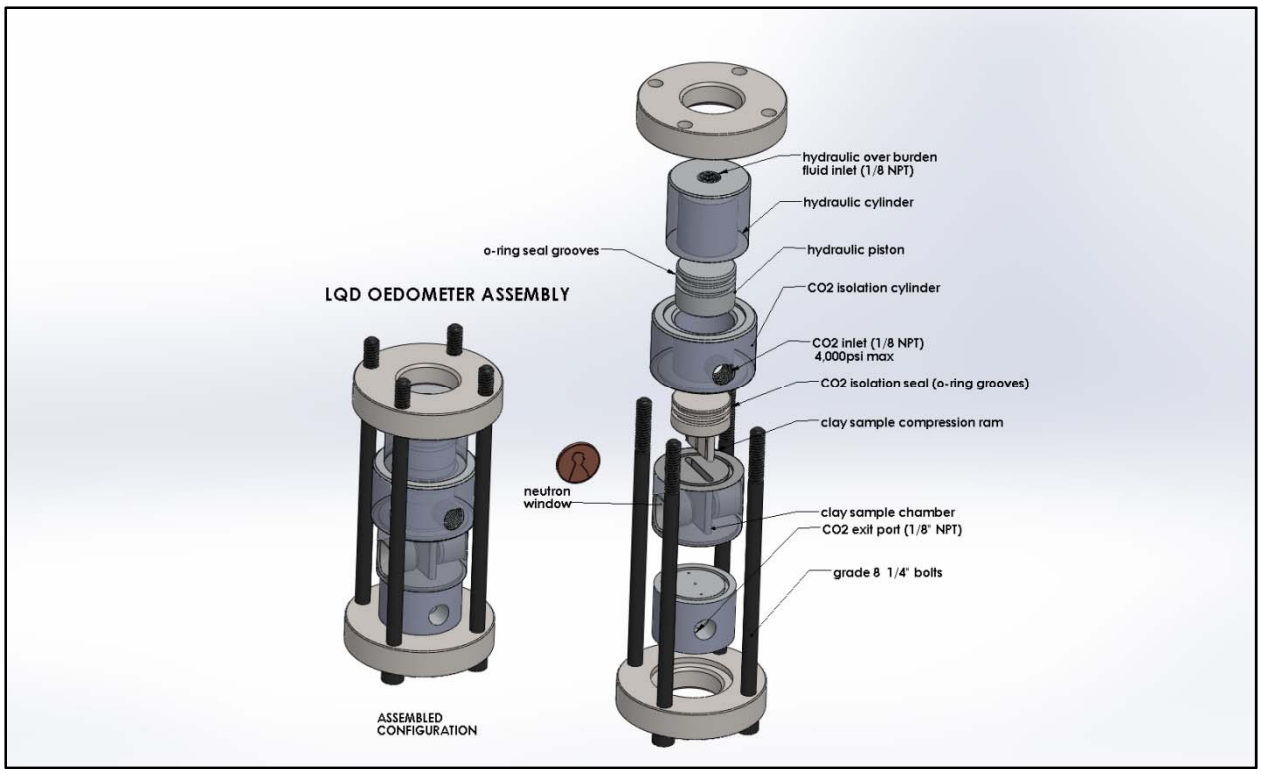

Figure 31. Schematic diagram of second oedometer with annotation indicated by arrows. Note penny for scale. (Figure courtesy of Mark Taylor, Los Alamos National Laboratories)

4.3 Results and Discussion

For the Ti oedometer, the neat and dry CO_2 had similar scattering intensity *I* (Q) as a function of the scattering vector *Q***,** whereas the D_2O-saturated $scCO_2$ sample may exhibit some measurable difference from the neat (Figure 32); however, the difference may decrease substantially depending on the data reduction that copes with noise in the data. Data interpretation is underway with help from LANSCE scientists, but preliminary findings indicate multiple neutron scattering. The peak and knees in the data may be artifacts or at least affected by the multiple scattering: work is underway to address the multiple scattering with methods similar to Mang and Hjelm [73]. The results are promising in that dry versus wet data may reflect both changes in scattering length and hence fluid saturation, and pore structure changes. If multiple scattering can be treated successfully, the remaining analysis will address pore size distributions for the neat, dry, and wet samples for the measured compaction and stress states. However, the multiple scattering is very strong and thus the newer stainless steel and aluminum oedometer (Figure 31) was designed and built to be optimized for the optics of SANS. Note that when D_2O-saturated CO_2 was flowed through the dry-CO_2 sample, instead of swelling pressures developing, the sample actually compacted further.

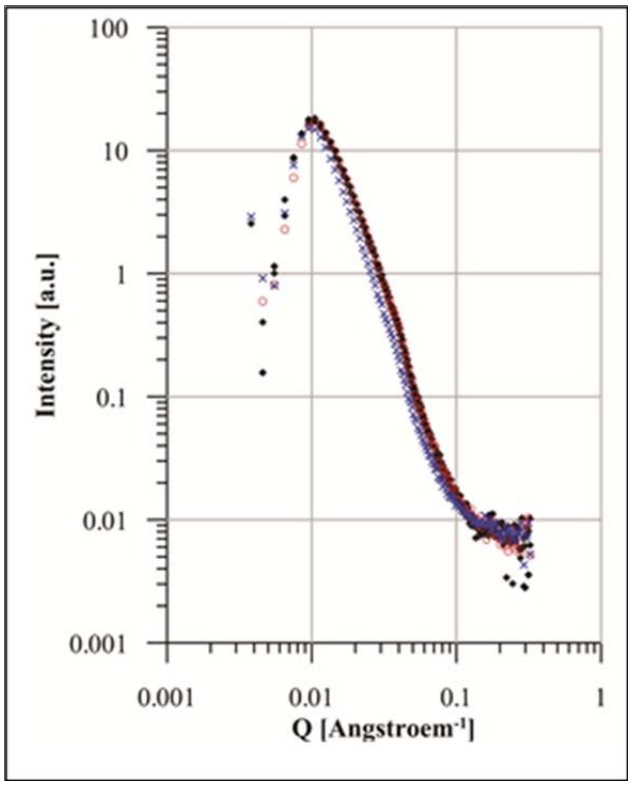

Figure 32. Example of preliminary LQD results using the titanium oedometer. Black diamonds represent neat (i.e., not placed in vessel) pellets under no axial stress. Red and blue are, respectively, for dry and wet (D_2O-saturated) high pore pressure CO_2 conditions under axial load.

Preliminary results from the stainless steel-aluminum oedometer were obtained the week of September 16, 2013, for low and relatively higher (up to ~ 5.5 MPa) pressures (Figure 33). Data labeled 37502 are for approximately zero gauge pore pressure and a packing ram axial pressure of ~ 2.0 MPa (286 psi). The other data are for pore pressures approximately between 5.7 to 5.5 MPa (840 to 800 psi). At higher pressure, the pore pressure may have supported the packing ram. The clear difference in the data for the low and high pressure conditions may reveal changes in pore structure and interaction between the CO_2 and clay. Tests were not yet performed with D_2O-saturated CO_2 at high pressure. Data interpretation is underway for determining pore structure for the different states of stress. In general, neutron methods seem to be a promising tool to reveal pore structure information for in-situ high pressure non-hydrostatic CO_2-rich conditions.

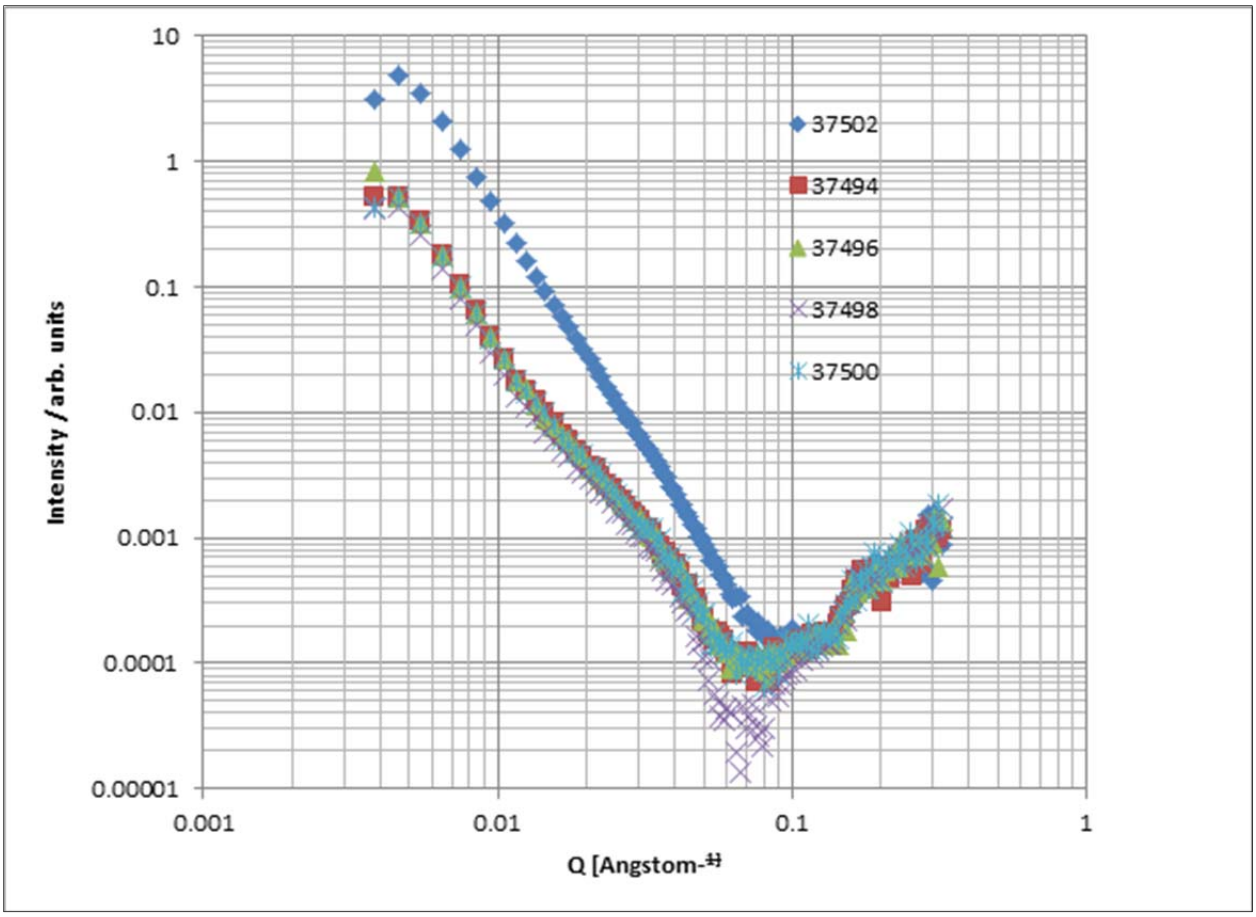

Figure 33. Preliminary results for the stainless steel-aluminum oedometer (note these data are preliminary).

5. ASSESSING MINERAL SURFACE REACTIVITY IN HYDROUS SUPERCRITICAL CO_2

5.1 Introduction

Geologic sequestration in deep saline aquifers is being considered as a viable option for mitigating release of carbon dioxide into the atmosphere [74-76]. Predictions for the long-term stability and containment of sequestered CO_2 are critical to implementation of CO_2 storage projects, and can depend heavily on assumptions made with regard to CO_2/mineral interactions in the subsurface. Injected CO_2 enters the subsurface as a supercritical fluid, and both displaces and dissolves into subsurface brine in the storage reservoir. The interaction of wet supercritical CO_2 ($scCO_2$) with rocks in the host formation potentially results in mineral alteration, which, in turn, may have important effects on CO_2 injectivity [17], CO_2- plume distribution [77], and the permanence of the storage operation [18]. Additionally, $scCO_2$ may interact with caprock lithologies, compromising the seal integrity of the injection formation [78].

Mineral reactions with the water-CO_2 supercritical phase may have several potential effects on the hydrological properties of the host and caprock formations. Volume changes associated with mineral dissolution/precipitation affect porosity and may have a disproportionate effect on permeability within the storage formation, if localized in channels or pore throats. Alteration mineral composition and extent of alteration also have important implications for secondary sequestration in the form of chemical trapping (e.g. carbonate precipitation). Moreover, alteration that changes surface mineralogy or morphology can lead to altered wettability. Mineral wetting properties strongly affect reservoir permeability with respect to water and the supercritical phase, play a key role in determining integrity of caprock seals, and control capillary and residual trapping processes and hence, reservoir storage capacity estimates [79].

Both the alkali and plagioclase feldspars are relatively abundant in target CO_2 storage reservoirs. Microcline and albite are a major component in parts of the Mt. Simon sandstone; the feldspars are present as diagenetic overgrowths and contribute preferentially to pore linings [80], implying a potentially important role for feldspars in the pore alteration and reactivity during CO_2 operations in the Mt. Simon. Possible subsea host reservoirs being considered by Taiwan and Japan are feldspar-rich greywackes. Muscovite, too, is a common minor detrital phase in sandstones and is compositionally similar to illite, a major component of caprock shale seals for potential reservoirs. Calcic plagioclase is abundant in mafic igneous rocks, and may contribute, in addition to the magnesium silicates, to the chemical trapping of CO_2 sequestered in mafic rocks.

The dissolution of feldspars in aqueous solutions at ambient pressures has been extensively evaluated. A full discussion of this topic is beyond the scope of this paper; the reader is referred to reviews in Blum and Stillings [81], as well as Alexeev [82]. The general model for feldspar dissolution under acidic conditions, far from equilibrium, proceeds as follow: 1) interstitial cations are exchanged for hydrogen ions, 2) aluminum ions are liberated either via complexation possibly involving hydrogen ions or by direct exchange with hydrogen ions, and 3) framework silicates, depending on the feldspar composition, are either released along with Al-release from the framework (when the Si:Al ratio = 1) or by hydrolysis of Si-O bonds [83]. A Si-rich

"leached layer" is postulated to form during incongruent dissolution of feldspar under acidic conditions (pH ≤ 3), when solution conditions are such that rates of silicate hydrolysis rates are outpaced by removal of both interstitial cations and tetrahedral-coordinated aluminum. It is worth noting that it has been also asserted that the leached layer may, in actuality, be formed from silicate re-precipitation (as opposed to being a relic of the silica framework leached of interstitial cations and aluminum). As shown in albite dissolution experiments by Kawano and Tomita [84], the Si-rich layer may serve as a platform for the growth of clays and clay minerals, and the leached layer on dissolving feldspars may, in fact, serve as a precursor for more stable mineral phase. It has been proposed that halloysite, a precursor to the more stable kaolinite, may actually form via an amorphous aluminosilicate that may be approximated as allophane [85].

In contrast, the literature for feldspar dissolution in systems containing $scCO_2$ is relatively sparse. Several studies have focused on the carbonation reaction of hydrous supercritical CO_2 with forsterite [7, 9, 86, 87]. These studies also investigated the role that water plays in surface reaction by comparing reactivity between mineral/water/$scCO_2$ and mineral/anhydrous $scCO_2$ systems, or by characterizing surface reactions and/or reactivity as a function of water saturation in the $scCO_2$ phase. Overall, it is reported that "wet" $scCO_2$ is more reactive and that reactivity is a function of water content in the $scCO_2$ phase. Shao et al. [11] investigated dissolution and secondary mineralization of phlogopite exposed to both brine equilibrated with $scCO_2$ and humid $scCO_2$. As with the forsterite studies, it was reported that hydrous $scCO_2$ resulted in greater reactivity of phlogopite, which was attributed to the formation of water films on the mineral surface. In terms of reaction in CO_2-saturated brines, Shao et al. also reported that while dissolution rates increased with increasing salinity, lower salinity produced nano-scale secondary mineralization at a faster rate and to a greater extent. Hu et al. [88] assessed biotite dissolution in CO_2-saturated brines, and also found that salinity increased dissolution rates for biotite, and found that rates decreased with decreasing hydrated metal cation size. Other studies that have compared anhydrous and hydrous $scCO_2$ conditions include studies of brucite [10] and granite [8] mineral substrates, both of which also concluded that hydrous $scCO_2$ is more reactive with mineral substrates than anhydrous $scCO_2$. Lin et al. [8] identified the plagioclase phase of the granite specimen as the most reactive with hydrous $scCO_2$, and report that its dissolution leads to formation of an unknown aluminosilicate secondary phase on the mineral surface. Sorai et al. [89] investigated anorthite dissolution in water equilibrated with $scCO_2$ at 10 MPa and over temperatures ranging from 25-80 ° C. Samples were characterized by atomic force microscopy both before and after exposure to $scCO_2$-saturated water. Surface alteration was reported to increase with temperature, and this included faster dissolution rates and greater surface roughening at higher temperatures. Regnault et al. [90] also exposed anorthite to 2-phase mixtures of water and $scCO_2$, as well as anhydrous $scCO_2$. These experiments were carried out at 16 MPa and 200 ° C and reported extensive secondary mineral formation of smectite clays and calcite in the water-saturated case, and similar secondary mineralization in the form of small clay sheaves in the anhydrous case.

The objectives of this study are several: 1) to understand the dissolution/precipitation behavior of several representative minerals exposed to CO_2/water mixtures under both ambient pressure and high pressure conditions 2) to identify the changes to key chemical and physical surface properties that result from CO_2/water/mineral interaction, and 3) to identify secondary minerals

precipitated under in situ conditions, so as to understand how host rock and caprock formations may be impacted by interaction with humid $sccCO_2$ during a CO_2 storage operation.

5.2 Methods and Materials

5.2.1 Mineral Samples and Preparation

Samples of the minerals albite, orthoclase, labradorite, and muscovite were acquired from different sources. Crystal structure, composition, homogeneity and lack of alteration were verified by X-ray diffraction (Bruker D-8 diffractometer), SEM observation (FEI Magellan 400), and electron microprobe analysis (JEOL 8200 Electron Probe Microanalyzer). Mineral compositions are given in Table 2; each is an average of at least 10 microprobe analyses. The analyses indicate that the samples are representative—concentrations of trace elements such as barium and lithium, occasionally enriched in feldspars and muscovite, were too low to detect. The albite and orthoclase are near end-member compositions. All samples were gem-quality and homogeneous; no exsolution lamellae were observed in any of the feldspars, even under SEM examination. However, microscopic mineral inclusions were observed in the albite and muscovite.

Table 2. Summary of minerals used for the study, including source and chemcial composition as determined by electron probe microscopy.

Mineral	Location	Chemical Composition
Albite	Minas Gerais, Brazil	$(Na_{1.00}Ca_{0.01}K_{0.01})Al_{1.07}Si_{2.94}O_8$
Orthoclase	Mt. Biti, Madagascar	$(K_{1.00}Na_{0.02})(Al_{0.99}Fe_{0.05})Si_{2.98}O_8$
Labradorite*	Chihuahua, Mexico	$(Na_{0.40}K_{0.02}Ca_{0.59})Al_{1.65}Si_{2.35}O_8$
Muscovite	Ingersoll Mine, S. Dakota, USA.	$(K_{0.90}Na_{0.08})(Al_{2.91}Fe_{0.12}Mn_{0.01}Si_{2.96}O_{10}(OH_{1.83}F_{0.17})$

* This material was originally identified as bytownite.

Feldspar samples were coarsely crushed to fragments a few mm in diameter, and individual, clean cleavage fragments were selected for use. Muscovite samples were cleavage flakes, trimmed to ~4 mm^2 with scissors. Following selection, sample materials were thoroughly rinsed with deionized water to remove fine dust and any salts that may have been released from crushed fluid inclusions. Finally, samples were dried by rinsing repeatedly with anhydrous ethanol.

5.2.2 Experimental Setup and Conditions

Mineral dissolution experiments were carried out under several conditions. Most were carried out under ambient pressures (0.83 bars at the elevation of Albuquerque, NM). Samples were exposed to humid conditions with P/Psat values of 0.6, 0.8, and 1.0 in a CO_2 environment (0.83 bar of CO_2). Two sets were immersed in DI water, one with a CO_2-saturated headspace (0.83 bar CO_2) and another under "ambient" headspace (CO_2 partial pressure of ~ $10^{-3.42}$). A single set were carried out in humid (P_w/P_{sat} = 0.8) supercritical CO_2 at a pressure of 137.4 bar.

For conditions at 0.83 bar CO_2 (P_w/P_{sat} = 0.6, 0.8, 1.0 and immersed in DI water), experiments were carried in a CO_2 atmosphere inside a laboratory oven that was used to control temperature, as well as modified and equipped to serve as a humidity chamber. Immersed samples were placed in 100 mL polypropylene centrifuge tubes, filled with ~95 ml of DI water. The tubes were arranged vertically in a beaker in the oven -- the lids will have a hole drilled to allow gas exchange. Samples were also placed in a separate oven in which the CO_2 partial pressure is ambient, i.e. $10^{-3.42}$ bar. As with the immersed samples under 0.83 bar CO_2, these samples were placed in 100 ml polycarbonate centrifuge tubes, with about 95 ml of DI water. The lids were tightly fastened, with a hole drilled into the lid to allow gas exchange.

For high pressure, elevated temperature experiments in $scCO_2$, mineral dissolution experiments were carried out in a specialized experimental apparatus. Figure 34 shows a schematic of the $scCO_2$ system. As shown in Figure 34, ISCO syringe pumps were used to control water and CO_2 flow into a pressure vessel that serves as an equilibration vessel, saturating the $scCO_2$ with water at 40 ºC. Temperatures throughout the system were controlled by heating blankets/tape and temperature controllers (not shown in Figure 34). An Eldex® Optos pump was used to meter the humidified $scCO_2$ from the equilibration vessel through a manifold and into the Poly Ether Ether Keytone (PEEK) pressure cells containing the mineral samples, which are maintained at 50 ºC in a water bath. Because of the temperature difference between the equilibration chamber and the sample cells, the cells are at a lower saturation, corresponding to an activity of water of 0.8 (P_w/P_{sat}). Nominal flow rates were in the range of 0.08-0.12 mL/min. On the downstream side of the pressure cells, the cells were routed through a PEEK manifold, which was connected to a PEEK back pressure regulator that vented to atmosphere.

5.2.3 Post-test Sample Characterization

Scanning Electron Microscopy (SEM) and Energy Dispersive X-ray spectroscopy (EDS) analysis were performed on a FEI Magellan 400. Samples were coated with a 10 nm layer of Au/Pd prior to analysis and imaging. Cross-sections were prepared for transmission electron microscopy (TEM) analysis using a Dual Beam FEI Quanta 3D Field Emission Gun SEM. A 10 μm × 2 μm rectangle to 5 μm depth using a Ga-source focused ion beam (FIB). A 2 μm Pt coating was deposited on the mineral surface to protect surface features, i.e. secondary minerals, during FIB thinning of the cross-section. The cross-sections were removed from the sample and welded to the TEM grid using an Omniprobe micromanipulator, thinned to ~100 nm using the FIB, and analyzed using a JEOL 2010F FASTEM Field Emission Gun STEM/TEM. Secondary minerals were also identified using a variant of a method described by Hu and Jun [91], where reacted minerals were sonicated for 30 minutes in anhydrous ethanol and the supernatant was pipetted onto Cu TEM grid and analyzed by TEM (JEOL 2010F FASTEM and JEOL 2010 HRTEM).

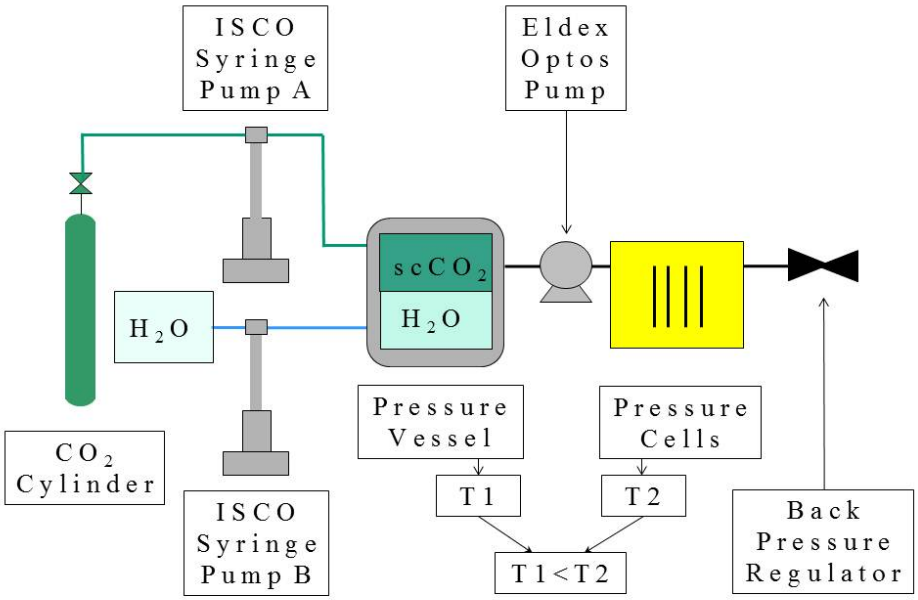

Figure 34. High pressure experimental setup. Mineral samples were loaded into pressure cells and exposed to a $scCO_2/H_20$ mixture. P_w/P_{sat} was controlled by holding T2 at a higher temperature than T1, which corresponds to a vessel containing water saturated $scCO_2$.

5.3 Results and Discussion

5.3.1 Ambient Pressure Experiments

The results of SEM analysis for samples under ambient pressure are summarized in Table 3. For samples exposed to humid conditions, dissolution behavior (etching and pitting) of each sample increases with P/Psat. At low water activities, corrosion was local, and secondary mineral growth was largely confined to step edges. Secondary minerals were localized into droplike distributions. It is possible that capillary condensation at the step may have been a necessary condition for dissolution of the mineral surface. Alternatively, cations released during dissolution of the primary mineral may have resulted in formation of condensed droplets at the step locations. Immersed samples, both at 0.83 bar CO_2 and $10^{-3.42}$ bar CO_2, show a significant increase in etching and secondary mineral coverage relative to the humidified samples.

The increase in water/solid ratio – moderate for increased P/Psat and large in the immersed -- ensures that the aqueous phase stays far from saturation with respect to primary mineral constituents. In both immersed cases, this is manifested by a marked increase in pitting for all 4 minerals, relative to the samples in humid CO_2. In general, there is a marked increase in the precipitation of secondary minerals with increasing P/Psat; however, in the 0.83 bar CO_2

Table 3. Summary of conditions and results for ambient pressure experiments

Conditions	Mineral	Dissolution		Secondary Mineral Precipitation	Description
		Etching	Pitting		
Expt. #1: 0.83 bar CO_2, 40 °C P/P_{SAT} = 0.6 7 days exposure	Albite	x	x	**X**	Limited mineral precipitation, mostly on edges and little on terraces; size of precipitates <10nm
	Orthoclase	x	-	x	Step edges, <100nm features
	Labradorite	**X**	-	-	-
	Muscovite	x	-	x	Step edges, <100nm
Expt #2: 0.83 bar CO_2, 40 °C P/P_{SAT} = 1.0 7 days exposure	Albite	**X**	x	x	More etching and precipitation compared to expt #1; heaviest on edges, sparse on terraces; size of precipitates <10nm
	Orthoclase	**X**	-	-	-
	Labradorite	**X**	-	-	-
	Muscovite	x	-	x	Step edges, clusters
Expt. #3: 0.83 bar CO_2, 40 °C, Immersed in DI water 7 days exposure	Albite	x	**X**	x	Large pits; limited mineral precipitation on the periphery of etch pits; Size of precipitates <10 nm
	Orthoclase	**X**	x	-	-
	Labradorite	**X**	**X**	-	-
	Muscovite	x	-	-	-
Expt. #4: $10^{-3.42}$ bar CO_2, 40 °C Immersed in DI water 7 days exposure	Albite	x	**X**	**X**	Pervasive pitting; pervasive covering of surface by secondary minerals (most amorphous)
	Orthoclase	**X**	**X**	-	-
	Labradorite	**X**	x	-	-
	Muscovite	**X**	**X**	**X**	Film of coalesced sub-micron features
Expt. #5: 0.83 bar CO_2, 50 °C P/P_{SAT} = 0.8 14 days exposure	Albite	**x**	**x**	**X**	Heaviest on edges, sparse on terraces, <10nm; more precipitation than exp. #1.
Expt. #6: 0.83 bar CO_2, 50 °C P_w/P_{sat} = 1.0 14 days exposure	Albite	**x**	**X**	**X**	Widespread coating of 10nm spherules, heaviest on step edges and defects
Expt. #7: 0.83 bar CO_2, 50 °C, Immersed in DI water 14 days exposure	Albite	**X**	**X**	**X**	Widespread coating of 10nm spherules, heaviest on step edges and defects
Expt. #8: $10^{-3.42}$ bar CO_2, 50 °C Immersed in DI water 14 days exposure	Albite	**x**	**X**	**X**	Widespread coating of 10nm spherules, heaviest on step edges and defects, rods/needles ~500nm in length and 10nm in width

immersed case (7 days exposure), there is a notable decrease in precipitation for all 4 minerals, presumably owing to the lower pH (pH=3 vs. pH=5.6) of the CO_2 saturated aqueous phase in equilibrium with 0.83 bar CO_2 relative to the DI water under an "ambient" CO_2 partial pressure of $10^{-3.42}$. The lower pH increases solubility of secondary minerals, thus moving the system further from saturation with respect to secondary minerals. Time of exposure also plays an important role in the precipitation of secondary minerals, especially for immersed samples.

Ambient samples of albite immersed in DI in equilibrium with 0.83 bar CO_2 showed a marked increase in secondary mineralization when the time of exposure was increased from 7 days to 14 days. Doubling the exposure time provided time for the aqueous phase to saturate with respect to secondary minerals.

Figure 35 (Plates A-F) shows the effects of water content and P_{CO2} for each set of conditions for the albite samples. It is clear that the formation of secondary mineralization increases with water content, with the immersed samples showing extensive precipitation on all surfaces, including both step edges and terraces.

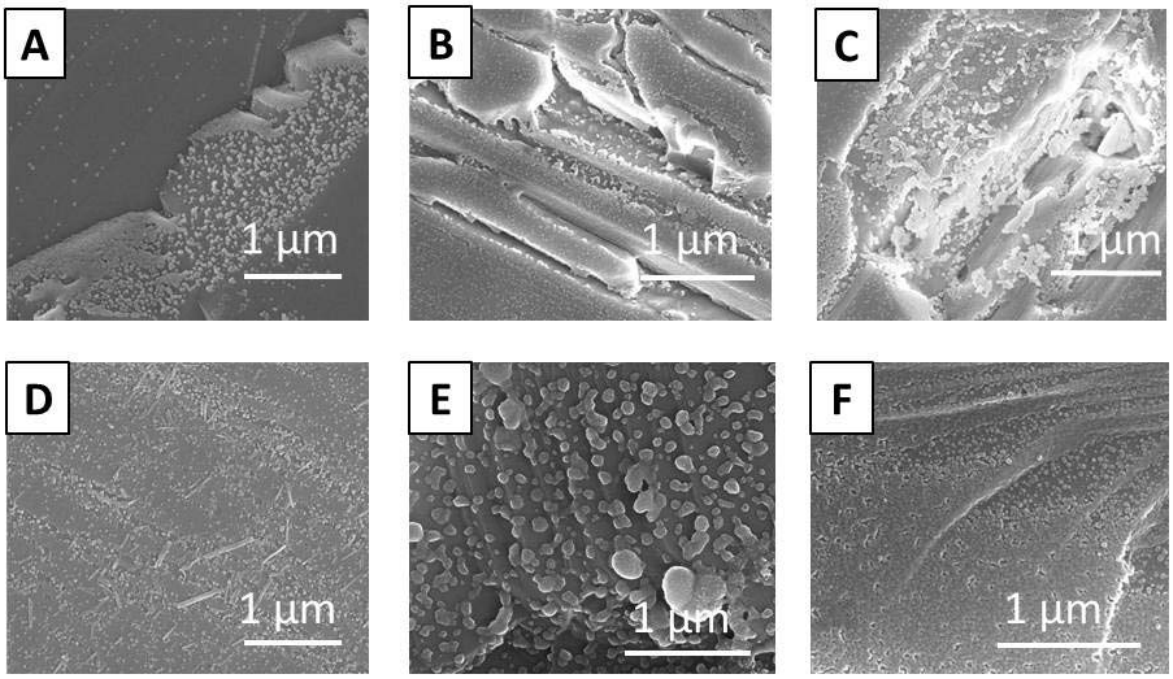

Figure 35. Summary of albite alteration for various conditions. A= Expt #5, B= Expt #6, C= Expt#7, D = Expt #8, E and F = Expt in $scCO_2$, P_w/P_{sat} = 0.9.

5.3.2 High Pressure Experiments in Humid Supercritical CO_2

The results of SEM analysis for samples under high pressure in humid $scCO_2$ are summarized in Table 4. All 4 minerals showed signs of secondary mineral dissolution, to an extent which equaled or surpassed that of gaseous CO_2 for both P_w/P_{sat} values. Both orthoclase and labradorite showed increased secondary mineralization relative to their respective counterparts under ambient pressure (which includes the immersed samples). Both albite and muscovite showed precipitation that was more widespread on the surface than counterparts at ambient pressure in humid gaseous CO_2. However, both albite and muscovite showed comparable levels of secondary mineralization, and heavier dissolution in the immersed case under $10^{-3.42}$ bar CO_2, probably because the mineral/water system was closer to saturation than the lower pH aqueous solution produced under 0.83 bar CO_2. Figure 36 shows a gallery of images for all four minerals after exposure to humid $scCO_2$.

As mentioned, albite exposed to humid $scCO_2$ shows widespread coating of spherules of amorphous material, as well as isolated pockets of coarser spherules or radiating crystals (see plates E and F, Figure 35). Additionally, there are also isolated pockets of clay minerals, some of which resemble features seen on muscovite in humid $scCO_2$ (see Figure 36, plate 4). Orthoclase under these conditions shows widespread precipitation of spherules at step edges, and in some areas this grows out onto terraces, as seen in Figure 36, plate 2. Some denser coatings, containing e-beam sensitive potassium-rich mineral phases, were also seen on orthoclase surfaces. labradorite shows isolated features apparently representing dried deliquesced droplets on the mineral surface; displaying with a filmy, probably amorphous residue, as well as umbrella-like structures with strand-like bases supporting a flat or bulbous roof off of the surface (see Figure 36, plate 3). Muscovite shows several distinct morphologies, some of which are potentially clay minerals (Figure 36, plate 4).

Table 4. Summary of conditions and results for high pressure experiments

Conditions	Mineral	Dissolution		Secondary Minerals		
		Etching	Pitting	Present?	Morphology	Identified as:
137.9 bar CO_2 50 °C P_w/P_{sat} = 0.8 14 days exposure	Albite	**X**	x	**X**	Widespread coating on most of the surface	Kaolinite, 200nm crystals
	Orthoclase	**X**	x	**X**	Step edges, some coating on terraces	*TBD*
	Labradorite	x	**-**	x	Islands of roof-like structures	*TBD*
	Muscovite	x	**-**	x	Isolated pockets of clays, extensive coating of micron-sized features	*TBD*

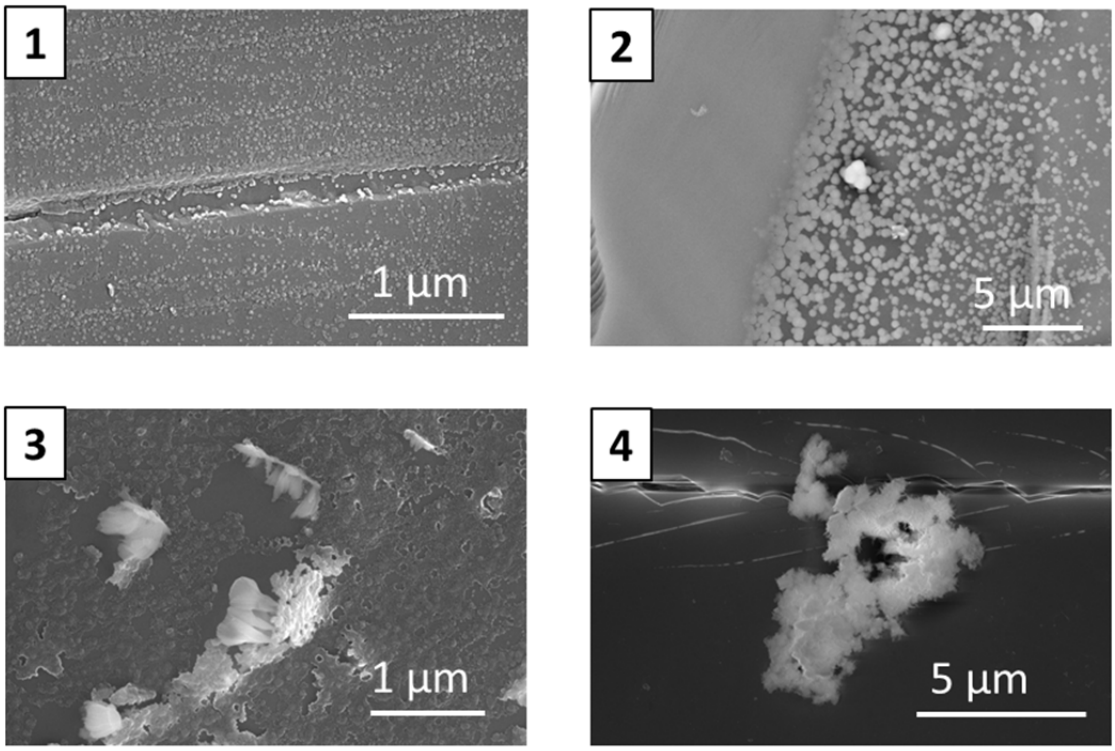

Figure 36. SEM images of test minerals exposed to $scCO_2$. 1) Albite, 2) Orthoclase, 3) Labradorite, and 4) Muscovite

Cross-sections of each feldspar mineral sample exposed to humid $scCO_2$ were prepared via Focused Ion Beam (FIB) and analyzed by TEM/EDS. Profiles of elemental compositions were used to determine if a leached layer – a silica-rich zone depleted of interstitial cations -- was present in any of the minerals exposed to humid $scCO_2$. Results for albite were equivocal, as Na loss during FIB thinning may have occurred. However, for orthoclase, a leached layer a few hundred nm thick was identified, in an area with moderate secondary mineralization (Figure 37). Labradorite, which showed the least secondary mineral formation among the feldspars, did not exhibit a leached layer.

5.3.3 The Role of Capillary Condensation in Secondary Mineral Formation under Humid Conditions

Capillary condensation in surface pits and at cleavage step edges clearly plays a role in the formation of secondary mineral phases, especially on the albite and orthoclase samples. This is evidenced in both the ambient pressure and the high pressure experiments in $scCO_2$. For the ambient pressure cases, in general, samples exposed to humid CO_2 showed most or all alteration at defects and step edges, with the coverage increasing out onto terraces with increased water content. For high pressure experiments, a similar trend is seen in terms of alteration extent increasing at surface pits and step edges. Overall, the water to solid ratio plays a key role in the precipitation of secondary minerals -- both in the extent of coverage and morphology of features -- as evidenced by the fact that the heaviest mineralization occurred either in immersed samples or in low lying defects where thicker water films can form by pooling.

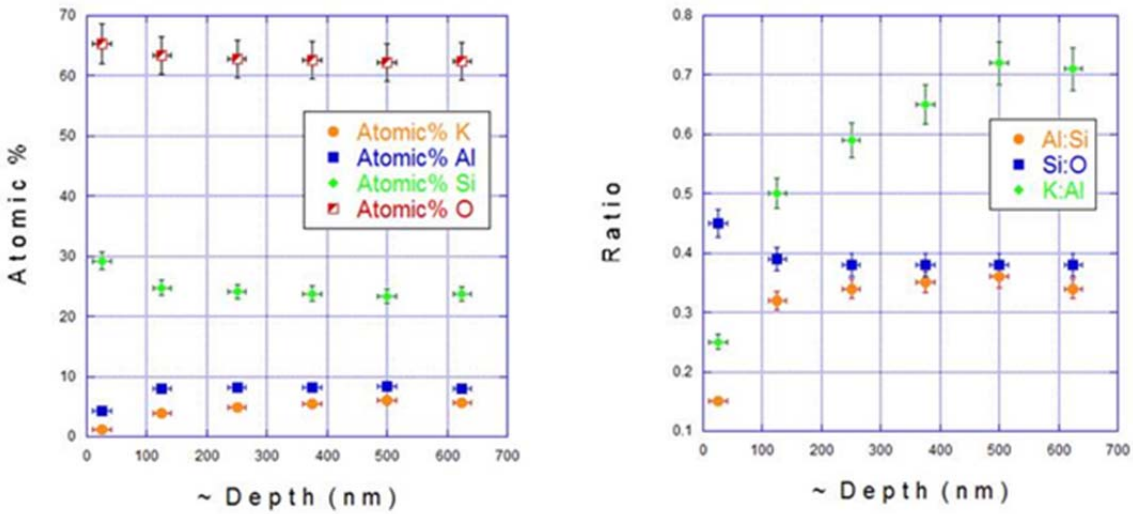

Figure 37. TEM/EDS element profile for orthoclase—atomic composition and ratio of elements

For high pressure experiments, there is evidence for secondary mineral formation that appears to be the result of deliquescent droplet formation. This is especially true for labradorite, where most of the precipitated features bear the appearance of having formed in this manner. This phenomenon was also evident in select areas on orthoclase, albite, and muscovite. It is not clear if these droplets were formed during exposure to $scCO_2$ under elevated pressure, or if they were formed during either system depressurization or drying of the minerals. It seems likely that under certain conditions, those water layers may occur in patches or drops as indicated by the presence of isolated circular surface domains that exhibits distinct mineral precipitation patterns.

5.3.4 Surface Alteration by Dissolution and Secondary Mineral Formation

The potential effects of surface alteration can be either chemical or physical; both will manifest changes in the wetting properties of the mineral surfaces in this study. Alteration of wetting properties has important implications for CO_2 storage operations, including CO_2 plume movement/distribution, storage capacity estimates, and caprock sealing efficiency.

Given the reactants present, there are a finite number of potential reaction products that can compose the secondary mineral phases. It could be expected that carbonates of Na, K, and Ca, may form as the interstitial cations are leached from albite, orthoclase and labradorite. Both K and Na are volatile under SEM and can be difficult to detect and/or identify. Secondary minerals composed of aluminosilicates are also apt to form as well.

5.4 Implications for Carbon Storage in Geologic Reservoirs

Mineral alteration during supercritical CO_2 injection and subsequent subsurface storage may significantly change reservoir/caprock properties such as porosity, permeability, and mineral surface wettability, thus directly affecting well injectivity and CO_2 plume distribution and mineralization in a storage reservoir. To better understand such processes, a systematic experimental study was carried out to assess the potential for surface alteration of reservoir-caprock minerals upon exposure to a wide range of physical and chemical conditions: (1) immersed in deionized (DI) water under air ($10^{-3.42}$ bar CO_2) and 40ºC; (2) immersed in deionized (DI) water under 0.83 bar CO_2 and 40ºC; (3) exposed to 0.83 bar CO_2 at various relative humidity (60%, 80%, and 100%) and temperatures (40 oC and 50 ºC); and (4) exposed to supercritical CO_2 (13.8 MPa) at 80% relative humidity and 50 ºC. The experiments were carried out for 7 or 14 days. Mineral investigated include albite, orthoclase, labradorite, and muscovite. All samples were analyzed by SEM/EDS and TEM/EDS. Albite samples immersed in DI water in equilibrium with air ($10^{-3.42}$ bar CO_2) experienced extensive mineral corrosion and precipitation as evidenced by the presence of extensive pitting and etching and pervasive secondary mineral coverage on flat surfaces. With an increased CO_2 concentration (0.83 bar), similar corrosion features were observed, but with much less secondary mineral precipitation, which was localized only to the inside of large corrosion pits, probably due to the reduction of secondary mineral saturation by solution acidification. In contrast, under ambient-pressure humid conditions, albite showed limited mineral dissolution and precipitation. The surface alteration increased with increasing RH. Secondary mineral formation was localized to cleavage steps and adjacent rims, where capillary condensation of water was likely to occur. Under ambient-pressure conditions, three other minerals (orthoclase, labradorite, and muscovite) displayed a similar trend as albite in surface alteration, but the extent of the alteration, especially for orthoclase and labradorite, was much less than observed for the albite.

Samples of all four minerals exposed to humid supercritical CO_2 exhibited widespread surface corrosion and secondary mineralization, to a much greater extent than samples exposed to humid ambient pressure conditions. Kaolinite and amorphous silica were identified among secondary minerals formed. TEM observations reveal that a leaching layer developed on orthoclase, with a thickness of a few hundred nanometers. These results imply that, in humid supercritical CO_2, thin water layers may form on mineral surfaces, thus facilitating mineral dissolution and precipitation. The limited liquid volume of the water layers appears not a major limiting factor for mineral alteration. Under certain conditions, those water layers may occur in patches or drops as indicated by the presence of isolated circular surface domains that exhibits distinct mineral precipitation patterns. Our work indicates that, even in a $scCO_2$ zone of a subsurface carbon storage reservoir, significant mineral alteration may occur due to water adsorption and capillary condensation, if the injected $scCO_2$ picks up some moisture during injection or storage. Such alteration may lead to significant modifications to reservoir or caprock hydrologic properties.

6. GANGLION DYNAMICS AND ITS IMPLICATIONS FOR GEOLOGIC CARBON DIOXIDE STORAGE

6.1 Introduction

Injection of supercritical carbon dioxide ($scCO_2$) into subsurface reservoirs is a possible option for the mitigation of carbon emissions to the atmosphere [92, 93]. The injected CO_2 can be trapped by various mechanisms including structural and hydrodynamic trapping, residual trapping, dissolution, and mineralization [94]. Structural trapping requires a reservoir to be capped by an impermeable formation (e.g. shale), whereas hydrodynamic trapping requires a head gradient to oppose migration of injected $scCO_2$. Residual trapping, or capillary trapping, has been considered to be attractive because it can potentially relax stringent requirements for cap rock integrity in structural and hydrologic trapping, allowing for utilization of uncapped or dipping structures for CO_2 storage. Capillary trapping of $scCO_2$ can significantly expand storage capacity through efficient utilization of subsurface reservoirs. It is important to note that capillary trapping has been shown to be a dominant mechanism for oil trapping in depleted oil fields. It has been found that, even following secondary recovery processes, more than 50% of the original oil remains trapped as a discontinuous phase [95, 96].

Capillary trapping of $scCO_2$ has recently been studied. Suekane et al. [97] suggest that co-injection CO_2 with water could be an effective scheme to control the initial gas saturation in porous media and maximize the volumetric ratio of CO_2 trapped to the total CO_2 injected. After water injection, most of the injected CO_2 can be trapped by capillarity. Qi et al. [98] show that co-injection followed by chase brine injection can render > 85% of the injected CO_2 immobile. Pore-scale simulations reveal complex behaviors of supercritical CO_2 movement and entrapment including coalescence, gravity fingering, division, and capillary trapping [99].

Two general modeling approaches have been used to evaluate immiscible displacement and capillary trapping: continuum and discontinuous (ganglion). In a continuum model, capillary trapping is described by the relative permeability of two liquids involved in displacement as a function of the saturation of each phase and the hysteretic behavior of capillary pressure-saturation functions [98, 100]. Material properties in those models are constrained by averaging the properties over a relatively large volume, larger than the size of individual nonwetting blobs. In contrast, in a ganglion model, the modeling effort is focused on the discontinuous nonwetting phase. Ganglion models have been applied to enhanced oil recovery [96, 101-104] and to the remediation of nonaqueous phase liquid (NAPL) contaminants in subsurface environments [105, 106]. Network models have been developed to study ganglion motion, breakup, and stranding [101] Amili and Yortsos [107] have used potential theory to model the hydrodynamic interaction between liquid and discontinuous gas ganglia in porous media. Percolation theory can provide insights into the stochastic flow behavior of a large population of fluid blobs in a two-phase flow system; specifically, it has been used to evaluate the size distribution of ganglia near the percolation threshold [108-110].

The objective of this research was to use the theory of ganglion dynamics to systematically study the mobility of $scCO_2$ injected into a water-wet subsurface porous medium such as a sandstone reservoir. Specifically, this study aimed to provide a general formulation for the generation,

mobilization, and entrapment of $scCO_2$ ganglia in subsurface environments and to demonstrate the concept that breaking up the injected $scCO_2$ into small blobs can potentially enhance capillary entrapment. Our work provides a new perspective for subsurface $scCO_2$ storage and monitoring.

6.2 Dynamics of Supercritical CO_2 Ganglia

6.2.1 General Model Formulation

We assume that the flow of both $scCO_2$ inside a ganglion and water outside follows Darcy's law:

$$\vec{V_s} = -\frac{k}{\mu_s}\vec{\nabla}(\mathrm{P_s} + \rho_\mathrm{s}\mathrm{gz}) \tag{6-1}$$

$$\vec{V_w} = -\frac{k}{\mu_w}\vec{\nabla}(\mathrm{P_w} + \rho_\mathrm{w}\mathrm{gz}) \tag{6-2}$$

$$\vec{\nabla}\cdot\vec{V_s} = \vec{\nabla}\cdot\vec{V_w} = 0 \tag{6-3}$$

where $\vec{V_s}$ and $\vec{V_w}$ are the velocity fields of $scCO_2$ and water, respectively; k is the permeability of the porous medium; μ_s and μ_w are the viscosity of $scCO_2$ and water, respectively; ρ_s and ρ_w are the density of $scCO_2$ and water, respectively; g is the gravitation acceleration; $\mathrm{P_s}$ and $\mathrm{P_w}$ are the pressures of $scCO_2$ and water, respectively; and z is the vertical coordinate pointing upward.

At the macroscopic $scCO_2$-water interface:

$$\vec{V_s}\cdot\vec{n} = \vec{V_w}\cdot\vec{n} \tag{6-4}$$

$$P_s - P_w = \sigma^*\vec{\nabla}\cdot\vec{n} + P_c \tag{6-5}$$

$$P_c = \begin{cases} \frac{2\sigma\cos(\theta)}{r_n} & \text{at an advancing front} \\ \frac{2\sigma\cos(\theta)}{r_p} & \text{at a receding front} \end{cases} \tag{6-6}$$

where $\vec{n}$ is the normal unit vector of the macroscopic ganglion surface pointing from $scCO_2$ to water; σ is the pore-scale surface tension between $scCO_2$ and water; P_c is the pore-scale capillary pressure; θ is the contact angle between the $scCO_2$-water interface and the underlying solid surface; r_n and r_p are the effective radii of pore throat and pore body, respectively; and σ^* is the effective macroscopic surface tension between $scCO_2$ and water – an empirical parameter to capture the effect of surface tension on the stability of macroscopic $scCO_2$-water interface. A typical pore structure in sandstone is shown in Figure 38a. The non-wetting $scCO_2$ phase tends to occupy large pore spaces as much as possible to minimize interfacial energy. As illustrated in Figure 38b and captured in Equation 6-6, at an advancing front, the capillary pressure is inversely proportional to the radius of pore throat, while, at a receding front, it is inversely proportional to the radius of pore body [105]. For simplicity, it is assumed that both advancing

and receding contact angles are similar [105]. Parameter σ^* is scale-dependent and can be related to σ by accounting for surface roughness [111]:

$$\sigma^* = C\sigma \tag{6-7}$$

with $C = b(d)^{1-D}$, where b is the fractal coefficient, d is the microscopic investigation scale, and D is the fractal dimension of the interface. It is assumed that both water and $scCO_2$ are non-compressible (Eq. 6-3). Equation 6-4 imposes velocity continuity across the interface for the normal component. Equation 6-5 accounts for the pressure drop across the macroscopic $scCO_2$-water interface [112], including both the effect of macro-scale surface tension σ^*, which tends to minimize the macroscopic surface area of a ganglion, and the effect of pore-scale capillarity, which tends to impede a $scCO_2$ blob snapping through pore throats.

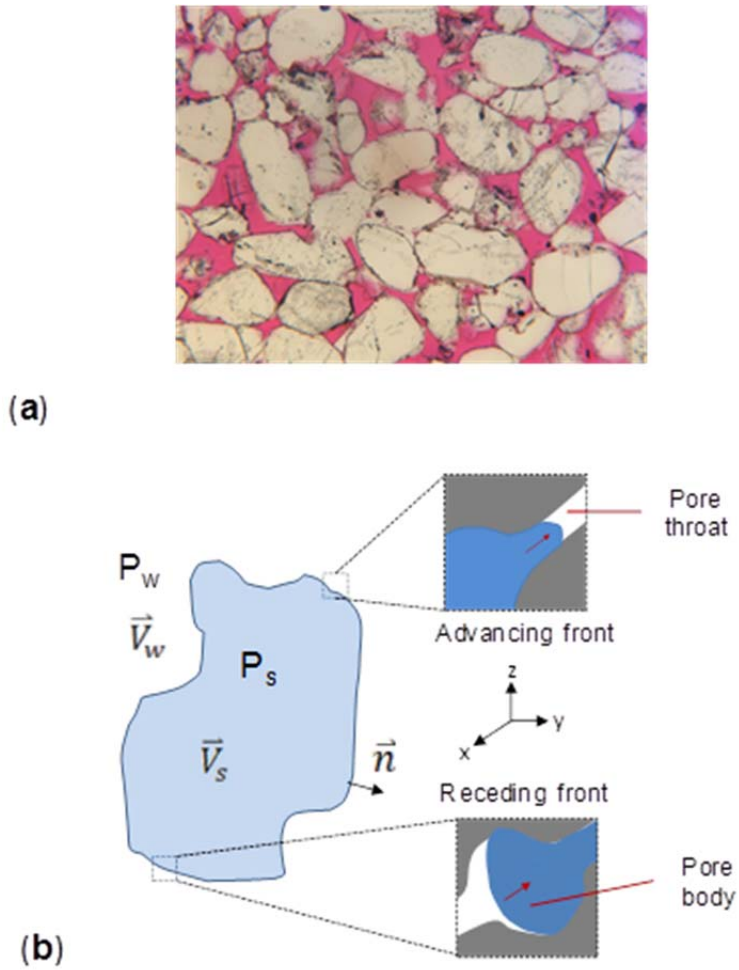

Figure 38. Conceptual model of pore structure and ganglion movement. (a) A thin section of Mount Simon Sandstone showing a typical sandstone pore structure, with red color indicating pore space (the horizontal field of view is 1.76 mm on the original specimen); (b) pore-scale ganglion movement at advancing and receding fronts. Symbols are defined in the text.

Let $F(x, y, z, t) = 0$ denote the macroscopic surface of a ganglion. The motion of the surface is related to the flow field by a kinematic equation:

$$\vec{V}_s \cdot \vec{\nabla}\mathrm{F} + \frac{\partial \mathrm{F}}{\partial \mathrm{t}} = 0 \tag{6-8}$$

where t is the time. The normal unit vector $\vec{n}$ can then be calculated by:

$$\vec{n} = \frac{\vec{\nabla}\mathrm{F}}{|\vec{\nabla}\mathrm{F}|} \tag{6-9}$$

Equations 6-1 to 6-9 constitute a moving boundary problem for the evolution of a $scCO_2$ ganglion in a porous medium. With appropriate boundary and initial conditions, this set of equations can be solved for the motion and morphological evolution ($\vec{V}_s$, F) of a single ganglion or multiple ganglia.

6.2.2 Trapping Criteria

By integrating Equation 6-5 for the force acting over the surface of a moving ganglion, using Stokes's theorem, we obtain:

$$\oiint \left(\sigma^* \vec{\nabla} \cdot \vec{n} + P_c\right) d\vec{S} = \oiint (P_s - P_w) d\vec{S} = \iiint \vec{\nabla} \cdot (P_s - P_w) dV$$
$$= \Delta\rho g V \vec{z} + \iiint \left(\frac{\mu_w}{k}\vec{V}_w - \frac{\mu_s}{k}\vec{V}_s\right) dV \tag{6-10}$$

where $\Delta\rho = \rho_w - \rho_s$; V is the volume of the ganglion; $\vec{z}$ is the vertical unit vector; and S is the surface area of the ganglion. The first term on the far right hand side represents the buoyancy force due to the density difference between water and $scCO_2$; the second and third terms, within the integral, account for the force exerted by groundwater pressure gradient (it is assumed that the flow field of water can be extended to the inside of the ganglion) and for the resistance which the ganglion has to overcome in order to move through the porous medium. An exact evaluation of Equation 6-10 would require a full solution of equations (1 - 9) for the flow fields. For simplicity, we make the following approximations:

$$\oiint \left(\sigma^* \vec{\nabla} \cdot \vec{n} + P_c\right) d\vec{S} \approx \Delta\rho g V \vec{z} + \left(\frac{\mu_w}{k}\vec{V}_w^0 - \frac{\mu_s + f\mu_w}{k}\vec{V}_s^g\right) V \tag{6-11}$$

where $\vec{V}_w^0$ is the average velocity of groundwater flow around the ganglion; and $\vec{V}_s^g$ is the velocity of ganglion movement as a whole. During movement, water will be displaced around the ganglion, moving from its advancing front to its tail at the same speed as the ganglion is advancing. This effect is captured by an effective viscosity $\mu_s + f\mu_w$ in Equation 6-11, where f is the ratio of the travel distance of water to the distance of ganglion movement [106, 113]. Since the water moves around the ganglion surface, f is expected to be slightly larger than 1. As a first order approximation, we set *f* equal to 1.

Let $\vec{l}$ denote the unit vector of net driving force for ganglion movement ($\Delta\rho g V \vec{z} + \frac{\mu_w}{k} V \vec{V}_w^0$). By setting $\vec{V}_s^g$ to zero, from Equation 6-11, the entrapment criterion for a ganglion is described by:

$$\left\|\Delta\rho g V\vec{z} + \frac{\mu_w}{k} V \vec{V}_w^0\right\| \leq \oiint \left(\sigma^* \vec{\nabla} \cdot \vec{n} + P_c\right) \vec{l} \cdot d\vec{S} \tag{6-12}$$

where $\vec{l} \cdot d\vec{S} \geq 0$ indicates an advancing front, and $\vec{l} \cdot d\vec{S} < 0$ indicates a receding front. The left hand side of the equation represents the total driving force contributed both by buoyancy and water flow, while the right hand side is the total impedance that needs to be overcome for a ganglion to be mobilized. For a no-flow (buoyancy-only) case, the trapping criterion becomes:

$$\Delta\rho g V \leq \oiint (\sigma^* \vec{\nabla} \cdot \vec{n} + P_c) \vec{z} \cdot d\vec{S} \tag{6-13}$$

Equation 6-12 indicates that capillary trapping of a $scCO_2$ ganglion is controlled by the pore-scale capillarity, the macro-scale surface tension, the geometry of the ganglion, and the water flow field. Generally, the curvature of a macroscopic water-$scCO_2$ interface is much smaller than that of the pore-scale interface. Thus, the first term in the integral in both Equation 6-12 and Equation 6-13 may be negligible compared to the second term, although it may play an important role in the morphological instability of a ganglion.

6.3 Model Analysis: First Order Approximation

In this paper, we do not solve the full set of equations formulated above. Instead, we only examine the first order approximation of the problem, in which a ganglion with a simple geometry is considered and the motion of an individual ganglion is separated from its morphological instability. With the simple ganglion geometry considered below, the integration of term $(\sigma^* \vec{\nabla} \cdot \vec{n})$ in Equations 6-12 and 6-13 vanishes. The parameter values used for these model analyses are summarized in Table 5.

6.3.1 Capillary Trapping of $scCO_2$ Ganglia in the Absence of Water Flow

For simplicity, consider a vertical, cylindrical $scCO_2$ ganglion with a height of H. From Equation 6-13, the entrapment condition for the ganglion is described by:

$$H < H_c = \frac{2\sigma\cos(\theta)}{\Delta\rho g}\left(\frac{1}{r_n} - \frac{1}{r_p}\right) \tag{6-14}$$

where H_c is the critical value of H. The contact angle between the $scCO_2$-water interface and the underlying mineral surface is an important factor controlling the effectiveness of capillary trapping. With increasing the contact angle, the trapping efficiency decreases, especially when the angle approaches 90º. The contact angle on a porous aluminum silicate substrate in $scCO_2$ was measured to be 10º to 40º, depending on the confining pressure [114]. Chiquet et al. [115] measured the contact angle for quartz and mica under various ionic strengths and confining pressure. The contact angle measured ranges 20º to 35º for quartz and 20º to 65º for mica. One complication with contact angle measurements is that this parameter is sensitive to surface roughness [116], and its determination for actual geologic materials can be challenging.

Table 5. List of parameter values used in the model analyses

Parameter	Value used in model analyses	Possible range	Sources
Microscopic surface tension of water-$scCO_2$ interface (σ)	0.04 N/m	0.035 – 0.05 N/m (pressure 8 – 17 MPa, temperature = 40 – 60 ^oC)	[117, 118]
Scaling factor for apparent surface tension (C)	3	2 – 4	[111]
Viscosity of aqueous solution (μ_w)	$7.5x10^{-4}$ N s/m^2	0.4 – $1.0x10^{-3}$ N s/m^2	[100]
Viscosity of $scCO_2$ (μ_s)	$4.0x10^{-5}$ N s/m^2	3.7 – $5.2x10^{-5}$ N s/m^2 (reservoir depth = 800 – 2000 m, thermal gradient = 3 ^0C/100 m)	[100]
Permeability (k)	10^{-10} m^2	10^{-12} – 10^{-10} m^2	[100]
Contact angle between the water-$scCO_2$ interface and the underlying solid surface (θ)	40 ^{o}	10 – 65 ^{o} (pressure = 26.6 – 48.9 MPa, temperature = 354.5 K)	[114, 115]
Density of $scCO_2$ (ρ_s)	650 kg/m^3	500 – 700 kg/m^3 for a storage depth of 0.8 – 2 km with a geothermal gradient of 3 ^oC per 100 meters)	[119, 120]
Density of aqueous solution (ρ_w)	1,065 kg/m^3	1,000 – 1,150 kg/m^3	[121]
Gravitational acceleration (g)	9.8 m/s^2		

As shown in Figure 39 for three different contact angles, at a fixed size ratio of pore to pore throat, the critical vertical dimension (H_c) of a $scCO_2$ ganglion that can be trapped is inversely proportional to the pore diameter. In absence of groundwater flow, for typical sandstone with a pore diameter from 0.6 to 2 mm, capillarity alone can trap a ganglion with a vertical dimension of 3 to 30 cm.

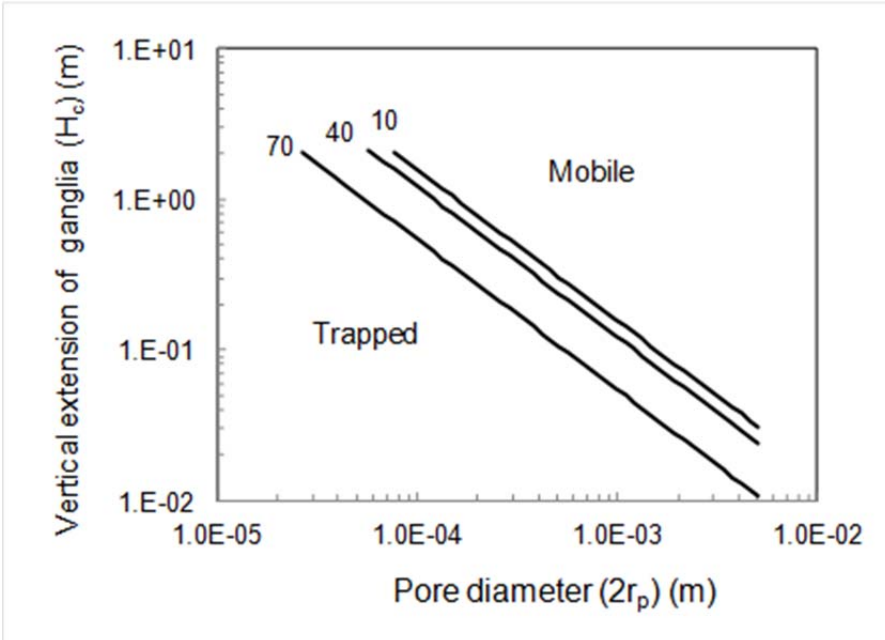

Figure 39. Critical vertical dimension for the entrapment of a $scCO_2$ ganglion as a function of pore diameter and contact angle (10º, 40º, and 70º) for a buoyance-only case. The size ratio of pore to throat is set to 5:1.

6.3.2 Effect of Reservoir Heterogeneity

Equation 6-14 can also be used to understand the effect of vertical heterogeneity within a reservoir rock on $scCO_2$ entrapment. Consider a horizontal less permeable layer (e.g. siltstone) within a permeable sandstone formation. Assume that a $scCO_2$ ganglion is trapped just beneath the finer-grained interbed rock. In this case, in order to move upward, the ganglion has to snap through the pore throats in the interbed at its advancing front, while retreating from the pore bodies in the sandstone at its receding front. In other words, the parameter r_n in Equation 6-14 now refers to the throat diameter of the interbed, while the parameter r_p remains to be the pore size of the sandstone. Assuming the same pore/throat size ratio for both the sandstone and the interbed, Figure 40 shows how the pore size (or particle size) of the interbed affects the critical size of a $scCO_2$ ganglion for trapping. The maximum vertical dimension of the ganglion that an interbed can effectively immobilize is a direct function of the size of its pores and the size of the pores of the underlying host formation. For example, for a shale cap rock, capillarity alone can inhibit upward movement of a ~50 meter thick layer of $scCO_2$. A siltstone layer, with a grain size 10 times smaller than that of the sandstone, can effectively cap $scCO_2$ ganglia (or banks) with vertical dimensions up to 3 m. A siltstone layer with a grain size 3 times smaller is enough to trap all ganglia with vertical dimensions up to 1 m. Therefore, the vertical heterogeneity of the reservoir formation is an important factor for enhancing $scCO_2$ entrapment. Numerical simulations indicate that trapping by finer-grained interbeds may account for up to ~ 35% of the total CO_2 immobilized [122]. The effectiveness of this mechanism has been demonstrated experimentally. In a CO_2 flooding column experiment, it was found that a thin layer of reduced

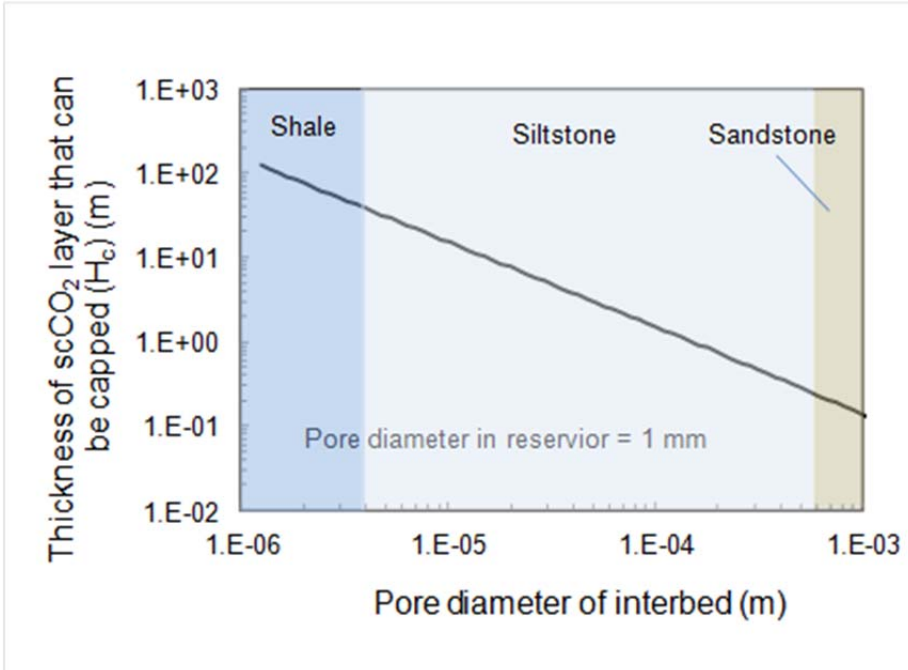

Figure 40. Effect of the pore size of an interbed on $scCO_2$ trapping. The ratio of pore diameter to throat diameter is 5:1 for both sandstone and interbed.

porosity at the exiting end of the column greatly increases (by a factor of 2-5 times) the residual CO_2 trapping in the core [123].

6.3.3 Making $scCO_2$ Ganglia

In principle, supercritical CO_2 ganglia can form through interface instability during immiscible displacement. In $scCO_2$ injection, the non-wetting CO_2 phase displaces the preexisting wetting phase (pore water). The morphologic instability of the displacement front is described by Equations 6-1 to 6-9. A stability analysis of Equations 6-1 to 6-9 for a planar front was obtained by Chuoke et al. [112]. When a planar interface between the two immiscible liquids advances at a constant velocity (V_s), instability occurs when V_s exceeds a critical value $V_{s,c}$ given by:

$$V_{s,c} = -\frac{\Delta\rho g k cos(\alpha)}{\mu_w - \mu_s} \tag{6-15}$$

where α is the angle between the vertical axis pointing upward and the normal direction to the interface pointing from $scCO_2$ to water. $V_{s,c}$ can be either positive or negative depending on the interface orientation. An unstable front would then become fingered, and the finger spacing λ is determined by:

$$\lambda = 2\sqrt{3}\pi \left[\frac{k\sigma^*}{(\mu_w - \mu_s)(V_s - V_{s,c})}\right]^{1/2} \tag{6-16}$$

Finger spacing predicted with Equation 6-16 has been shown to agree well with numerical simulations [100].

Now consider a case in which $scCO_2$ is injected to into a horizontal sandstone reservoir. The initial interface between CO_2 and preexisting brine is vertically aligned (i.e., α = 90º). The finger spacing for the front can be calculated as a function of the velocity of the moving front and the permeability of the reservoir (Figure 41). Finger spacing decreases with both increasing injection rate and decreasing permeability. For reasonable CO_2 injection rates, the CO_2-water interface becomes unstable, and the resulting finger spacing ranges from 1 cm to 30 cm. Alternating the injection of CO_2 with water should facilitate the formation of isolated ganglia.

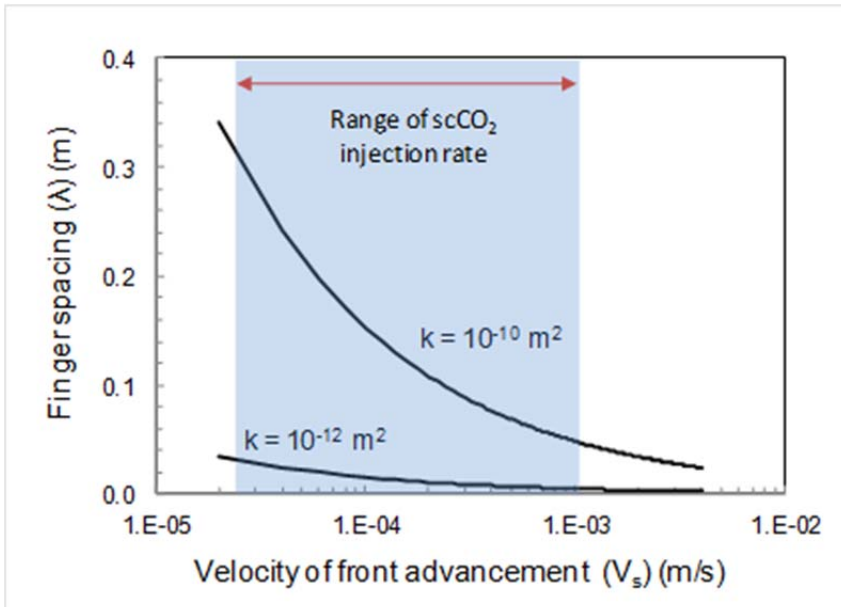

Figure 41. Finger spacing induced as $scCO_2$ displaces pore water during CO_2 injection, for two different reservoir permeabilities. The shaded area indicates the possible range of front velocities, assuming a typical CO_2 injection rate of 10^4 to 10^6 metric tons per year in a borehole of 0.3 m diameter and with 10 m injection interval. Finger spacing here is equivalent to the vertical dimension of a ganglion in Figure 39.

6.3.4 Fate of Moving Ganglia

Consider a vertical cylindrical $scCO_2$ ganglion in the absence of groundwater flow. From Equation 6-1, the velocity of ganglion rise can be estimated by:

$$V_s^g \approx \frac{k}{\mu_w+\mu_s}\left[\Delta\rho g - \frac{2\sigma\cos(\theta)}{H}\left(\frac{1}{r_n}-\frac{1}{r_p}\right)\right]. \qquad (6\text{-}17)$$

In Figure 42, the velocity of ganglion rise is calculated as a function of the vertical dimension (*H*) of the ganglion. A sufficiently large ganglion will rise, and its velocity will increase with its size. Because of interfacial instability, as described in the previous section, a large ganglion may experience further fingering at its advancing front and break into smaller pieces, causing further trapping.

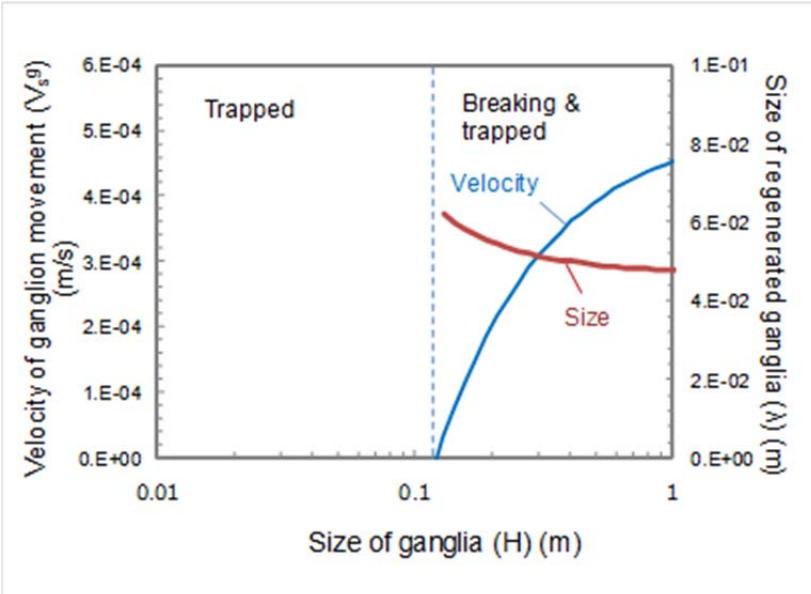

Figure 42. Ganglion breaking and trapping due to interface instability. The radii of pore throat and pore body are assumed to be 0.1 and 0.5 mm, respectively. To the left of the vertical broken line, ganglia are small and trapped. To the right, ganglia are large enough to attain sufficient rising velocities to cause further breaking up and trapping. The size of regenerated ganglia is calculated from Equations 6-15 and 6-16 by setting α = 0, and thus $scCO_2$ fingering due to gravity instability is automatically accounted. Since the size of regenerated ganglia is smaller than the critical size (~ 0.1 m) for mobilization, all regenerated ganglia become trapped.

A ganglion may grow as it moves due to coalescence with other ganglia in the pathway. However, once it becomes large enough, the ganglion will break up through interface instability. This breaking and trapping mechanism thus imposes an important limit on ganglion size evolution. In this sense, the mobility of a group of ganglia becomes self-limited. This concept points to a new way for making small ganglia for capillary trapping, that is, to inject $scCO_2$ into the bottom of the reservoir and then let it rise. As it rises, a CO_2 bank will automatically break up into small pieces. Based on a scaling analysis of Equations 6-1 to 6-9, the travel distance required for this breakup is probably on the same magnitude as the original ganglion size. Note that we here use terms of "size" and "vertical extension" interchangeably, because we expect that the surface tension of a ganglion would tend to minimize the aspect ratio of the ganglion.

6.3.5 Mobilization of $scCO_2$ Ganglia by Water Flow

Now consider the mobilization of $scCO_2$ ganglia in a water flow field. As shown in Figure 43 (solid line), the critical ganglion size for mobilization decreases with increasing water flow velocity. Once mobilized, a ganglion would be carried down along the water stream through entrainment. The velocity of a ganglion entrained depends on its size. Consider a horizontal cylindrical ganglion with its length of L and, for simplicity, ignore the buoyancy term in Equation 6-11. From Equation 6-11, the entrainment effect can be described by the velocity ratio of ganglion to the carrying fluid:

$$\frac{V_s^g}{V_w^0} = \frac{\mu_w}{\mu_w+\mu_s} - \frac{k}{\mu_w+\mu_s} \cdot \frac{2\sigma\cos(\theta)}{LV_w^0}\left(\frac{1}{r_n} - \frac{1}{r_p}\right)$$

$$= \frac{\mu_w}{\mu_w+\mu_s} - \frac{k}{1+\mu_s/\mu_w} \cdot \frac{2}{LCa}\left(\frac{1}{r_n} - \frac{1}{r_p}\right). \quad (6\text{-}18)$$

where C_a [$=\mu_w V_w^0/\sigma cos(\theta)$] is the capillary number. For a given size, a ganglion would be entrained only when the carrying flow velocity exceeds a critical value (the intercept of a dash line with the X-axis) (Figure 43). It seems unlikely for a regional groundwater flow (say, with a flow rate < 10-5 m/s) to mobilize any injected $scCO_2$ once the $scCO_2$ phase is broken into small ganglia with a size less than 40 cm. During a CO_2 injection time period, however, due to high flow rates, $scCO_2$ ganglia may be carried away by water flows. In a given water flow field, a larger ganglion would move faster than a smaller one. As it moves, a large ganglion may grow by coalescence with other ganglia in the pathway, and may eventually break up due to interface instability. The movement of a ganglion can also potentially be affected by the presence of its neighboring ganglia, leading to a so-called crowding effect [107], a research topic that warrants a further study.

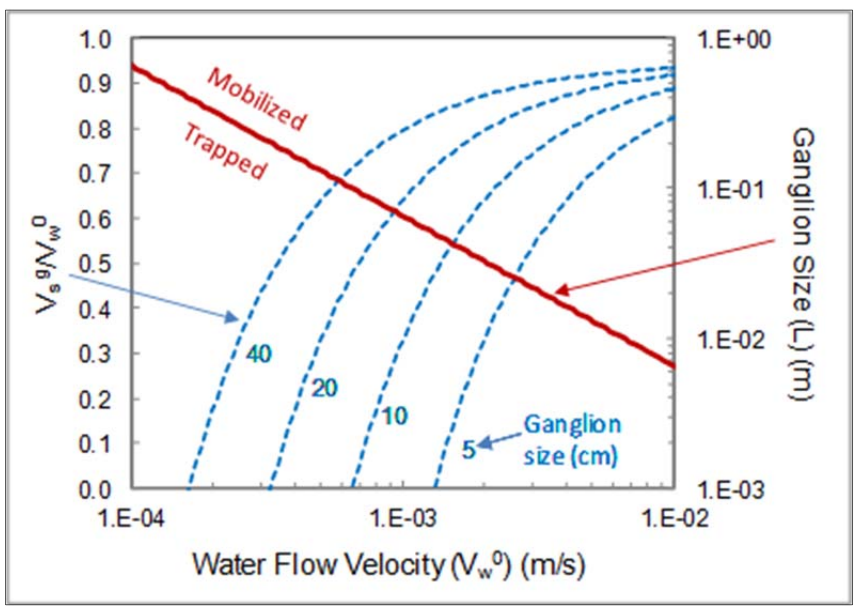

Figure 43. Mobilization and entrainment of ganglia by flow field. Larger ganglia would be more easily mobilized and move faster than the smaller ones in a given flow field. The radii of pore throat and pore body are assumed to be 0.1 and 0.5 mm, respectively.

6.4 Model Analysis: First Order Approximation

The model formulated above provides a unified framework to relate the capillary trapping of $scCO_2$ to key controlling factors such as ganglion size, surface tension, contact angle, rock pore structure, and the chemistry of phase interfaces. Our model analyses demonstrate that capillary trapping can be an important mechanism for long-term geologic storage of CO_2. The analyses show that the movement of a $scCO_2$ ganglion is inversely dependent on its dimension: the smaller the ganglion, the more difficult it is to move. Therefore, breaking the injected supercritical CO_2 into small ganglia can significantly enhance the effectiveness of capillary trapping. A large, mobile ganglion can potentially break up into smaller, less mobile ganglia through the instability of the CO_2-water interface during buoyant rise, and therefore the mobility of $scCO_2$ in the subsurface is self-limited. The $scCO_2$ ganglia can be made through deliberately engineered interface instability of immiscible flows, and their size distribution can be controlled by CO_2 injection mode and rate.

Ganglion dynamics presented above provides a new perspective for maximizing subsurface CO_2 trapping and safe storage. As shown in Figure 41, a relatively homogeneous medium with a larger grain size (i.e. high permeability), which is favored for high reservoir injectivity, would result in larger $scCO_2$ ganglia due to great permeability. However, larger pores and larger ganglia would reduce the effectiveness of capillary trapping, as indicated in Figure 39. Therefore, there should be an optimal pore size for capillary trapping of $scCO_2$, balancing permeability and porosity (Figure 44). Our work also shows that the vertical structural heterogeneity of reservoir rock can greatly enhance CO_2 ganglion trapping (Figure 40). Therefore, a sandstone formation with a medium grain size and significant vertical heterogeneity may constitute an ideal medium for capillary trapping of $scCO_2$.

Our model analyses paint a complex picture of population dynamics of $scCO_2$ ganglia in the subsurface. Percolation theory predicts that, near a percolation threshold in immiscible displacement, when the non-wetting liquid starts to become disconnected, the number (p) of ganglia of size L follows a power law [110]:

$$p(L) \sim L^{-\tau} \tag{6-19}$$

where τ is a constant (= ~ 2.0). This relationship has been confirmed by directly imaging the size distribution of gas bubbles co-injected with water into sandstone columns [97]. As discussed above, a large ganglion can spontaneously break up during movement. The critical size estimated in Figure 39 and Figure 42 thus imposes an upper limit on the size distribution of $scCO_2$ ganglia. The actual distribution may follow a truncated power law. The capacity of a geologic medium for capillary trapping can then be related to the key controlling factors by Equation 6-20:

$$CCT \propto \int_{r_p}^{H_c} p(L)dL = \frac{1}{r_p} - \frac{\Delta\rho g}{2\sigma\cos(\theta)} \frac{r_p r_n}{r_p - r_n} . \tag{6-20}$$

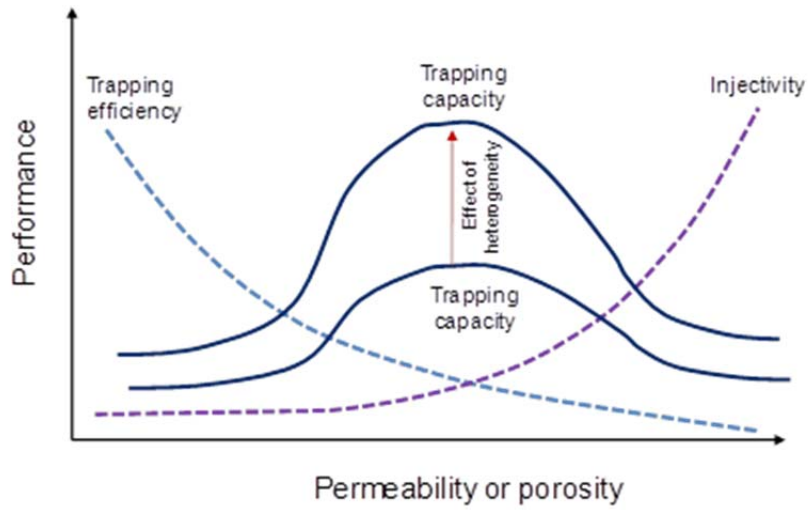

Figure 44. Schematic illustration of the existence of an optimal condition for $scCO_2$ capillary trapping.

This relationship is qualitatively consistent with the measurements of residual saturation for $scCO_2$ and n-decane in brine-saturated Berea sandstone [114]. The measurements show a systematically higher residual saturation for n-decane than that for $scCO_2$. Note that n-decane has a relatively smaller density difference ($\Delta\rho$) and higher surface tension (σ) than $scCO_2$.

The maximum capacity of capillary trapping can be estimated by assuming that it corresponds to the percolation threshold, at which the non-wetting phase just becomes disconnected. The percolation threshold depends on the shape and the size uniformity of ganglia [124]. Based on a simple cubic lattice calculation, the threshold is estimated to be 0.341 for ganglia with a uniform size [110]. This is consistent with a recent column experiment, which shows that the maximum residual supercritical CO_2 phase in Berea sandstone is about 35% [114] This seems reasonable, considering that the core sample used in this experiment is small (~ 4 cm in diameter and 8 cm in length) and, as a result, the size distribution of ganglia is limited to a relatively narrow range. In an actual reservoir, however, the size of ganglia is expected to distribute over a much broader range, and the actual capacity could be higher. As pointed out earlier, one advantage of capillary trapping is that this mechanism does not require a cap rock or the structural integrity of cap rock. Therefore, the total capacity of sequestration by capillary trapping on a regional scale could be significant.

As discussed above, the key parameters controlling capillary trapping of $scCO_2$ include: the surface tension, the contact angle, and the pore structure of the media. There are large uncertainties associated with each of these parameters. First, contact angles for many reservoir-relevant minerals are poorly known for the potential range of reservoir pressure, temperature, and chemical conditions. Furthermore, contact angles can potentially be modified by the presence and properties of water films on mineral surfaces. The thickness of water film is controlled by mineral surface properties and pore-water chemistry [25]. Surface tension between $scCO_2$ and aqueous solution can potentially be affected by solution chemistry and possible

organic compound dissolution into either the supercritical phase or the aqueous solution, which may modify the interfacial properties between the two liquids. As indicated in Equation 6-7, the macroscopic effective surface tension σ^* is scale-dependent, which makes it difficult to characterize for an actual system. In general, chemical reactions will be enhanced by the formation of $scCO_2$ ganglia due to an increase in specific surface area of $scCO_2$. The key parameters identified here may then evolve with time. For example, dissolution of organics (e.g. oil residues) from mineral surfaces can change the wetting properties of the surface and therefore the liquid-mineral contact angle. Mineral dissolution and precipitation may change the pore structure of the storage media. For example, secondary mineral precipitation may enhance capillary trapping by reducing porosity or pore throat size specifically. As minerals dissolve and new minerals precipitate, the pore surface properties (e.g., surface roughness and chemical identity) will also change. Evaluating the importance of these effects on long-term CO_2 trapping is scientifically challenging.

As pointed out earlier, there are two general approaches to modeling immiscible displacement and capillary trapping: continuum models and ganglion models. In a continuum model, material properties are derived by averaging each property over a representative elementary volume. However, the analysis presented here indicates that the size of $scCO_2$ ganglia may distribute over a wide range following a power law and the size of large ganglia may exceed the size of what is generally considered to be a representative element volume. More importantly, this work shows that the size of a ganglion is one of the most important factors controlling capillarity trapping of $scCO_2$ ganglia. None of the existing continuum models explicitly account for the important effect of ganglion size.

The ganglion concept developed above also provides a reasonable explanation for seemingly contradictory observations on residual gas saturation in a porous medium. With an X-ray computer tomography (CT) technique, Suekane et al. [125] imaged the distribution of nitrogen gas bubbles in Berea and Tako sandstone in a core-flooding experiment. They found that, on a local scale (~1 mm), the residual gas saturation increases with an increase in porosity. However, on a core scale, the residual gas saturation exhibits an inverse relationship with porosity [125, 126]. These seemingly contradictory observations are actually the two different manifestations of the same immiscible displacement process. Based on the earlier discussions, a non-wetting fluid tends to occupy large pore spaces as much as possible to minimize gas-water interfacial energy. Therefore, on a scale close to pore size, the residual gas saturation should positively correlate with local porosity. However, on a bulk scale, because of the same tendency to minimize gas-water interfacial energy, smaller pores (actually smaller pore throats for this matter) would create more capillary resistance for gas bubbles to snap through pore necks, thus promoting residual trapping. Thus, on a core scale, the residual gas saturation should to be inversely correlated with porosity (i.e., pore size), as indicated in Equations 6-14 and 6-18.

Finally, the concept developed here may allow for the development of a new technique for characterizing and monitoring supercritical CO_2 in subsurface environments. For example, recent interest in using acoustic waves to enhance oil recovery has stimulated a significant amount of work on the interaction of acoustic waves with non-wetting oil blobs in porous media [127, 128]. It has been found that acoustic waves may induce capillary resonance of the blobs and the size of the blob (L) can be related to the resonant frequency (ω) by [127]:

$$L = \frac{16\sigma \sin(\theta)[1+\sin(\theta)]^2}{\rho_s (r_n + r_p)^2 \omega^2}. \tag{6-21}$$

As discussed above, supercritical CO_2 injected into a reservoir is likely to form discontinuous ganglia. It is reasonable to expect that acoustic wave attenuation at a specific wave frequency is mainly attributed to the capillary resonance of ganglia of the appropriate size. If this is true, then measuring the attenuation of acoustic waves at various frequencies may allow us to estimate the size distribution of $scCO_2$ ganglia in subsurface systems.

7. CONCLUSIONS

Carbon sequestration via underground storage in geologic formations is currently the only realistic approach for sequestering high-volume industrial CO_2 emissions. The existing multiphysics models for CO_2 sequestration do not adequately account for processes occurring at the $scCO_2$-mineral interface due to changing activity of water in the supercritical fluid, which may strongly affect core and reservoir-scale hydrologic properties. Interfacial processes control the wetting properties of minerals, and by affecting wettability (surface tension), affect the permeability of reservoir units and caprock seals with respect to water and $scCO_2$. Capillary condensation of water from $scCO_2$ and coalescence of water films will also affect the relative permeability of $scCO_2$ and the aqueous phase. Moreover, recent studies have shown that the development of a water layer controls the chemical reactivity at the $scCO_2$-mineral interface, may be critical to mineral dissolution reactions in $scCO_2$.

This work evaluates processes occurring at the $scCO_2$-mineral interface, and how those processes affect the macro-scale hydrologic properties of the reservoir host-rock and cap-rock. Theoretical, experimental, and modeling capabilities for understanding the interactions of supercritical CO_2-H_2O fluids with geologic formations have been developed. The research described here provides improved constitutive models and needed experimental data for incorporating processes at the mineral-$scCO_2$ interface into process models for CO_2 sequestration, and for evaluating and validating the long-term performance of subsurface CO_2 storage.

As part of this study, we have developed for theoretically assessing the formation and evolution of water films on mineral surfaces in $scCO_2$ as a function of $scCO_2$ water content. The model assesses both water adsorption and capillary condensation in $scCO_2$, and provides estimates both of film thickness and of water saturation as a function of pore size. Experimental assessments of water adsorption onto silica in N_2 and in $scCO_2$, using QCM and FTIR-ATR techniques, have confirmed the major conclusions of the model, showing that adsorbed water films are thinner in $scCO_2$ than in N_2 at ambient pressures. Also evaluated by these techniques was water uptake by montmorillonite clays. Water sorption by the clays was also less in $scCO_2$, probably because of the thinner water films and the resulting reduced saturations in the interparticle pores, as predicted by the water adsorption/capillary condensation model. It is notable that no evidence of CO2 intercalation into the clay structure was observed, in the FTIR study. However, only a single clay, a Ca-montmorillonite, was evaluated.

In a second study, high pressure titanium and aluminum pressure vessels were developed to evaluate clay interactions with $scCO_2$ by neutron beam methods, at temperatures and pressures typical of *in situ* CO_2 sequestration conditions. Although difficulties were encountered in developing the appropriate design for the pressure vessel, the final data sets indicate that the method has great promise for this application. The pressure vessels have generated much interest in the rock mechanics community, and a technical advance has been filed.

We also evaluated the reactivity of common aquifer and caprock minerals in humid $scCO_2$, and in humid air and CO_2 at ambient pressures as a baseline. Experiments with albite, orthoclase, labradorite, and muscovite showed that reactive water films develop on the surface of these

minerals in hydrous $scCO_2$, resulting in pitting and precipitation of amorphous silica/alumina and clay minerals, in the case of orthoclase, a thick leached layer forms on the mineral surface. In must cases, mineral precipitation is localized occurring preferentially at cleavage step edges, in surface pits, and in deliquesced droplets; it is possible that thickening of the surface water layer in areas with enhanced capillarity is a necessary prerequisite for fluid-rock reactions. Under *in situ* conditions, capillary condensation processes may cause mineral dissolution/precipitation reactions to preferentially occur in small pores and pore throats. Such preferential mineral precipitation would have a disproportionately large effect on hydrologic properties.

Finally, we have developed a model which describes the formation and movement of CO_2 ganglia in porous media, allowing assessment of the effect of pore size and structural heterogeneity on capillary trapping efficiency. The model results also indicate possible engineering approaches for optimizing trapping capacity, for which Sandia is seeking a patent.

8. REFERENCES

1. Wilson, E.J. and D. Gerard, eds. *Carbon Capture and Sequestration: Integrating Technology, Monitoring and Regulation*. 2007, Blackwell Publishing Ltd: Ames, Iowa. 269.

2. Audigane, P., et al., *Two-dimensional reactive transport modeling of CO_2 injection in a saline Aquifer at the Sleipner site, North Sea.* American Journal of Science, 2007. **307**(7): p. 974-1008.

3. Gaus, I., et al., *Geochemical and solute transport modelling for CO_2 storage, what to expect from it?* International Journal of Greenhouse Gas Control, 2008. **2**(4): p. 605-625.

4. McCafferty, E. and A.C. Zettlemoyer, *Adsorption of water vapour on α-Fe_2O_3.* Discussions of the Faraday Society, 1971(52): p. 239-&.

5. Sumner, A.L., et al., *The nature of water on surfaces of laboratory systems and implications for heterogeneous chemistry in the troposphere.* Physical Chemistry Chemical Physics, 2004. **6**(3): p. 604-613.

6. Asay, D.B. and S.H. Kim, *Evolution of the adsorbed water layer structure on silicon oxide at room temperature.* Journal of Physical Chemistry B, 2005. **109**(35): p. 16760-16763.

7. Kwak, J.H., et al., *The role of H_2O in the carbonation of forsterite in supercritical CO_2.* International Journal of Greenhouse Gas Control, 2011. **5**(4): p. 1081-1092.

8. Lin, H., et al., *Experimental evaluation of interactions in supercritical CO_2/water/rock minerals system under geologic CO_2 sequestration conditions.* Journal of Materials Science, 2008. **43**(7): p. 2307-2315.

9. Loring, J.S., et al., *In Situ Infrared Spectroscopic Study of Forsterite Carbonation in Wet Supercritical CO_2.* Environmental Science & Technology, 2011. **45**(14): p. 6204-6210.

10. Schaef, H.T., et al., *Brucite $Mg(OH)_2$ carbonation in wet supercritical CO_2: An in situ high pressure X-ray diffraction study.* Geochimica et Cosmochimica Acta, 2011. **75**(23): p. 7458-7471.

11. Shao, H.B., J.R. Ray, and Y.S. Jun, *Effects of salinity and the extent of water on supercritical CO_2-induced phlogopite dissolution and secondary mineral formation.* Environmental Science & Technology, 2011. **45**(4): p. 1737-1743.

12. Esposito, R.A., L.S. Monroe, and J.S. Friedman, *Deployment Models for Commercialized Carbon Capture and Storage.* Environmental Science & Technology, 2011. **45**(1): p. 139-146.

13. Haszeldine, R.S., *Carbon Capture and Storage: How Green Can Black Be?* Science, 2009. **325**(5948): p. 1647-1652.

14. Benson, S. and P. Cook, *Underground geological storage*, in *IPPC Special Report on Carbon Dioxide Capture and Storage*, B. Metz, et al., Editors. 2005, Cambridge University Press: New York, NY. p. 195-276.

15. Doctor, R., et al., *Chapter 4: Transport of CO_2*, in *IPCC Special Report on Carbon Dioxide Capture and Storage*, R. Pichs-Madruga and S. Timashev, Editors. 2005, Intergovernmental Panel on Climate Change, Cambridge University Press: Cambridge. p. 179-193.

16. Kim, K.-Y., et al., *Characteristics of Salt-Precipitation and the Associated Pressure Build-Up during CO_2 Storage in Saline Aquifers.* Transport in Porous Media, 2012. **92**(2): p. 397-418.

17. Pruess, K. and N. Muller, *Formation dry-out from CO_2 injection into saline aquifers: 1. Effects of solids precipitation and their mitigation.* Water Resources Research, 2009. **45**.

18. Gaus, I., *Role and impact of CO_2–rock interactions during CO_2 storage in sedimentary rocks.* International Journal of Greenhouse Gas Control, 2010. **4**: p. 73-89.

19. Nitao, J.J. and J. Bear, *Potentials and their role in transport in porous media.* Water Resources Research, 1996. **32**(2): p. 225-250.

20. Philip, J.R., *Unitary approach to capillary condensation and adsorption.* Journal of Chemical Physics, 1977. **66**(11): p. 5069-5075.

21. Philip, J.R., *Adsorption and geometry: the boundary layer approximation.* Journal of Chemical Physics, 1977. **67**(4): p. 1732-1741.

22. Tuller, M., D. Or, and L.M. Dudley, *Adsorption and capillary condensation in porous media: Liquid retention and interfacial configurations in angular pores.* Water Resources Research, 1999. **35**(7): p. 1949-1964.

23. Baveye, P.C., *Comment on "Physicochemical controls on adsorbed water film thickness in unsaturated geological media" by Tetsu K. Tokunaga.* Water Resources Research, 2012. **48**.

24. Or, D. and M. Tuller, *Hydraulic conductivity of partially saturated fractured porous media: flow in a cross-section.* Advances in Water Resources, 2003. **26**(8): p. 883-898.

25. Tokunaga, T.K., *Physicochemical controls on adsorbed water film thickness in unsaturated geological media.* Water Resources Research, 2011. **47**.

26. Kim, T.W., et al., *Thickness measurements of nanoscale brine films on silica surfaces under geologic CO_2 sequestration conditions using synchrotron X-ray fluorescence.* Water Resources Research, 2012.

27. Kim, Y., et al., *Dewetting of Silica Surfaces upon Reactions with Supercritical CO_2 and Brine: Pore-Scale Studies in Micromodels.* Environmental Science & Technology, 2012. **46**(7): p. 4228-35.

28. Giorgis, T., M. Carpita, and A. Battistelli, *2D modeling of salt precipitation during the injection of dry CO_2 in a depleted gas reservoir.* Energy Conversion and Management, 2007. **48**(6): p. 1816-1826.

29. Mathias, S.A., et al., *Role of partial miscibility on pressure buildup due to constant rate injection of CO_2 into closed and open brine aquifers.* Water Resources Research, 2011. **47, W12525, doi:10.1029/2011WR011051**.

30. Pruess, K., *Formation dry-out from CO_2 injection into saline aquifers: 2. Analytical model for salt precipitation.* Water Resources Research, 2009. **45, W03403, doi:10.1029/2008WR007102**.

31. Hovelmann, J., et al., *Direct nanoscale observations of CO_2 sequestration during Brucite $Mg(OH)_2$ dissolution.* Environmental Science & Technology, 2012. **46**(9): p. 5253-5260.

32. Kerisit, S., J.H. Weare, and A.R. Felmy, *Structure and dynamics of forsterite-scCO(2)/H2O interfaces as a function of water content.* Geochimica et Cosmochimica Acta, 2012. **84**: p. 137-151.

33. Loring, J.S., et al., *In Situ Infrared Spectroscopic Study of Forsterite Carbonation in Wet Supercritical CO_2.* Environmental Science & Technology, 2011. **45**(14): p. 6204-6210.

34. Loring, J.S., et al., *In Situ Infrared Spectroscopic Study of Brucite Carbonation in Dry to Water-Saturated Supercritical Carbon Dioxide.* Journal of Physical Chemistry A, 2012. **116**(19): p. 4768-4777.

35. Loring, J.S., et al., *Carbonation of forsterite exposed to water-saturated supercritical carbon dioxide.* Geochimica et Cosmochimica Acta, 2010. **74**(12): p. A631-A631.

36. Pruess, K., *ECO2N: a TOUGH2 fluid property module for mixtures of water, NaCl, and CO_2*. 2005, Lawrence Berkeley National Laboratory, LBNL-57952. p. 66.

37. Wang, S., I.M. Edwards, and A.F. Clarens, *Wettability phenomena at the CO_2-brine-mineral interface: implications for geologic carbon sequestration.* Environmental Science & Technology, 2013. **47**(1): p. 234-241.

38. Spycher, N. and K. Pruess, *CO_2-H_2O mixtures in the geological sequestration of CO_2. II. Partitioning in chloride brines at 12-100 degrees C and up to 600 bar.* Geochimica et Cosmochimica Acta, 2005. **69**(13): p. 3309-3320.

39. Tokunaga, T.K., *DLVO-based estimates of adsorbed water film thicknesses in geologic CO2 reservoirs.* Langmuir, 2012. **28**(21): p. 8001-8009.

40. McGrail, B.P., et al., *Water reactivity in the liquid and supercritical CO_2 Phase: has half the story been neglected?*, in *Greenhouse Gas Control Technologies 9*, J. Gale, H. Herzog, and J. Braitsch, Editors. 2009. p. 3415-3419.

41. Botan, A., et al., *Carbon Dioxide in Montmorillonite Clay Hydrates: Thermodynamics, Structure, and Transport from Molecular Simulation.* Journal of Physical Chemistry C, 2010. **114**(35): p. 14962-14969.

42. Schaef, H.T., et al., *In situ XRD study of Ca^{2+} saturated montmorillonite (STX-1) exposed to anhydrous and wet supercritical carbon dioxide.* International Journal of Greenhouse Gas Control, 2012. **6**: p. 220-229.

43. Ilton, E.S., et al., *In Situ X-ray Diffraction Study of Na+ Saturated Montmorillonite Exposed to Variably Wet Super Critical CO2.* Environmental Science & Technology, 2012. **46**(7): p. 4241-4248.

44. Or, D. and M. Tuller, *Liquid retention and interfacial area in variably saturated porous media: upscaling from single-pore to sample-scale model.* Water Resources Research, 1999. **35**(12): p. 3591-3605.

45. Bear, J. and J.J. Nitao, *On equilibrium and primary variables in transport in porous media.* Transport in Porous Media, 1995. **18**(2): p. 151-184.

46. Israelachvili, J., *Intermolecular and Surface Forces, Third Edition*. 2011, San Diego: Elsevier Inc. 674.

47. Dhanuka, V.V., et al., *High internal phase CO2-in-water emulsions stabilized with a branched nonionic hydrocarbon surfactant.* Journal of Colloid and Interface Science, 2006. **298**(1): p. 406-418.

48. Meli, L., et al., *Polystyrene thin films in CO_2*. Physical review. E, Statistical, nonlinear, and soft matter physics, 2004. **69**(5 Pt 1): p. 051601.

49. Gregory, J., *Interaction of unequal double layers at constant charge.* Journal of Colloid and Interface Science, 1975. **51**(1): p. 44-51.

50. Verwey, E.J.W. and J.T.G. Overbeek, *Theory of the stabiilty of lyophobic colloids*. 1948, Mineola, NY: Dover Publications. 218.

51. Yan, W., et al., *Interfacial tension of (methane plus nitrogen) plus water and (carbon dioxide plus nitrogen) plus water systems.* Journal of Chemical and Engineering Data, 2001. **46**(6): p. 1544-1548.

52. Tabor, R.F., et al., *Anomalous Stability of Carbon Dioxide in pH-Controlled Bubble Coalescence.* Angewandte Chemie-International Edition, 2011. **50**(15): p. 3454-3456.

53. Nelson, P.H., *Pore-throat sizes in sandstones, tight sandstones, and shales.* Aapg Bulletin, 2009. **93**(3): p. 329-340.

54. Moore, D.M. and R.C. Reynolds, *X-ray Diffraction and the Identification and Analysis of Clay Minerals*. 1997, Oxford, NY: Oxford University Press.

55. Spycher, N. and K. Pruess, *CO_2-H_2O mixtures in the geological sequestration of CO_2 II. Partitioning in chloride brines at 12-100 degrees C and up to 600 bar.* Geochimica et Cosmochimica Acta, 2005. **69**(13): p. 3309-3320.

56. Barraclough, P.B. and P.G. Hall, *Adsorption of water vapour by silica and effect of surface methylation.* Journal of the Chemical Society-Faraday Transactions I, 1978. **74**: p. 1360-1372.

57. Bérend, I., et al., *Mechanism of adsorption and desorption of water vapor by homoionic montmorillonite. 2. The Li^+, Na^+, K^+, Rb^+ and Cs^+ exchanged forms.* Clays and Clay Minerals, 1995. **43**(3): p. 324-336.

58. Cases, J.M., et al., *Mechanism of adsorption and desorption of water vapor by homoionic montmorillonite. 3. The Mg^{2+}, Ca^{2+}, Sr^{2+}, and Ba^{2+} exchanged forms.* Clays and Clay Minerals, 1997. **45**(1): p. 8-22.

59. Baleanu, M.C., et al., *New approach for consideration of adsorption/desorption data.* Communications in Nonlinear Science and Numerical Simulation, 2011. **16**(12): p. 4643-4648.

60. Lee, S. and R.W. Staehle, *Adsorption of water on gold.* Corrosion, 1996. **52**(11): p. 843-852.

61. Lee, S. and R.W. Staehle, *Adsorption of water on copper, nickel, and iron.* Corrosion, 1997. **53**(1): p. 33-42.

62. Chiarello, R.P., J. Krim, and C. Thompson, *Quartz-crystal microbalance and synchrotron X-ray reflectivity study of water and liquid Xenon adsorbed on gold and quartz.* Surface Science, 1994. **306**(3): p. 359-366.

63. Tagawa, M., et al., *Effect of water adsorption on microtribological properties of hydrogenated diamond-like carbon films.* Tribology Letters, 2004. **17**(3): p. 575-580.

64. Oliveira, N.S., et al., *Gas solubility of carbon dioxide in poly(lactic acid) at high pressures: thermal treatment effect.* Journal of Polymer Science Part B-Polymer Physics, 2007. **45**(5): p. 616-625.

65. Otake, K., et al., *Frequency change of a quartz-crystal microbalance at the supercritical condition of carbon dioxide.* Journal of Supercritical Fluids, 1994. **7**(4): p. 289-292.

66. Park, K.H., et al., *The behavior of quartz crystal microbalance in high pressure CO_2.* Journal of Supercritical Fluids, 2004. **29**(1-2): p. 203-212.

67. Griffins, P. and J. de Haseth, *Fourier Transform Infrared Spectrometry*. 2007, Hoboken, NJ: John Wiley and Sons. 536 p.

68. Prasad, P.S.R., D.S. Sarma, and S.N. Charan, *Mineral trapping and sequestration of carbon-dioxide in Deccan basalts: SEM, FTIR and Raman spectroscopic studies on secondary carbonates.* Journal of the Geological Society of India, 2012. **80**(4): p. 546-552.

69. Fernandez-Carrasco, L., J. Rius, and C. Miravitlles, *Supercritical carbonation of calcium aluminate cement.* Cement and Concrete Research, 2008. **38**(8-9): p. 1033-1037.

70. Bergren, M.S., et al., *The OH stretching region infrared spectra of low density amorphous solid water and polycrystalline ice Ih.* Journal of Chemical Physics, 1978. **69**(8): p. 3477-3482.

71. Schanz, T. and S. Tripathy, *Swelling pressure of a divalent-rich bentonite: Diffuse double-layer theory revisited.* Water Resources Research, 2009. **45**.

72. de Jong, S.M., C.J. Spiers, and A. Busch. *Strain development in smectite clays upon exposure to CO_2* in *European Geosciences Union General Assembly, 22-27 April*. 2012. Vienna, Austria.

73. Mang, J.T. and R.P. Hjelm, *Fractal networks of inter-granular voids in pressed TATB.* Propellants, Explosives, Pyrotechnics, 2013. **35**: p. 1-10.

74. IPCC, *IPCC special report on carbon dioxide capture and storage, prepared by Working Group III of the Intergovernmental Panel on Climate Change*, ed. B. Metz, et al. 2005, Cambridge, United Kingdom and New York, NY, USA: Cambridge University Press. 442.

75. Bennaceur, K., et al., *CCS: A Key Carbon Abatement Option*. 2008, Paris: OECD/IEA.

76. Pacala, S. and R. Socolow, *Stabilization wedges: Solving the climate problem for the next 50 years with current technologies.* Science, 2004. **305**(5686): p. 968-972.

77. Jahangiri, H.R. and D.X. Zhang, *Effect of spatial heterogeneity on plume distribution and dilution during CO_2 sequestration.* International Journal of Greenhouse Gas Control, 2011. **5**(2): p. 281-293.

78. Gherardi, F., T.F. Xu, and K. Pruess, *Numerical modeling of self-limiting and self-enhancing caprock alteration induced by CO_2 storage in a depleted gas reservoir.* Chemical Geology, 2007. **244**(1-2): p. 103-129.

79. Wang, S.B., I.M. Edwards, and A.F. Clarens, *Wettability Phenomena at the CO_2-Brine-Mineral Interface: Implications for Geologic Carbon Sequestration.* Environmental Science & Technology, 2013. **47**(1): p. 234-241.

80. Bowen, B.R., et al., *Depositional and diagenetic variability within the Cambrian Mount Simon Sandstone: Implications for carbon dioxide sequestration.* Environmental Geosciences, 2011. **18,**: p. 69-89.

81. Blum, A.E. and L.L. Stillings, *Feldspar dissolution kinetics*, in *Chemical Weathering Rates of Silicate Minerals*, A.F. White and S.L. Brantley, Editors. 1995. p. 291-351.

82. Alexeev, V.A., *Kinetics and mechanisms of the laboratory dissolution of feldspars.* Geochemistry International, 2001. **39**(11): p. 1078-1097.

83. Oelkers, E.H. and J. Schott, *Experimental study of anorthite dissolution and the relative mechanism of feldspar hydrolysis.* Geochimica et Cosmochimica Acta, 1995. **59**(24): p. 5039-5053.

84. Kawano, M. and K. Tomita, *Growth of smectite from leached layer during experimental alteration of albite.* Clays and Clay Minerals, 1994. **42**(1): p. 7-17.

85. Steefel, C.I. and P. Vancappellen, *A new kinetic approach to modeling water-rock interaction - the role of nucleation, precursors, and Ostwald ripening.* Geochimica et Cosmochimica Acta, 1990. **54**(10): p. 2657-2677.

86. Felmy, A.R., et al., *Reaction of water-saturated supercritical CO_2 with forsterite: Evidence for magnesite formation at low temperatures.* Geochimica et Cosmochimica Acta, 2012. **91**: p. 271-282.

87. Kwak, J.H., et al., *Metal Carbonation of Forsterite in Supercritical CO_2 and H_2O Using Solid State Si-29, C-13 NMR Spectroscopy.* Journal of Physical Chemistry C, 2010. **114**(9): p. 4126-4134.

88. Hu, Y.D., J.R. Ray, and Y.S. Jun, *Na^+, Ca^{2+}, and Mg^{2+} in brines affect supercritical CO_2-brine-biotite interactions: ion exchange, biotite dissolution, and illite precipitation.* Environmental Science & Technology, 2013. **47**(1): p. 191-197.

89. Sorai, M., T. Ohsumi, and M. Ishikawa, *Nanoscale surface observation of feldspar dissolved under supercritical CO_2-water-mineral system.* Energy, 2005. **30**(11-12): p. 2334-2343.

90. Regnault, O., et al., *Experimental study of pure mineral phases/supercritical CO_2 reactivity. Implications for geological CO_2 sequestration.* Comptes Rendus Geoscience, 2005. **337**(15): p. 1331-1339.

91. Hu, Y.D. and Y.S. Jun, *Biotite dissolution in brine at varied temperatures and CO_2 pressures: its activation energy and potential CO_2 intercalation.* Langmuir, 2012. **28**(41): p. 14633-14641.

92. Lackner, K.S., *A guide to CO_2 sequestration.* Science, 2003. **300**(5626): p. 1677-1678.

93. Ide, S.T., K. Jessen, and F.M. Orr, *Storage of CO_2 in saline aquifers: Effects of gravity, viscous, and capillary forces on amount and timing of trapping.* International Journal of Greenhouse Gas Control, 2007. **1**(4): p. 481-491.

94. Bachu, S., *CO_2 storage in geological media: Role, means, status and barriers to deployment.* Progress in Energy and Combustion Science, 2008. **34**(2): p. 254-273.

95. Taber, J.J., *Research on enhanced oil recovery - past, present, and future.* Pure and Applied Chemistry, 1980. **52**(5): p. 1323-1347.

96. de la Cruz, V. and T.J.T. Spanos, *Mobilization of oil ganglia.* Aiche Journal, 1983. **29**(5): p. 854-858.

97. Suekane, T., N. Zhou, and T. Hosokawa, *Maximation of capillary trapping ration to injected CO_2 by means of co-injection*, in *10th International Conference on Greenhouse Gas Control Technologies*, J. Gale, C. Hendriks, and W. Turkenberg, Editors. 2011. p. 4260-4266.

98. Qi, R., T.C. LaForce, and M.J. Blunt, *Design of carbon dioxide storage in aquifers.* International Journal of Greenhouse Gas Control, 2009. **3**(2): p. 195-205.

99. Bandara, U.C., A.M. Tartakovsky, and B.J. Palmer, *Pore-scale study of capillary trapping mechanism during CO_2 injection in geological formations.* International Journal of Greenhouse Gas Control, 2011. **5**(6): p. 1566-1577.

100. Garcia, J. and K. Pruess. *Flow instabilities during injection of CO_2 into saline aquifers.* in *Proceedings of the 2003 TOUGH Symposium*. 2003: Lawrence Berkeley National Laboratories.

101. Ng, K.M. and A.C. Payatakes, *Stochastic simulation of the motion, breakup, and stranding of oil ganglia in water-wet granular porous-media during immiscible displacement.* Aiche Journal, 1980. **26**(3): p. 419-429.

102. Payatakes, A.C., *Dynamics of oil ganglia during immiscible displacement in water-wet porous-media.* Annual Review of Fluid Mechanics, 1982. **14**: p. 365-393.

103. Constantinides, G.N. and A.C. Payatakes, *A theoretical model of collision and coalescence of ganglia in porous-media.* Journal of Colloid and Interface Science, 1991. **141**(2): p. 486-504.

104. Payatakes, A.C. and M.M. Dias, *Immiscible microdisplacement and ganglion dynamics in porous media.* Reviews in Chemical Engineering, 1984. **2,** : p. 486-504.

105. Pennell, K.D., G.A. Pope, and L.M. Abriola, *Influence of viscous and buoyancy forces on the mobilization of residual tetrachloroethylene during surfactant flushing.* Environmental Science & Technology, 1996. **30**(4): p. 1328-1335.

106. Gioia, F., et al., *Oil mobility in a saturated water-wetted bed of glass beads.* Journal of Hazardous Materials, 2003. **97**(1-3): p. 315-327.

107. Amili, P. and Y.C. Yortsos, *Darcian dynamics: a new approach to the mobilization of a trapped phase in porous media.* Transport in Porous Media, 2006. **64**(1): p. 25-49.

108. Larson, R.G., L.E. Scriven, and H.T. Davis, *Percolation theory of residual phases in porous-media.* Nature, 1977. **268**(5619): p. 409-413.

109. Larson, R.G., L.E. Scriven, and H.T. Davis, *Percolation theory of 2-phase flow in porous-media.* Chemical Engineering Science, 1981. **36**(1): p. 57-73.

110. Wilkinson, D., *Percolation model of immiscible displacement in the presence of bouyancy forces.* Physical Review A, 1984. **30**(1): p. 520-531.

111. Smith, J.E. and Z.F. Zhang, *Determining effective interfacial tension and predicting finger spacing for DNAPL penetration into water-saturated porous media.* Journal of Contaminant Hydrology, 2001. **48**(1-2): p. 167-183.

112. Chuoke, R.L., P. Vanmeurs, and C. Vanderpoel, *The instablity of slow, immiscible, viscous liquid-liquid displacement in permeable media.* Transactions of the American Institute of Mining and Metallurgical Engineers, 1959. **216**: p. 188-194.

113. Clift, R., J.R. Grace, and M.E. Weber, *Bubbles, Drops and Particles*. 1978, New York, NY: Academy Press.

114. Pentland, C.H., et al., *Immiscible Displacements and Capillary Trapping in CO_2 Storage*, in *10th International Conference on Greenhouse Gas Control Technologies*, J. Gale, C. Hendriks, and W. Turkenberg, Editors. 2011. p. 4969-4976.

115. Chiquet, P., D. Broseta, and S. Thibeau, *Wettability alteration of caprock minerals by carbon dioxide.* Geofluids, 2007. **7**(2): p. 112-122.

116. Degennes, P.G., *Wetting—statics and dynamics.* Reviews of Modern Physics, 1985. **57**(3): p. 827-863.

117. Bachu, S. and D.B. Bennion, *Interfacial Tension between CO_2, Freshwater, and Brine in the Range of Pressure from (2 to 27) MPa, Temperature from (20 to 125) degrees C, and Water Salinity from (0 to 334 000) mg L^{-1}*. Journal of Chemical and Engineering Data, 2009. **54**(3): p. 765-775.

118. Tewes, F. and F. Boury, *Formation and rheological properties of the supercritical CO_2 - water pure interface.* Journal of Physical Chemistry B, 2005. **109**(9): p. 3990-3997.

119. Bikkina, P.K., O. Shoham, and R. Uppaluri, *Equilibrated Interfacial Tension Data of the CO_2-Water System at High Pressures and Moderate Temperatures.* Journal of Chemical and Engineering Data, 2011. **56**(10): p. 3725-3733.

120. Benson, S.M. and D.R. Cole, *CO_2 sequestration in deep sedimentary formations.* Elements, 2008. **4**: p. 325-331.

121. Javadpour, F., *CO_2 injection in geological formations: determining macroscale coefficients from pore scale processes.* Transport in Porous Media, 2009. **79**(1): p. 87-105.

122. Saadatpoor, E., S.L. Bryant, and K. Sepehrnoori, *New Trapping Mechanism in Carbon Sequestration.* Transport in Porous Media, 2010. **82**(1): p. 3-17.

123. Krevor, S.C.M., et al., *Capillary heterogeneity trapping of CO_2 in a sandstone rock at reservoir conditions.* Geophysical Research Letters, 2011. **38**.

124. Yi, Y.B. and A.M. Sastry, *Analytical approximation of the percolation threshold for overlapping ellipsoids of revolution.* Proceedings of the Royal Society a-Mathematical Physical and Engineering Sciences, 2004. **460**(2048): p. 2353-2380.

125. Suekane, T., et al., *Direct Observation of Trapped Gas Bubbles by Capillarity in Sandy Porous Media.* Transport in Porous Media, 2010. **82**(1): p. 111-122.

126. Morrow, N.R., I. Chatzis, and J.J. Taber, *Entrapment and mobilization of residual oil in bead packs.* SPE Reservoir Engineering, 1988. **3**(3): p. 927-934.

127. Hilpert, M., C.Y. Guo, and J. Katz, *Capillary dynamics of elastic-wave-enhanced two-phase flow in porous media*, in *Innovations in Nonlinear Acoustics*, A.A. Atchley, V.W. Sparrow, and R.M. Keolian, Editors. 2006. p. 178-185.

128. Beresnev, I.A., *Theory of vibratory mobilization on nonwetting fluids entrapped in pore constrictions.* Geophysics, 2006. **71**(6): p. N47-N56.

DISTRIBUTION

4 Lawrence Livermore National Laboratory
Attn: N. Dunipace (1)
P.O. Box 808, MS L-795
Livermore, CA 94551-0808

1	MS0721	P. B. Davies	6200
1	MS0735	J. A. Merson	6910
1	MS0736	E. J. Bonano	6220
1	MS0779	S. J. Saltzstein	6225
1	MS0899	Technical Library	9536 (electronic copy)
1	MS0359	D. Chavez, LDRD Office	1911
1	MS0161	Legal Technology Transfer Center	11500

Sandia National Laboratories